A COMPUTATIONAL INVESTIGATION FOR TWO-DIMENSIONAL EDDY CURRENT TESTING PROBLEMS USING SUBREGION FINITE ELEMENT METHOD

By

Mohammad Rawhi Alrawashdeh

A DISSERTATION

Submitted to
Michigan State University
in partial fulfillment of the requirements
for the degree of

Electrical Engineering ─Doctor of Philosophy

2018

ABSTRACT

A COMPUTATIONAL INVESTIGATION FOR TWO-DIMENSIONAL EDDY CURRENT TESTING PROBLEMS USING SUBREGION FINITE ELEMENT METHOD

By

Mohammad Rawhi Alrawashdeh

A novel computational technique is presented in this thesis which improves Finite Element Method (FEM) in solving both direct and inverse problems for nondestructive evaluation (NDE) applications. Subregion method is used to select and isolate area of interest that design parameters need to be updated from entire domain. An elastic mesh generator is developed in this thesis to generate optimal meshes in the selected area to save connectivity matrix until having the most accurate design parameters. Using Subregion FEM (SFEM) in solving inverse problems will help in minimizing processing time and memory usage in addition of reducing solution complexity. An Eddy Current Testing (ECT) problem of detecting and characterizing the location and shape of surface and subsurface defects by separating the defects from entire domain is investigated to validate the presented SFEM algorithm. The elastic mesh generator is derived to update the pre-selected design parameters of the defect in each iteration. This novel meshing technique adds the specialty of using subregion method in inverse problems, where, elements and nodes numbering is saved inside and outside the defect region. Both of Genetic Algorithm (GA) and Simulated Annealing (SA) based optimization techniques are developed to get the accurate defect parameters. A parametric study of those defect parameters including size, depth and position is also presented to study the defect response problems by comparing with classical forward formulation. The presented SFEM results have been verified computationally using conventional FEM and COMSOL Multiphysics. Excellent results of signal agreement and processing time minimization with a reduction of 90% with an accuracy of 98% have been achieved. In addition, the presented SFEM algorithm has been verified experimentally using Aluminum (T6061-T6) and steel samples.

The experiments are carried out for the first time using an elongated excitation coil in a fixed position mounted on the top of the sample and Tunneling Magnetoresistive (TMR) sensor to measure magnetic field. The measured magnetic fields were used as input to the inverse SFEM solver and machined artificial defects were characterized with excellent accuracy.

To my friends and relatives who supported me through all my entire life

To the value of friendship;

"True friendship multiplies the good in life and divides its evils. Strive to have friends, for life without friends is like life on a desert island... to find one real friend in a lifetime is good fortune; to keep him is a blessing". Baltasar Gracian.

ACKNOWLEDGMENTS

Foremost, I would like to express my sincere gratitude to my advisor Prof. Yiming Deng for the continuous support of my Ph.D. study and research, for his patience, motivation, enthusiasm, and immense knowledge. His guidance helped me in all the time of research and writing of this thesis. I want to thank Prof. Deng for his financial and emotional support in addition to his academic supervision. It was a great privilege and honor to work and study under his guidance. I'm extremely grateful for what he has offered me.

I want to thank my retired adviser Prof. S. Ratnajeevan H. Hoole for giving me the opportunity to do this research. His dynamism, vision, sincerity and motivation have deeply inspired me in the field of computational electromagnetics. I am extending my heartfelt thanks to his wife and beautiful family for their acceptance, kindness and support.

I would like to thank the rest of my thesis committee: Prof. Lalita Udpa, Prof. Mahmoodul Haq and Prof. John Papapolymerou for their encouragement, insightful comments and unlimited support.

During my five academic years of graduate study, which involved research work with brilliant lab-mates and high-end class experience, I have been exposed to plenty of personality build up experience and was fortunate to work in a healthy research and academic environment that was offered by the Department of Electrical and Computer Engineering and different helping resources in Michigan State University; RCPD, OISS and Olin Centers and offices.

My sincere thanks also go to a lot of people in MSU who believed in my potentials. I believe that I would not succeed and get my PhD without their support and encouragement. Those people are:

Prof. John Papapolymerou, Professor Manoochehr Koochesfahani, Professor Hassan Khalil, Professor Hayder Radha, Professor Katy Colbry, Professor Dean Aslam, Professor Antonio Nunez, Professor Leo Kempel and Professor Satish Udpa. Each one of those professors contributed in different way in my academic progress.

There are different MSU centers and offices supported me during these five years. I want to thank my beloved and great doctors who took care of my health, special thanks go to Dr. Richard Kustasz and Dr. Debra Duxbury. I want also to thank my clinical social worker Karen Boyd for all what she did for me. I want to thank the RCPD office for giving me the required accommodations during my study. I want also to thank the graduate students for choosing me as their representative in the GSC in our department. I tried to help them as much as I can through my department and through the GEU.

I want to thank my friends and relatives who helped and supported me during all the drama that I have lived in my life; starting from the sickness and the death of my father after returning back from the Gulf War before 28 years and ending by the falling accident and the related health issues that affected my life at the beginning of my PhD study in USA.

Special mention goes to my great and beloved enthusiastic supervisor in Jordan, Prof. Nihad Dib. My academic life has been an amazing experience, not only for his tremendous academic support, but also for giving me so many wonderful opportunities.

My great mother who sacrificed a lot for me deserves a special thank from me. No words are sufficient to describe my mother's contribution to my life. I owe every bit of my existence to her. I am looking to see my beloved mother Heyam in this coming summer insha'allah after five years of waiting. My mother raised me by her love and passion. I am looking to that moment when I

bend and kiss her immaculate hands. I am looking to that moment when she will meet my children after long time of waiting.

Last but not the least; I would like to thank my beautiful wife, Doaa for supporting and helping me in these five years. I was lucky to have three beautiful and amazing children; Maria, Elias and Rawhi. My beloved wife took care of all of us. I was not the only person who flighted and worked hard in these five years, my wife was the co-fighter and the source of inspiration. She took care of all of us. Thank you Doaa.

Finally, I would like to thank my home country; Jordan and my university, Yarmouk University for covering my PhD study in the previous years. I am looking to return to my country and to serve my community.

Mohammad R. Rawashdeh

TABLE OF CONTENTS

LIST OF TABLES

LIST OF FIGURES

1 Introduction

In the year of 1831, the English scientist Michael Faraday discovered electromagnetic induction. Faraday found an electric current would flow through the conductor when a conductor passes through a magnetic field. This current would flow if there is a closed path through which the current can circulate. On that time, the terminology of eddy current was not a fundamental part in research like these days. Eddy current was called sometime as Foucault currents referring to the French scientist Leon Foucault who generated magnetic fields in 1951. Foucault experiment was in placing a moving copper desk in a strong magnetic field. This generated magnetic field is generated due to the eddy current existence.

The basic explanation for ECT of crack detection that will be presented in this thesis is that a magnetic field will be resulted from AC current excitation. This magnetic field will induce an eddy current starting on the surface and deeply inside the conductor. An opposing magnetic field due to the flow of eddy currents will be produced, while we can detect the resultant magnetic field density values at some fixed measuring points. This coil has the flexibility of moving to scan all surface of the conductor to detect defect(s). Once the defect starts to interrupt the paths of the eddy current, that will lead to a direct effect on the opposing magnetic field in the entire material in general and on a pre-determined measuring points in specific. These measuring points will be used to define some parameters later to examine the effect of the defect on the magnetic flux density on these points. That defect could be detected using the concept of ECT as shown in Figure 1-1.

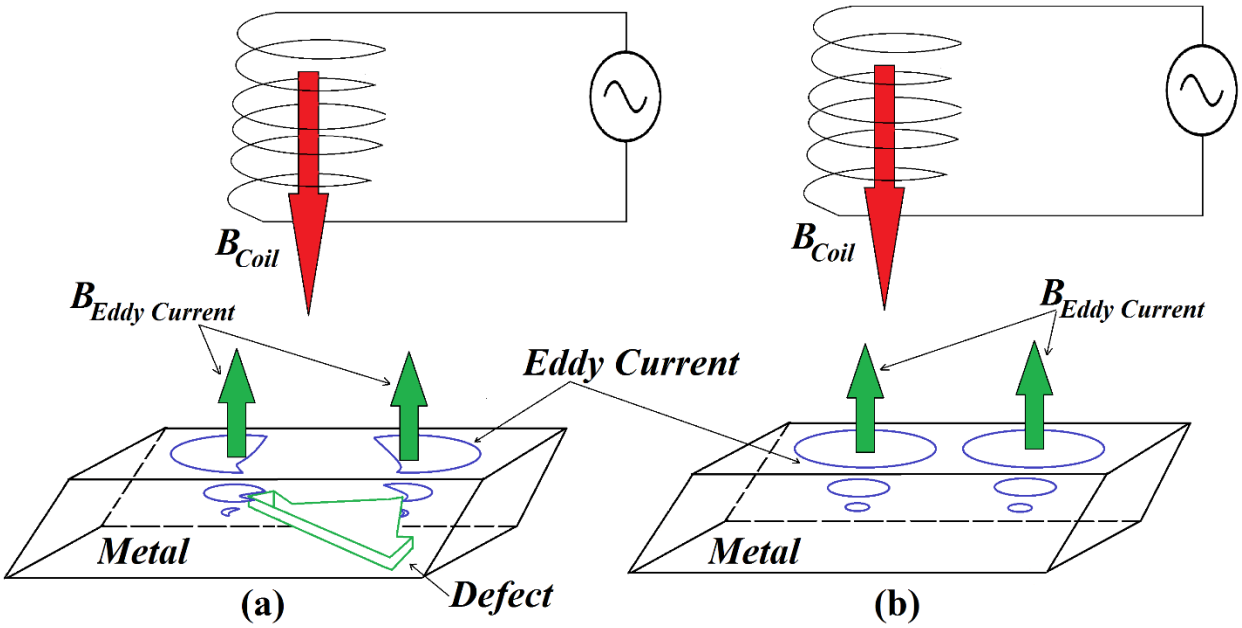

Figure 1-1 Side view of the effect of the defect on the eddy current regular paths (a) Interrupted eddy current paths due to the defect (b) Defect free conductor with regular eddy current paths.

A computational model, by improving FEM using subregion method is presented in this thesis to study both direct and inverse ECT problems. Using SFEM in solving such problems will reduce processing time and memory usage in tangible values compared to conventional FEM.

The introduction of this thesis will give a general view for different techniques used in nondestructive evaluation (NDE) technology. Then, we will focus on ECT since we used the presented SFEM algorithm to solve ECT problems to validate the proposed SFEM methodology. The mathematical derivation for SFEM and elastic meshing and how they are used in solving ECT problems will be presented in Chapters: 2, 3, 4 and 5 in this thesis. While, the experimental part of setting up an ECT experiment will be explained in detail in Chapter 6. The final chapter will give a complete discussion of the results found in this thesis in addition to the recommended future work.

1.1 Nondestructive Evaluation

Nondestructive testing (NDT) is a wide group of analysis techniques used in science and technology industry to evaluate the properties of a material, component or system without causing damage. The terms nondestructive inspection (NDI) and nondestructive evaluation (NDE) are also commonly used to describe this technology. Because NDT does not permanently alter the article being inspected, it is a highly valuable technique that can save both money and time in product evaluation, troubleshooting, and research. The six most frequently used NDT methods in industry are eddy-current [1-5] , magnetic-particle [6-8], liquid penetrant [9-11], radiographic [6, 12-16], ultrasonic [17-22], and visual testing [6, 20, 23, 24]. NDT is commonly used in forensic engineering [25-28], mechanical engineering [29-31], petroleum engineering [32-34], electrical engineering [24, 35-38] and civil engineering [30, 39-42], .

NDT methods may rely upon use of electromagnetic radiation, sound, and inherent properties of materials to examine samples. This includes some kinds of microscopy to examine external surfaces in detail, although sample preparation techniques for metallography, optical microscopy and electron microscopy are generally destructive as the surfaces must be made smooth through polishing or the sample must be electron transparent in thickness. The inside of a sample can be examined with penetrating radiation, such as X-rays, neutrons or terahertz radiation. Sound waves are utilized in the case of ultrasonic testing. Contrast between a defect and the bulk of the sample may be enhanced for visual examination by the unaided eye by using liquids to penetrate fatigue cracks. One method (liquid penetrant testing) involves using dyes, fluorescent or non-fluorescent, in fluids for non-magnetic materials, usually metals. Another commonly used NDT method used on ferrous materials involves the application of fine iron particles (either liquid or dry dust) that are applied to a part while it is in an externally magnetized state (magnetic-particle testing). The

particles will be attracted to leakage fields within the test object, and form on the objects surface. Magnetic particle testing can reveal surface and some sub-surface defects within the part. Moreover, thermoelectric effect uses thermal properties of an alloy to quickly and easily characterize many alloys. The chemical test, or chemical spot test method, utilizes application of sensitive chemicals that can indicate the presence of individual alloying elements. Electrochemical methods, such as electrochemical fatigue crack sensors, utilize the tendency of metal structural material to oxidize readily to detect progressive damage [43-47].

1.2 Eddy Current Testing

Eddy-current testing (ECT) is one of many electromagnetic testing methods used in nondestructive testing (NDT) making use of electromagnetic induction to detect and characterize surface and sub-surface flaws in conductive materials.

Eddy current testing as a technique for testing finds its roots in electromagnetism. Eddy currents were first observed by François Arago in 1824, but French physicist Léon Foucault is credited with discovering them in 1855. ECT began largely as a result of the English scientist Michael Faraday's discovery of electromagnetic induction in 1831. Faraday discovered that when there is a closed path through which current can circulate and a time-varying magnetic field passes through a conductor (or vice versa), an electric current flows through this conductor.

In 1879, another English-born scientist, David Edward Hughes, demonstrated how the properties of a coil change when placed in contact with metals of different conductivity and permeability, which was applied to metallurgical sorting tests.

Much of the development of ECT as an nondestructive testing technique for industrial applications was carried out during World War II in Germany. Professor Friedrich Förster while working for

the Kaiser-Wilhelm Institute (now the Kaiser Wilhelm Society) adapted eddy current technology to industrial use, developing instruments measuring conductivity and sorting mixed ferrous components. After the war, in 1948, Förster founded a company, now called the Foerster Group where he made great strides in developing practical ECT instruments and marketing them.

Eddy current testing is now a widely used and well understood inspection technique for flaw detection, as well as thickness and conductivity measurements. Frost & Sullivan analysis in the global NDT equipment market in 2012 estimated the magnetic and electromagnetic NDT equipment market at $220 million, which includes conventional eddy current, magnetic particle inspection, eddy current array, and remote-field testing. This market is projected to grow at 7.5% compounded annual growth rate to approximately $315 million by 2016.

In its most basic form, the single-element ECT probe where a coil of conductive wire is excited with an alternating electrical current. This wire coil produces an alternating magnetic field around itself. The magnetic field oscillates at the same frequency as the current running through the coil. When the coil approaches a conductive material, eddy currents are induced in the material.

Variations in the electrical conductivity and magnetic permeability of the test object, and the presence of defects causes a change in eddy current and a corresponding change in phase and amplitude that can be detected by measuring the impedance changes in the coil, which is a telltale sign of the presence of defects. This is the basis of standard (pancake coil) ECT.

ECT has a very wide range of applications. Because ECT is electrical in nature, it is limited to conductive material. There are also physical limits to generating eddy currents and depth of penetration (skin depth).

The two major applications of ECT are surface inspection [48-51] and tubing inspections [49, 52-55]. Surface inspection is used extensively in the aerospace industry, but also in the petrochemical industry. The technique is very sensitive and can detect tight cracks. Surface inspection can be performed both on ferromagnetic and non-ferromagnetic materials.

Tubing inspection is generally limited to non-ferromagnetic tubing and is known as conventional ECT. Conventional ECT is used for inspecting steam generator tubing in nuclear plants and heat exchangers tubing in power and petrochemical industries. The technique is very sensitive to detect and size pits. Wall loss or corrosion can be detected but sizing is not accurate.

A variation of conventional ECT for partially magnetic materials is full saturation ECT. In this technique, permeability variations are suppressed by applying a magnetic field. The saturation probes contain conventional eddy current coils and magnets. This inspection is used on partially ferromagnetic materials such as nickel alloys, duplex alloys, and thin-ferromagnetic materials such as ferritic chromium molybdenum stainless steel. The application of a saturation eddy current technique depends on the permeability of the material, tube thickness, and diameter. A method used for carbon steel tubing is remote field ECT. This method is sensitive to general wall loss and not sensitive to small pits and cracks [56-59].

When it comes to surface applications, the performance of any given inspection technique depends greatly on the specific conditions - mostly the types of materials and defects, but also surface conditions, etc. [60]. However, in most situations, the following statements for conventional ECT are true:

- Effective on coatings/paint: yes

- Computerized record keeping: partial
- 3D/Advanced imaging: none
- User dependence: high
- Speed: low
- Post-inspection analysis: none
- Requires chemicals/consumables: no

ECT is also useful in making electrical conductivity and coating thickness measurements, among others [61].

To circumvent some of the shortcomings of conventional ECT, other ECT techniques were developed with various successes. Conventional ECT uses sinusoidal alternating current of a particular frequency to excite the probe. Pulsed eddy current (PEC) testing uses a step function voltage to excite the probe. The advantage of using a step function voltage is that such a voltage contains a range of frequencies. As a result, the electromagnetic response to several different frequencies can be measured with just a single step [62, 63]. Since depth of penetration depends on the excitation frequency, information from a range of depths can be obtained all at once. If measurements are made in the time domain, i.e., by looking at the strength of the signal as a function of time, indications produced by defects and other features near the inspection coil can be seen first and more distant features will be seen later in time.

When comparing PEC testing with the conventional ECT, ECT can be regarded as a continuous-wave method where propagation takes place at a single frequency or, more precisely, over a very narrow-frequency bandwidth. With pulse methods, the frequencies are excited over a wide band, the extent of which varies inversely with the pulse length; this allows multi-frequency operation.

The total amount of energy dissipated within a given period of time is considerably less for pulsed waves than for continuous waves of the same intensity, thus allowing higher input voltages to be applied to the exciting coil for PEC than conventional ECT.

One of the advantage of this type of testing is that there is no need for direct contact with the tested object. Testing can be performed through coatings, sheathings, corrosion products and insulation materials. Through this way, even high-temperature inspections are possible.

Eddy current array (ECA) and conventional ECT share the same basic working principles. ECA technology provides the ability to electronically drive an array of coils (i.e., multiple coils) arranged in a specific pattern called a topology that generates a sensitivity profile suited to the target defects. Data acquisition is achieved by multiplexing the coils in a special pattern to avoid mutual inductance between the individual coils [64, 65]. The benefits of ECA are:

- Faster inspections
- Wider coverage
- Less operator dependence - array probes yield more consistent results compared to manual raster scans
- Better detection capabilities
- Easier analysis because of simpler scan patterns
- Improved positioning and sizing because of encoded data
- Array probes can easily be designed to be flexible or shaped to specifications, making hard-to-reach areas easier to inspect

ECA technology provides a remarkably powerful tool and saves significant time during inspections. For example, ECA inspection in carbon steel welds is regulated by ASTM standard E3052.

In EC NDE, a different, albeit physically closely related challenge is the detection of deeply lying flaws and inhomogeneities in electrically conducting solid materials. In the traditional version of ECT, an alternating (AC) magnetic field is used to induce eddy currents inside the material to be investigated. If the material contains a crack or a flaw, which make the spatial distribution of the electrical conductivity non-uniform, the path of the eddy currents is perturbed and the impedance of the coil, which generates the AC magnetic field is modified. By measuring the impedance of this coil, a crack can hence be detected. Since the eddy currents are generated by an AC magnetic field, their penetration into the subsurface region of the material is limited by the skin effect. The applicability of the traditional version of ECT is therefore limited to the analysis of the immediate vicinity of the surface of a material, usually of the order of millimeters. Attempts to overcome this fundamental limitation using low frequency coils and superconducting magnetic field sensors have not led to widespread applications [66, 67].

A recent technique, referred to as Lorentz force ECT (LET), exploits the advantages of applying DC magnetic fields and relative motion providing deep and relatively fast testing of electrically conducting materials. In principle, LET represents a modification of the traditional ECT from which it differs in two aspects, namely (i) how eddy currents are induced and (ii) how their perturbation is detected. In LET, eddy currents are generated by providing the relative motion between the conductor under test and a permanent magnet. If the magnet is passing by a defect,

the Lorentz force acting on it shows a distortion whose detection is the key for the LET working principle. If the object is free of defects, the resulting Lorentz force remains constant.

One of the major advantages of eddy current as an NDT tool is the variety of inspections and measurements that can be performed. In proper circumstances, eddy currents can be used for crack detection, material thickness measurement, coating thickness measurement and conductivity measurement. Some of the advantages of eddy current inspection include that it is sensitive to small cracks and it detects surface and near surface defects by giving immediate results. There are few limitations of eddy current inspection include [68-70]: only conductive materials can be inspected, surface must be accessible to the probe, skill and training required is more extensive than other techniques, surface finishing and roughness may interfere, reference standards needed for setup and flaws such as delamination's that lie parallel to the probe coil winding and probe scan direction are undetectable

1.3 Motivation

Finite Element Method (FEM) has been widely used for solving different electromagnetic problems [71-76]. ECT is an example of electromagnetic quasi-static problems, which can be solved by different methods using FEM [77, 78]. Computational methods, which lead later to different commercial FEM software, can use different kinds of mathematical and numerical techniques that play a key role in improving FEM. The idea of subregion method was applied successfully in conjunction with many computational techniques, especially in Finite Element Method for solving electromagnetic problems to reduce processing time and saving issues [79-83]. Frontal method, as an example of subregion method was used for repeated solution of large sparse matrices in electromagnetic problems [84]. SFEM was used before in designing machine pole at

given values for magnetic flux density as some measuring points [85]. Dividing solution domain of a problem to multiple regions regarding the physical properties or areas of interest and recombine them later using subregion method can be used in ECT techniques, where we can detect and reconstruct the shape of different types of defects. This will be useful in testing the performance of the entire system that contains these metals. These metals maybe parts of aircrafts, vehicles or industrial machines and the defects may be close to surface, on surface or deep inside the metal. In this thesis, we developed a general algorithm for all defect shapes and positions. The numerical results have been verified using COMSOL and conventional FEM. The presented algorithms can be used in industry and to improve commercial software especially in simulating complicated shape problems that needs long processing time.

Engineering design problems can be defined in two opposing ways according to given and required data. Direct or forward problems, which can be, defined as the problems of calculating what should be observed for a particular model.. Where inverse problem can be defined as the process of calculating from a set of observations the causal factors that produced them: for example, calculating an image in computer tomography, source reconstructing in acoustics, or calculating the density of the Earth from measurements of its gravity field [86-89]. It is called an inverse problem because it starts with the results and then calculates the causes. Inverse problems are some of the most important mathematical problems in science and mathematics because they tell us about parameters that we cannot directly observe. They have wide applications in optics, radar, acoustics, communication theory, signal processing, medical imaging, computer vision, geophysics, oceanography, astronomy, remote sensing, natural language processing, machine learning, nondestructive testing, and many other fields [90-94]. Figure 1-1 shows how design process rarely calls upon the engineer to solve the direct problem only.

Figure 1-2 Block diagram for direct problems

When an electromagnetic system is given, using such well- known methods as finite elements or boundary elements [95, 96], for example, it may be analyzed for its electromagnetic fields; these are then used to predict the system's performance defined by such as quantities forces, voltages, flux linkages and so on.

The inverse problem in this thesis of detecting and characterizing hidden defects inside metals can be described in Figure 1-2, where we can get our optimal solution by finding the best matching defect from known parameters of the current density, permeability and conductivity of the entire problem.

Figure 1-3 Block diagram for inverse problems

ECT, as seen in Figure 1-4; came from the idea of applying an AC source, which generates an AC current in the connected coil that is close to the conductor surface.

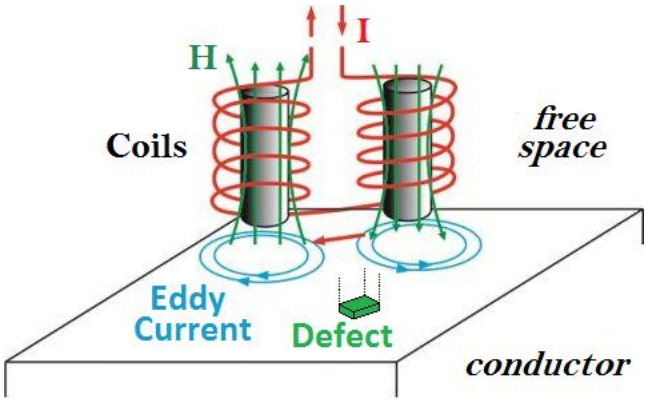

Figure 1-4 Eddy current formulation in conductive materials

As an example of practical application in industry, ECT is used in aircrafts for detecting defects in different multilayer aircraft structures and study some selective depth techniques [97, 98] . In nuclear plant structures, [99] showed how to design Rotating Magnetic Field Eddy-Current Probe (RoFEC) eddy-current probe composed of three windings excited by three-phase as current sources. FEM is one of the leading computational tools that used in ECT. In general, and from computational point of view, FEM was used in ECT techniques for the purpose of detecting defects [97-106]. Recently, domain decomposition FEM was used to divide the solution into both test sample and core domains [107]. The problems of processing speed and saving storage were types of major challenges for researchers who use FEM in their practical applications simulations. Graphical Processing Units- Finite Element Method (GPU-FEM) was used to solve such problems for different defects shapes [108-113]. In this thesis, subregion method, which is widely used in structural engineering is improved for solving Forward ECT problems by studying multiple defects with different angles, shapes and positions. Then, this algorithm is improved and developed to study some defects characterization problems, where we use inverse problem mathematical techniques and both of Genetic Algorithm and Simulated Annealing optimization methods to get the best shape of the defect that is close to the "ground truth". We developed and improved an elastic meshing method to track these hidden defects, so we can only conduct FEM computation

within defect region efficiently. Finally, all solutions can be merged using the sub-regional FEM. This process will stop when we get the optimal defect shape.

Defect Characterization techniques vary according to multiple factors. A C-Scan imaging method was presented in [106] using LabView for DAQ, and defect evaluation is carried out. Experimental work is widely used in defects and cracks detection and characterization. Infrared Thermography was used in [105] to inspect large areas non-invasively rapidly and provide full field images in a noncontact nature.

1.4 Problem Statement

In this thesis, we have derived new algorithm contains an integration between subregion Method, which was introduced in [85] for solving some magnetostatic problems with an Elastic Mesh Generation scheme that was introduced in [114] for solving pole machine problems, where we used Genetic Algorithm and Simulated Annealing optimization techniques for minimizing the cost function and get the optimal shape of the defect shape [115, 116].

In our two dimensional (2-D) Mmagnetostatic and ECT problems, we started from the adaptive mesh generator which was introduced in [116, 117]. We derived our FEM solver starting from [95, 118], which presented how classical FEM algorithms can be derived for solving different EM problems. Detecting defects in metals using classical FEM will not be a problem from processing time side since FEM analysis will be applied only one time for the entire domain. It is necessary to know the exact shape of defects shapes. To do that, an iterative method can be applied and different defect shapes will be found at each iteration until having the optimal solution/approximation. Be noted that the entire domain has a fixed surface area and this area contains the reconstructed defect each iteration. To do that, we will need a flexible and iterative FEM mesh generator. There are several methods for developing some algorithms for generating

meshes as in [119-121]. In [117], a parameter based mesh generator was used to generate meshes for the purpose of characterizing two dimensional defects as shown in [108, 109, 115, 116] where the idea for this mesh generator is to change the number of nodes and elements and then to change the related connectivity matrix at each iteration. The core in SFEM is to divide the entire domain to two different regions; first, defect region and second, the reminder domain. These two regions will be connected to each other using interfacing nodes. Those nodes should have fixed positions and they should not change their positions. Therefore, we will not be able to use the methods developed in [117] to solve inverse SFEM problems. As a result, we used an elastic mesh generator that saves interfacing nodes positions to generate meshes and nodes to solve inverse SFEM problems. Examples for these adaptive elastic meshing techniques are presented in [122, 123]. For the presented SFEM to be used in inverse ECT problems, the mesh generator that was presented in [114] was used to derive an elastic mesh generator to update meshing in the defect region each iteration. This update should continue until getting the optimal defect shape where we used both Simulated Annealing and Genetic Algorithm for this issue. Genetic Algorithm [124-129] and Simulated Annealing [129-133] are used to solve different inverse problems in computational science and engineering. We get an excellent defect characterization and detection matching between our SFEM results and [108-116] . The presented results in this thesis have been verified through COMSOL in addition to an experimental validation that was done in the Nodestructive Evaluation Lab at Michigan State University. Those results prove that our presented algorithm is valid and can be extended to more advanced applications as will be shown in this study.

1.5 Thesis Contributions

This study passes through multiple steps as introduced in previous sections. The main contribution in this thesis is considered computational by developing new algorithms for solving computational

electromagnetic problems. To verify the presented algorithm, we used it in solving multiple direct and inverse 2D-ECT problems. Later, we set up a complete experiment to verify the numerical results experimentally and we get an excellent computational and experimental validation. We can summarize the contributions in this doctoral thesis as:

1) Improving conventional Finite Element Method (FEM) by using Subregion method by improving FEM so, regions will be assembled instead of elements. This will improve processing time and memory usage for solving inverse problems.
2) Developing a Subregion 2D-FEM solution for Magnetostatic problems. We want to find the magnetic field and vector potential lines that resulted from passing known current through cable. We used classical FEM to validate our algorithm for the same problem parameters. This work was done before in [31] and we started developing our algorithm by using it in solving different Magnetostatic problems to verify our algorithm before improving it for solving Eddy Current problems.
3) We updated the SFEM solver to solve direct Eddy Current problems. This study is done for the first time for these kinds of problems. We designed our algorithm so it can solve any 2D SFEM-ECT problems. We studied multiple defect shapes with different angles and positions. After that, we compared between our results and other published results in addition to COMSOL and experimental validation. We get excellent matching between these results.
4) We improved our methodology that we used in solving direct SFEM-ECT problems so we can solve inverse ECT-FEM problems. Solving these inverse problems led to find and detect hidden defects inside metals. We used both Genetic Algorithm and Simulated

Annealing as optimization techniques to minimize cost function. This study has been done for the first time and will help to minimize processing time and in memory saving.

5) In addition to computational and COMSOL validation, a complete setup for an experimental part was done for testing both of a steel plate (0.15 - 0.30% carbon and Fe) and Aluminum (T6061-T6) samples with defects. Moreover, we get an excellent matching between SFEM and experimental results. We used TMR sensor to measure the component of the magnetic field normal to the sample top surface.
6) Deriving an elastic mesh generator that can be used for subregion problems. This technique has the property of giving a unique solution for gridding the divided regions into elements and changing elements distributions within these regions with keeping the same connectivity between these elements. This idea for this technique was introduced in [56] in solving some Magnetostatic problems. This technique is improved in this study and merged with SFEM be one algorithm that can solve any inverse SFEM problem.
7) The major part of minimizing computational processing time up to 90% compared to classical FEM with a reconstruction defect shape accuracy of 98% was achieved which can lead to use this technique in online and in field practical testing problems.
8) A complete description for future work to extend the presented algorithm to serve more complicated projects will be presented in Chapter Seven in this dissertation.

2 Finite Element Method

Computational Electromagnetics plays an important role in modeling and solving different NDE problems. Those methods helps to understand the underlying physics, more cost effective testbed for NDE sensors development and developing different numerical algorithms can be used to improve commercial software used in NDE in addition comparing with experimental results [134-138].

2.1 Finite Element Computation for Two-Dimensional Magneto-Static Problems

The presented algorithm in solving ECT problems using SFEM is derived from solving and analyzing Magneto-Static problems by using SFEM find the optimal shape of a magnetic pole piece for obtaining a constant air gap flux density and finding the magnetic flux density that resulted from passing current through coil [85]. Therefore, the first step is to validate the proposed algorithm to these magnetostatic problems. After that, moving to the next step which is the core of this research by solving Eddy Current problems to detect hidden defects and then to characterize these defects in order to evaluate the overall performance. Finally, these algorithms can be used to solve a complete inverse problem, which is another objective of this thesis.

Using SFEM solve a complete magnetostatic problem means to solve the related differential equation using FEM after dividing the domain to specific subregions. A complete solution for the magnetic vector potential will be demonstrated for a sheathed cable through this method. After that, these potential lines will be drawn inside the cable as shown in Figure 2-1 [95].

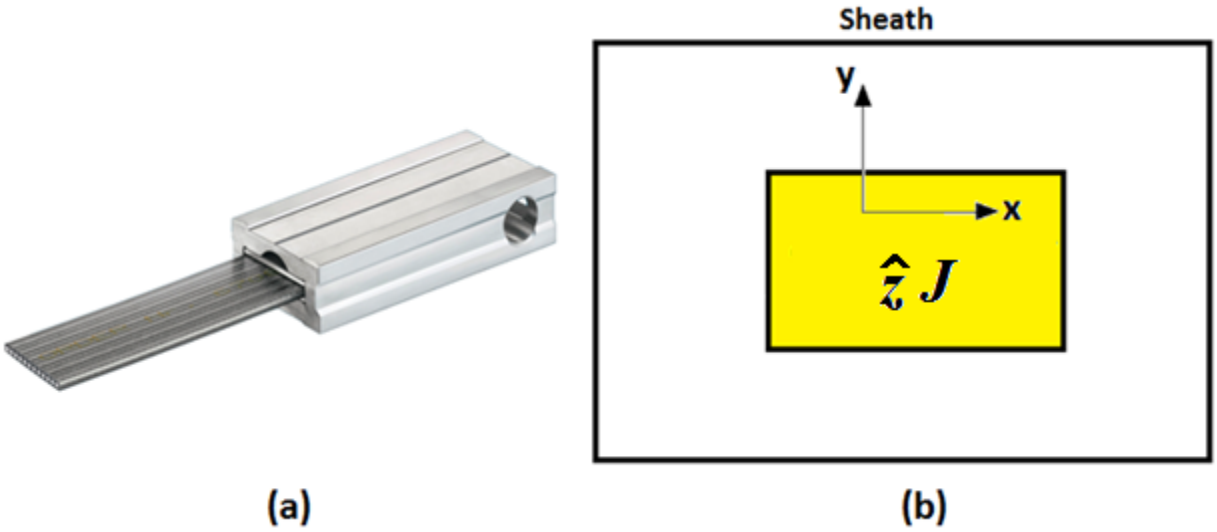

Figure 2-1 Cable System:(a) Commercial Board to wire connecter, rectangular for flat cables (b) a 2D cross sectional for sheathed infinitely long cable carrying current through inner conductor and returned through the outside sheath.

We need to start from Maxwell's equations to derive the governing second order differential equation for the system shown in Figure 2-1 to get the values of magnetic potentials. These equations are:

$$\nabla \bullet \overline{D} = \rho \tag{2.1}$$

$$\nabla \bullet \overline{B} = 0 \tag{2.2}$$

$$\nabla \times \overline{H} = \overline{J} + \frac{\partial \overline{D}}{\partial t} \tag{2.3}$$

$$\nabla \times \overline{E} = 0 \tag{2.4}$$

where $\overline{D}$ is electric flux density, $\frac{\partial \overline{D}}{\partial t}$ is displacement current which is negligible at low frequencies since it has low value compared to conductive current $\overline{J}$ [95, 118], ρ is the electric charge density, $\overline{B}$ is the magnetic flux density, $\overline{H}$ is the magnetic field intensity, $\overline{J}$ is the conductive current density**,** and $\overline{E}$ is the electric field intensity. Where we can relate $\overline{J}$ is to $\overline{E}$ by the constitutive relationship:

$$\overline{J} = \sigma_e \overline{E} \tag{2.5}$$

where σ_e is the material electric conductivity. $\overline{B}$ is related to $\overline{H}$ as $\overline{D}$ is related to $\overline{E}$ by the constitutive relationships:

$$\overline{B} = \mu \overline{H} \tag{2.6a}$$

$$\overline{D} = \varepsilon \overline{E} \tag{2.6b}$$

where ε is the permittivity and μ is the permeability. In addition to these equations, the magnetic vector potential $\overline{A}$ is defined by**:**

$$\overline{B} = \nabla \times \overline{A} \tag{2.7}$$

Now, for the vector $\overline{A}$ to be unique and therefore determinable, its divergence must be defined. This can be done by Coulomb Gauge as:

$$\nabla \bullet \overline{A} = 0 \tag{2.8}$$

The subject of computational electromagnetics may be divided into low and high frequency electromagnetics. It is a natural separation in view of the governing equations and the specialized nature of the division between low and high frequency electromagnetics. Typical low frequency devices are electrical machines, electronic devices, transmission lines, and magnetic recording heads whereas high frequency devices are waveguides, resonant cavities, and radiating devices such as antennae. In terms of equations, the difference between these two systems is that in low frequency devices, displacement current is negligible while in high frequency devices it is not. Therefore, for high frequency devices, although $\overline{D}$ is small, its rate of change is high, making $\frac{\partial \overline{D}}{\partial t}$ of equation (2.3) will be reduced to conductive current only. However, in many problems in lossless media, where medium has zero conductivity σ_e, no conduction current may exist in keeping with equation (2.5).

Since $\overline{H} = \upsilon \overline{B}$ and $\overline{B} = \nabla \times \overline{A}$ where υ is the reluctivity:

$$\overline{H} = \upsilon \overline{B} = \upsilon \nabla \times \overline{A} \tag{2.9}$$

Substituting the magnetic field intensity $\overline{H}$ from equation (2.9) into (2.3), so the result curl of curl of the magnetic vector potential will be will be: $\nabla \times \left(\upsilon \nabla \times \overline{A} \right) = \overline{J}$.

Since υ is constant, so: $\nabla \times \nabla \times \overline{A} = \nabla \left(\nabla \bullet \overline{A} \right) - \nabla^2 \overline{A}$ and $\nabla \bullet \overline{A} = 0$ leading to:

$$-\upsilon \nabla^2 \overline{A} = \overline{J} \tag{2.10}$$

Although we have continued variable governed by one equation, we still must solve for three components. A great simplification arises in two dimensional problems where no changes occur in one direction as in *z*- direction, so: $\frac{\partial}{\partial z} \equiv 0$. In this case, all magnetic flux will be on the *xy*-plane. From curl equation (2.3) and setting B_z =0, then: $\overline{J} = \hat{z} J$. Since equation (2.10) represents three Poisson's equations for the three components of $\overline{A}$, the vector $\overline{A}$ will have only one component as: $\overline{A} = \hat{z} A$ where this value of vector potential will automatically have zero divergence in view of imposing $\frac{\partial}{\partial z} \equiv 0$. The resulting equation after putting vector potential in equation (2.8) and thereafter equating the magnitudes we can derive the Poisson equation for the magnitude *A* of the vector potential $\overline{A}$ as:

$$-\upsilon \nabla^2 A = J \tag{2.11}$$

It is seen that in two dimensional Magnetostatic at least under which many design tasks are fitted, using the vector potential does replace a vector unknown by a scaler giving us scalar boundary value problem.

Given the current through the cable, the solution for the previous Poisson's Equation in (2.11) will be the magnetic vector potentials within the cable of Figure 2-1. The idea of FEM is to divide the space of solution into mesh of triangles. Points in these triangles are called the interpolation nodes of the mesh. The variation of the potential over the triangles is assumed to be defined by a given trial function. The objective is to find the potentials at the nodes of the mesh so that the potential at any given point inside a triangle can be found using the trial function. To do this, we develop one equation per unknown node in the mesh. Then, this set of equations must be solved to find the potentials at each node. Since these equations alone are not enough to get a unique solution, some boundary conditions must also be considered. These boundary conditions are imposed to help us to get the values for all unknown nodes for our problem.

The main objective of using FEM is to find solution for such Partial Differential equations as in equation (2.11) that do not have close form solution in the problem domain.

To start the FEM equations, we will identify the energy functional that is at its minimum at the point of solution and has the energy is at its minimum at stable state. This function is called the Lagrange Function.

The Lagrange Function for the scalar boundary problem in equation (2.11) is given by:

$$L[A] = \iint_R \left(\frac{\upsilon}{2} (\nabla A)^2 - JA \right) dR \tag{2.12}$$

Where the solution domain R will be meshed to triangular elements and a first order two-dimensional trail function can be represented for any point inside these elements, as we will see in the following section.

2.2 Interpolation Using First Order Trial Functions

In our two-dimensional problem in Figure 2.1 we will use a two-dimensional triangular element in order of discretizing our domain. A first order trail function $\phi_{\triangle}(x,y)$ can be represented in Cartesian coordinate for any point inside any arbitrary element as:

$$\phi_{\triangle}(x,y) = a + bx + cy \tag{2.13}$$

Where *a*, *b*, and *c* are constants and are related to each triangular element, so we need to create a profile contains these values for each element.

In FEM, we will use Triangular coordinates since this system provides many advantages in analyzing properties inside elements. A first order trail function can be represented in Triangular coordinate for any point inside any arbitrary element as:

$$\phi_{\triangle}(\xi_1,\xi_2,\xi_3) = \phi_1\xi_1 + \phi_2\xi_2 + \phi_3\xi_3 \tag{2.14}$$

Where arbitrary point *P*(*x*,*y*) inside the triangular element can be represented in triangular coordinates as we can see in Figure 2-2:

$$(x,y) \equiv (\xi_1,\xi_2,\xi_3)$$

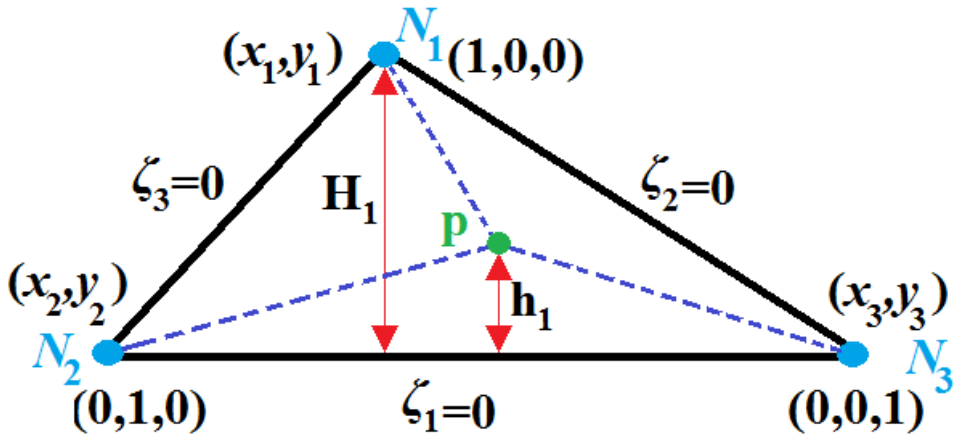

Figure 2-2 Triangular coordinates derivation per element

Triangular coordinate (ξ_1, ξ_2, ξ_3) for any point *P* can be found directly as:

$$\xi_k = \frac{h_k}{H_k} \tag{2.15}$$

Where: *k* represents vertex, and facing edge number as: 1,2 and 3. H_k is the shortest distance from vertex *k* to the facing edge while h_k is the shortest distance from point *P* to related edge.

(ξ_1, ξ_2, ξ_3) should be derived for each element. So, three equations will be needed to get these values so that we can find the values for each trial function for each element as in equation (2.9).

Using linear interpolation, the Cartesian coordinates for point *P* within the triangular element can be written as:

$$x = x_1\xi_1 + x_2\xi_2 + x_3\xi_3 \tag{2.7}$$

$$y = y_1\xi_1 + y_2\xi_2 + y_3\xi_3 \tag{2.8}$$

The third equation can be found from the summation of the three sub-triangles areas that resulted from the point of interest *P* and the vertices (N_1, N_2 and N_3) of the triangle where the area is:

$$S = \frac{1}{2} H_n N_{ij} \tag{2.9}$$

Where: *n, i* and *j* are cyclic permutation of :1, 2 and 3. $N_{ij}=N_{ji}$ is the length of the edge that faces N_n and between vertices N_i and N_j.

$$S = \sum_{n=i}^{3} \frac{1}{2} h_n N_{ij} \tag{2.10}$$

From the definitions of (ξ_1, ξ_2, ξ_3) in equation (2.9) we can write equation (2.19) as:

$$S = \sum_{n=i}^{3} \frac{1}{2} H_n \xi_n N_{ij} \tag{2.20}$$

Using (2.20) we can find the third equation as:

$$1 = \xi_1 + \xi_2 + \xi_3 \tag{2.21}$$

Now, we can find the triangular coordinates (ξ_1, ξ_2, ξ_3) in each element by solving the algebraic equations (2.16), (2.17) and (2.21) as:

$$\begin{bmatrix} 1 \\ x \\ y \end{bmatrix} = \begin{bmatrix} 1 & 1 & 1 \\ x_1 & x_2 & x_3 \\ y_1 & y_2 & y_3 \end{bmatrix} \begin{bmatrix} \xi_1 \\ \xi_2 \\ \xi_3 \end{bmatrix} \tag{2.22}$$

Then solving the previous system of equations in (2.21) as:

$$\begin{bmatrix} \xi_1 \\ \xi_2 \\ \xi_3 \end{bmatrix} = \begin{bmatrix} 1 & 1 & 1 \\ x_1 & x_2 & x_3 \\ y_1 & y_2 & y_3 \end{bmatrix}^{-1} \begin{bmatrix} 1 \\ x \\ y \end{bmatrix} \tag{2.23}$$

Using Cramer's Rule to find the inverse of the matrix as:

$$\begin{bmatrix} \xi_1 \\ \xi_2 \\ \xi_3 \end{bmatrix} = \frac{\begin{bmatrix} \begin{vmatrix} x_2 & x_3 \\ y_2 & y_3 \end{vmatrix} & \begin{vmatrix} 1 & 1 \\ y_3 & y_2 \end{vmatrix} & \begin{vmatrix} 1 & 1 \\ x_2 & x_3 \end{vmatrix} \\ \begin{vmatrix} x_3 & x_1 \\ y_3 & y_1 \end{vmatrix} & \begin{vmatrix} 1 & 1 \\ y_1 & y_3 \end{vmatrix} & \begin{vmatrix} 1 & 1 \\ x_3 & x_1 \end{vmatrix} \\ \begin{vmatrix} x_1 & x_2 \\ y_1 & y_2 \end{vmatrix} & \begin{vmatrix} 1 & 1 \\ y_2 & y_1 \end{vmatrix} & \begin{vmatrix} 1 & 1 \\ x_1 & x_2 \end{vmatrix} \end{bmatrix}}{\Delta} \begin{bmatrix} 1 \\ x \\ y \end{bmatrix} \tag{2.24}$$

Where:

$$\Delta = \begin{vmatrix} 1 & 1 & 1 \\ x_1 & x_2 & x_3 \\ y_1 & y_2 & y_3 \end{vmatrix}$$

So, each of the three triangular coordinates will be:

$$\xi_1 = \frac{\left(\left(x_2 y_3 - x_3 y_2\right) + x\left(y_2 - y_3\right) + y\left(x_3 - x_2\right)\right)}{\Delta} \tag{2.25}$$

$$\xi_2 = \frac{\left(\left(x_3 y_1 - x_1 y_3\right) + x\left(y_3 - y_1\right) + y\left(x_1 - x_3\right)\right)}{\Delta} \tag{2.26}$$

$$\xi_3 = \frac{\left(\left(x_1 y_2 - x_2 y_1\right) + x\left(y_1 - y_2\right) + y\left(x_2 - x_1\right)\right)}{\Delta} \tag{2.11}$$

Therefore, we can write general equation for finding the triangular coordinates within any element in our domain as in equation (2.28):

$$\xi_i = \frac{a_i + b_i x + c_i y}{\Delta} \tag{2.12}$$

Where:

$$a_i = \left(x_{i1} y_{i2} - x_{i2} y_{i1}\right)$$

$$b_i = \left(y_{i1} - y_{i2}\right)$$

$$c_i = \left(x_{i2} - x_{i1}\right)$$

And:

$$i1 = \left(i \mod 3\right) + 1$$

$$i2 = \left(i1 \mod 3\right) + 1$$

We can define: i= 1, 2 and 3 referring to the triangular coordinate system that we are working on now. For three-dimensional system i will be extended to 4.

Now, we can find the first order trial function $\phi_{\triangle}\left(\xi_1, \xi_2, \xi_3\right)$ in terms of Cartesian coordinates using equation (2.22) in each triangular element as taken from equation (2.8).

Keeping in mind that $A\left(x, y\right)$ is the potential at any point P in all elements (the entire domain), $\phi_{\triangle}\left(\xi_1, \xi_2, \xi_3\right)$ is the first order trail function which gives an approximate value for the potential

inside a specific element using nodal potentials at N_1, N_2 and N_3 ; ϕ_1, ϕ_2 and ϕ_3 for this element as shown in Figure 2-2.

This can be verified by considering that the triangular coordinates of the three nodes of the triangle are (1,0,0), (0,1,0) and (0,0,1). By substituting these points, one will get ϕ_1, ϕ_2 and ϕ_3 as the potentials and a linear variation of potentials along any given line inside a triangle. This trial function also provides a continuous variation of potentials from triangle to triangle and a continuous first derivative from triangle to triangle along the tangential direction of the boundary. And these potentials and their related derivatives will be the source for deriving the two-dimensional FEM Solver for such problems.

Equation (2.8) can be written as:

$$\phi_{\triangle} = \{\phi\}^t \{\alpha\} \tag{2.13}$$

Where:

$$\{\phi\}^t = [\phi_1 \quad \phi_2 \quad \phi_3] \tag{2.30}$$

$$\{\alpha\} = \begin{bmatrix} \xi_1 \\ \xi_2 \\ \xi_3 \end{bmatrix} = \begin{bmatrix} \dfrac{a_1 + b_1 x + c_1 y}{\Delta} \\ \dfrac{a_2 + b_2 x + c_2 y}{\Delta} \\ \dfrac{a_3 + b_3 x + c_3 y}{\Delta} \end{bmatrix} \tag{2.31}$$

Therefore, we can write (2.29) as:

$$\phi_{\triangle} = \begin{bmatrix} \phi_1 & \phi_2 & \phi_3 \end{bmatrix} \begin{bmatrix} \dfrac{a_1 + b_1 x + c_1 y}{\Delta} \\ \dfrac{a_2 + b_2 x + c_2 y}{\Delta} \\ \dfrac{a_3 + b_3 x + c_3 y}{\Delta} \end{bmatrix} \tag{2.32}$$

$$= \phi_1 \frac{a_1 + b_1 x + c_1 y}{\Delta} + \phi_2 \frac{a_2 + b_2 x + c_2 y}{\Delta} + \phi_3 \frac{a_3 + b_3 x + c_3 y}{\Delta}$$

According to equation (2.12) we need to find the derivative for $\phi_{\triangle}$ per each element with respect to both *x* and *y*. Therefore, we need first to find $\frac{\partial\{\alpha\}}{\partial x}$ and $\frac{\partial\{\alpha\}}{\partial y}$ as:

$$\frac{\partial\{\alpha\}}{\partial x} = \begin{bmatrix} \frac{\partial \xi_1}{\partial x} & \frac{\partial \xi_2}{\partial x} & \frac{\partial \xi_3}{\partial x} \end{bmatrix}^t = \frac{1}{\Delta} \begin{bmatrix} b_1 & b_2 & b_3 \end{bmatrix}^t = \{b\} \tag{2.33}$$

$$\frac{\partial\{\alpha\}}{\partial y} = \begin{bmatrix} \frac{\partial \xi_1}{\partial y} & \frac{\partial \xi_2}{\partial y} & \frac{\partial \xi_3}{\partial y} \end{bmatrix}^t = \frac{1}{\Delta} \begin{bmatrix} c_1 & c_2 & c_3 \end{bmatrix}^t = \{c\} \tag{2.34}$$

These two equations are referred to as first order differentiation matrices

Now, we can find both $\frac{\partial \phi_{\triangle}}{\partial x}$ and $\frac{\partial \phi_{\triangle}}{\partial y}$ as:

$$\frac{\partial \phi_{\triangle}}{\partial x} = \frac{\partial \{\phi\}^t \{\alpha\}}{\partial x} = \{\phi\}^t \frac{\partial\{\alpha\}}{\partial x} = \{\phi\}^t \{b\} \tag{2.35a}$$

$$\frac{\partial \phi_{\triangle}}{\partial y} = \frac{\partial \{\phi\}^t \{\alpha\}}{\partial y} = \{\phi\}^t \frac{\partial\{\alpha\}}{\partial y} = \{\phi\}^t \{c\} \tag{2.35b}$$

We also need to deal with second term of the integral in equation (2.12). Referring to Figure 2-3, we find that $dy=dh_i$,so we can find $\iint_{\Delta} \xi_i dR$ as:

$$\iint_{\Delta} \xi_i dR = \iint_{\Delta} \frac{h_i}{H_i} dxdy = \int_{h_i=0}^{h_i=H_i} \int_{x=x_1}^{x=x_2} \frac{h_i dx dh_i}{H_i}$$
$$= \int_{h_i=0}^{h_i=H_i} (x_2 - x_1) \frac{h_i dh_i}{H_i} = \int_{h_i=0}^{h_i=H_i} b_i \frac{h_i dh_i}{H_i} \qquad (2.36)$$
$$= \int_{h_i=0}^{h_i=H_i} (x_2 - x_1) \frac{h_i dh_i}{H_i} = \int_{h_i=0}^{h_i=H_i} b_i \frac{h_i dh_i}{H_i}$$

From the similarity of the triangles, we can find that:

$$\frac{b_i}{B_i} = \frac{H_i - h_i}{H_i}$$

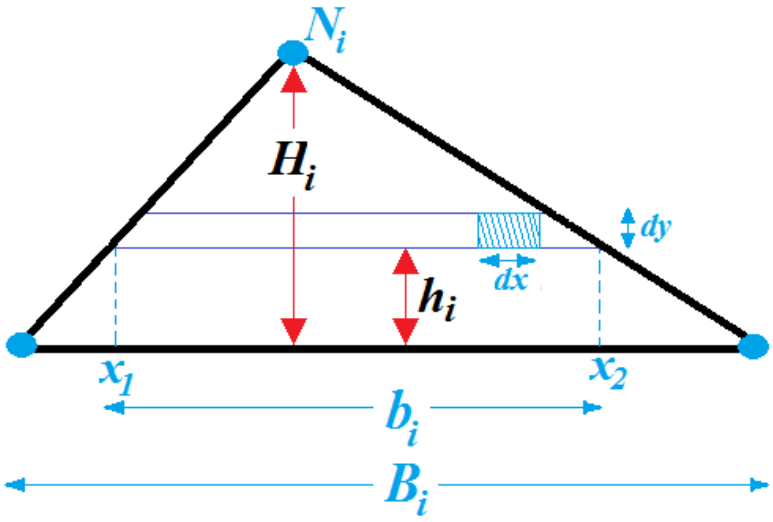

Figure 2-3 Area of trial function in triangular coordinates

So, equation (2.36) can be written as:

$$\iint_{\Delta} \xi_i dR = \int_{h_i=0}^{h_i=H_i} h_i (H_i - h_i) \frac{B_i}{H_i^2} dh_i = \frac{1}{3}\frac{1}{2} H_i B_i = \frac{1}{3}\frac{\Delta}{2} \qquad (2.14)$$

By using the S as the area of the triangular element as: $S = \frac{\Delta}{2}$.

Now, $\iint_{\Delta} \{\alpha\} dR$ can be found as:

$$\begin{aligned}\iint_{\Delta}\{\alpha\}\,dR &= \iint_{\Delta}\begin{bmatrix}\xi_1 & \xi_2 & \xi_3\end{bmatrix}^t dR \\ &= \begin{bmatrix}\iint_{\Delta}\xi_1 dR & \iint_{\Delta}\xi_2 dR & \iint_{\Delta}\xi_3 dR\end{bmatrix}^t \\ &= \begin{bmatrix}\frac{1}{3}S & \frac{1}{3}S & \frac{1}{3}S\end{bmatrix}^t = T^{0,1}S\end{aligned} \tag{2.38}$$

In addition, we can find the total integration for the trial function $\phi_{\vartriangle}$ inside any triangle as:

$$\iint_{\Delta}\phi_{\vartriangle}\,dR = \iint_{\Delta}\{\phi\}^t\{\alpha\}\,dR = \iint_{\Delta}\{\phi\}^t\begin{bmatrix}\frac{1}{3}S & \frac{1}{3}S & \frac{1}{3}S\end{bmatrix}^t dR = \{\phi\}^t T^{0,1}S \tag{2.39}$$

Therefore, the second term of equation (2.12) will be derived from equation (2.39) as we will see in next section, where $T^{0,1} = \begin{bmatrix}\frac{1}{3} & \frac{1}{3} & \frac{1}{3}\end{bmatrix}^t$ is a metric tensor.

2.3 Solution for the Lagrange Functional

Now, we can return to original Lagrange function in (2.12). The solution region has been divided into triangles. Therefore, the total energy can be written as the sum of the energies of each individual triangle as:

$$L[\phi_{\vartriangle}] = \sum_{\forall\Delta}\left(\iint_{\Delta}\left(\frac{\upsilon}{2}(\nabla\phi_{\vartriangle})^2 - J\phi_{\vartriangle}\right)dR\right) \tag{2.40}$$

For the first term in (2.34):

$$\nabla\phi_{\vartriangle} = \hat{x}\frac{\partial\phi_{\vartriangle}}{\partial x} + \hat{y}\frac{\partial\phi_{\vartriangle}}{\partial y} \tag{2.41}$$

$$(\nabla\phi_{\vartriangle})^2 = \left(\hat{x}\frac{\partial\phi_{\vartriangle}}{\partial x} + \hat{y}\frac{\partial\phi_{\vartriangle}}{\partial y}\right)^2 = \left(\hat{x}\frac{\partial\phi_{\vartriangle}}{\partial x} + \hat{y}\frac{\partial\phi_{\vartriangle}}{\partial y}\right)\bullet\left(\hat{x}\frac{\partial\phi_{\vartriangle}}{\partial x} + \hat{y}\frac{\partial\phi_{\vartriangle}}{\partial y}\right) \tag{2.42}$$

So $\iint_{\Delta}\left[\frac{\upsilon}{2}(\nabla\phi_{\vartriangle})^2\right]dR$ will be:

$$\iint_{\Delta}\left[\frac{\upsilon}{2}\left(\nabla\phi_{\vartriangle}\right)^2\right]dR=\iint_{\Delta}\frac{\upsilon}{2}\left[\left(\frac{\partial\phi_{\vartriangle}}{\partial x}\right)^2+\left(\frac{\partial\phi_{\vartriangle}}{\partial y}\right)^2\right]dR$$

$$\iint_{\Delta}\left[\frac{\upsilon}{2}\left(\nabla\phi_{\vartriangle}\right)^2\right]dR=\iint_{\Delta}\frac{\upsilon}{2}\left[\left(\frac{\partial\{\phi\}^t\{\alpha\}}{\partial x}\right)^2+\left(\frac{\partial\{\phi\}^t\{\alpha\}}{\partial y}\right)^2\right]dR$$

$$\iint_{\Delta}\left[\frac{\upsilon}{2}\left(\nabla\phi_{\vartriangle}\right)^2\right]dR=\iint_{\Delta}\frac{\upsilon\{\phi\}}{2}\left[\left(\frac{\partial\{\alpha\}}{\partial x}\right)^2+\left(\frac{\partial\{\alpha\}}{\partial y}\right)^2\right]\{\phi\}^t\,dR$$

$$\iint_{\Delta}\left[\frac{\upsilon}{2}\left(\nabla\phi_{\vartriangle}\right)^2\right]dR=\frac{\upsilon\{\phi\}}{2}S\left[\{b\}\{b\}^t+\{c\}\{c\}^t\right]\{\phi\}^t \tag{2.43}$$

Since we have already the solution for the second term of equation (2.12), then we can write an element Lagrange Function as:

$$L\left[\phi_{\vartriangle}\right]_{\Delta}=0.5\{\phi\}^t\left[P\right]^L\{\phi\}-\{\phi\}^t\{q\} \tag{2.44}$$

Where:

$$\{q\}=JS\begin{Bmatrix}\frac{1}{3}\\ \frac{1}{3}\\ \frac{1}{3}\end{Bmatrix} \tag{2.45}$$

$$\left[P\right]^L=\upsilon S\left[\{b\}\{b\}^t+\{c\}\{c\}^t\right]=\upsilon S\begin{bmatrix}b_1^2+c_1^2 & b_1b_2+c_1c_2 & b_1b_3+c_1c_3\\ b_2b_1+c_2c_1 & b_2^2+c_2^2 & b_2b_3+c_2c_3\\ b_3b_1+c_3c_1 & b_3b_2+c_3c_2 & b_3^2+c_3^2\end{bmatrix} \tag{2.46}$$

Where we can now find programmable close form for $[P]^L$ as:

$$\left[P\right]^L=\upsilon S\begin{bmatrix}b_1^2+c_1^2 & b_1b_2+c_1c_2 & b_1b_3+c_1c_3\\ b_2b_1+c_2c_1 & b_2^2+c_2^2 & b_2b_3+c_2c_3\\ b_3b_1+c_3c_1 & b_3b_2+c_3c_2 & b_3^2+c_3^2\end{bmatrix} \tag{2.47}$$

In addition, $\{\phi\}$ was defined in equation (2.29).

To get a solution for the total domain we should minimize total $L\{\tilde{\phi}\}$ with respect $\{\phi\}^t$ after finding the total energy for all elements as:

$$\frac{\partial}{\partial\{\phi\}^t} L[\phi_\triangle] = \frac{\partial}{\partial\{\phi\}^t} \sum_{\forall\Delta} \frac{1}{2}\left[\{\phi\}^t [P]^L \{\phi\} - \{\phi\}^t \{q\}^L\right] \tag{2.48}$$

To get the solution for the values of $\phi_\triangle$ at the nodes for all elements, then equation (2.42) should be solved.

$$\frac{\partial}{\partial\{\phi\}^t} L[\phi_\triangle] = \frac{\partial}{\partial\{\phi\}^t} \sum_{\forall\Delta} \frac{1}{2}\left[\{\phi\}^t [P]^L \{\phi\} - \{\phi\}^t \{q\}^L\right]$$

$$\frac{\partial}{\partial\{\phi\}^t} L[\phi_\triangle] = 0$$

$$\frac{\partial}{\partial\{\phi\}^t} L\{\phi_\triangle\} = \sum_{\forall\Delta}\left[[P]^L \{\phi\} - \{q\}^L\right] = 0 \tag{2.15}$$

Therefore, the final solution can be obtained by solving:

$$\sum_{\forall\Delta}^{Total} [P]^L \{\phi\} = \sum_{\forall\Delta}^{Total} \{q\}^L \tag{2.50}$$

In addition, the equation solved algebraically for $\{\phi\}$ after doing the assembly process for the local matrices for $[P]^L$ and $\{q\}^L$ according to the global scheme of node numbering that used for generating the elements.

FEM analysis provides the solution to equation (2.50) by applying certain boundary conditions. The local matrices of elements will be added to the corresponding position of the global matrix to be solved for potential values at all nodes, $\{\Phi\}^{total}$ .This leads to the FEM matrix equation:

$$[P]^G \{\Phi\}^{total} = \{Q\}^G \tag{2.51}$$

The solution for (2.51) can be found in any numerical technique like LU Decomposition [95, 118]. Where we will sum and add the local matrices of $[P]^L$ per each elements as we will do for the local vectors $\{q\}^L$ so that we can have our final and global matrix $[P]^G$ and vector $\{Q\}^G$ that contains all the data for the elements of the system. The solution will be $\{\Phi\}^{total}$ that contains the values of the known nodes that will be used to find the values of the unknown nodes.

2.4 Finite Element Computation for Two-Dimensional Eddy Current Problems

Eddy Current Problems are considered as quasi-static problems. Therefore, solving Eddy Current problems will be started as we did for solving magnetostatic problems since both can be derived from Maxwell's equations for low frequency problems in magnetostatic. If time variation is introduced, the resulting magnetic field does affect the initial electric field as for static problems where we neglect the effect of varying fields. Let us consider Maxwell's equations again (2.1-2.4), the non-divergent $\overline{B}$ may be modelled by a vector potential $\overline{A}$ as in equation (2-9);

$$\nabla \times \overline{E} = -\frac{\partial \overline{B}}{\partial t} = -\frac{\partial \nabla \times \overline{A}}{\partial t} \tag{2.52}$$

$$\nabla \times \overline{E} = \nabla \times \left(-\frac{\partial \overline{A}}{\partial t} \right) \tag{2.53}$$

The two vectors $\overline{E}$ and $-\frac{\partial \overline{A}}{\partial t}$ have the same curl, which is possible only if:

$$\overline{E} = -\frac{\partial \overline{A}}{\partial t} - \nabla \varphi \tag{2.54}$$

It is realized that the term $-\nabla\varphi$ is the externally imposed electric field driving the current and $-\frac{\partial \overline{A}}{\partial t}$ is the induced electric field. Combining equations (2.5) and (2.3), substituting (2.6), (2.8) and (2.54),

$$\nabla \times \overline{H} = \overline{J} = \sigma_e \overline{E} \tag{2.55}$$

So that

$$\nabla \times \overline{H} = \sigma_e \left(-\frac{\partial \overline{A}}{\partial t} - \nabla \varphi \right) \tag{2.56}$$

And

$$\nabla \times \frac{1}{\mu} \nabla \times \overline{A} = \sigma_e \left(-\frac{\partial \overline{A}}{\partial t} - \nabla \varphi \right) \tag{2.57}$$

where φ represents the electric potential and using equation (2.9) , then curl of curl for the magnetic vector potential can be represented as:

$$\nabla \times \nabla \times \overline{A} = \nabla \left(\nabla \bullet \overline{A} \right) - \nabla^2 \overline{A} = -\nabla^2 \overline{A} \tag{2.58}$$

Differentiation with respect to time is the equivalent of pre-multiplication by $j\omega$ in phasor representations as and as we did for Magnetostatic Poisson's equation in taking only the *z*-component but in phasor representation for both current density and vector potential as: $\overline{J} = \hat{z}\tilde{J}_0$ and $\overline{A} = \hat{z}\tilde{A}$ respectively and substituting $\nabla \bullet \overline{A}$ =0 in equation (2.58) as:

$$-\frac{1}{\mu}\nabla^2 \tilde{A} = \tilde{J} \ = \sigma_e \tilde{E} = \sigma_e \left[-j\omega \tilde{A} - \nabla \varphi \right] \tag{2.16}$$

This reduces to our final equation

$$-\frac{1}{\mu}\nabla^2\tilde{A} = \tilde{J}_0 - j\omega\sigma_e\tilde{A} \tag{2.60}$$

For eddy current problem, equation (2.60) is the key equation to be solved to find the magnetic vector potential $\tilde{A}$ for a given imposed current density $\tilde{J}_0$. Once we find $\tilde{A}$ **,** the magnetic flux density $\tilde{B}$ can be calculated using equation (2.8). Calculating $\tilde{A}$ from (2.60) using the FEM will be like one solving Magnetostatic problems but we need to add the part that is related to frequency of the imposed current, which means that we will work with phasor representation of fields.

Magnetic fields in a ferromagnetic material can be generated by placing an AC (Alternative Current) coil on top of the material. For AC magnetization, the magnetic vector potential $\tilde{A}$**,** and the exciting current density $\tilde{J}_0$ at angular frequency ω**,** are related by $-\frac{1}{\mu}\nabla^2\tilde{A} = \tilde{J}_0 - j\omega\sigma_e\tilde{A}$ as described in equation (2.60).

The corresponding Lagrange function can be written, like the way we derived for equation (2.12) as:

$$L\left[\tilde{A}\right] = \iint_R \left(\frac{1}{2\mu}\left(\nabla\tilde{A}\right)^2 - \tilde{J}_0\tilde{A} + \frac{1}{2}\, j\omega\sigma_e\tilde{A}^2 \right) dR \tag{2.61}$$

When we divide the total domain to triangular meshes then the total energy can be represented as:

$$L\left[\tilde{\phi}_\triangle\right] = \sum_{\forall\Delta}\left(\iint_\Delta \left(\frac{1}{2\mu}\left(\nabla\tilde{\phi}_\triangle\right)^2 - \tilde{J}_0\tilde{\phi}_\triangle + \frac{1}{2}\, j\omega\sigma_e\tilde{\phi}_\triangle^{\,2} \right) dR \right) \tag{2.62}$$

Where the solution domain *R* will be meshed to triangular elements and a first order two-dimensional trail function can be represented for any point inside these elements as we will see in the following section.

The functional in equation (2.62) contains three terms. The first two terms were solved in detail in the previous section. While the third term, which resulted from the AC current, can be solved as following:

$$\iint_{\Delta}\left(\frac{1}{2}\,j\omega\sigma_e\tilde{\phi}_{\vartriangle}^{\,2}\right)dR=\iint_{\Delta}\left(\frac{1}{2}\,j\omega\sigma_e\left\{\phi\right\}^t\left\{\alpha\right\}\left\{\alpha\right\}^t\left\{\phi\right\}\right)dR \tag{2.63}$$

Where $\{\phi\}^t$ and $\{\alpha\}$ can be found from (2.30) and (2.31) respectively. Then (2.63) will be:

$$\iint_{\Delta}\left(\frac{1}{2}\,j\omega\sigma_e\tilde{\phi}_{\vartriangle}^{\,2}\right)dR=\iint_{\Delta}\left(\frac{1}{2}\,j\omega\sigma_e\begin{bmatrix}\tilde{\phi}_1 & \tilde{\phi}_2 & \tilde{\phi}_3\end{bmatrix}\begin{Bmatrix}\xi_1\\ \xi_2\\ \xi_3\end{Bmatrix}\begin{bmatrix}\xi_1 & \xi_2 & \xi_3\end{bmatrix}\begin{Bmatrix}\tilde{\phi}_1\\ \tilde{\phi}_2\\ \tilde{\phi}_3\end{Bmatrix}\right)dR \tag{2.64}$$

$$\iint_{\Delta}\left(\frac{1}{2}\,j\omega\sigma_e\tilde{\phi}_{\vartriangle}^{\,2}\right)dR=\iint_{\Delta}\left(\frac{1}{2}\,j\omega\sigma_e\begin{bmatrix}\tilde{\phi}_1 & \tilde{\phi}_2 & \tilde{\phi}_3\end{bmatrix}\begin{bmatrix}\xi_1^{\,2} & \xi_1\xi_2 & \xi_1\xi_3\\ \xi_1\xi_2 & \xi_2^{\,2} & \xi_2\xi_3\\ \xi_1\xi_3 & \xi_2\xi_3 & \xi_3^{\,2}\end{bmatrix}\begin{Bmatrix}\tilde{\phi}_1\\ \tilde{\phi}_2\\ \tilde{\phi}_3\end{Bmatrix}\right)dR \tag{2.65}$$

If *S* is the element area and $\tilde{\phi}_{\vartriangle}$ in a triangle element has been written in triangular coordinates, then:

$$\iint_{\Delta}\left(\xi_1^{\,i}\xi_2^{\,j}\xi_3^{\,k}\right)dR=2!\frac{i!\,j!\,k!}{(i+j+k+2)!}S \tag{2.66}$$

By substituting equation (2.66) in (2.65), and rearranging,

$$\iint_{\Delta}\left(\frac{1}{2}\,j\omega\sigma_e\tilde{\phi}_{\Delta}^{\,2}\right)dR=\left(\frac{1}{2}\,j\omega\sigma_e\begin{bmatrix}\tilde{\phi}_1 & \tilde{\phi}_2 & \tilde{\phi}_3\end{bmatrix}\begin{bmatrix}\iint_{\Delta}\xi_1^{\,2}dR & \iint_{\Delta}\xi_1\xi_2 dR & \iint_{\Delta}\xi_1\xi_3 dR\\ \iint_{\Delta}\xi_1\xi_2 dR & \iint_{\Delta}\xi_2^{\,2}dR & \iint_{\Delta}\xi_2\xi_3 dR\\ \iint_{\Delta}\xi_1\xi_3 dR & \iint_{\Delta}\xi_2\xi_3 dR & \iint_{\Delta}\xi_3^{\,2}dR\end{bmatrix}\begin{Bmatrix}\tilde{\phi}_1\\ \tilde{\phi}_2\\ \tilde{\phi}_3\end{Bmatrix}\right)$$

$$\iint_{\Delta}\left(\frac{1}{2}\,j\omega\sigma_e\tilde{\phi}_{\Delta}^{\,2}\right)dR=\frac{1}{2}\,j\omega\sigma_e\left\{\tilde{\phi}\right\}^t\frac{S}{12}\begin{bmatrix}2&1&1\\1&2&1\\1&1&2\end{bmatrix}\left\{\tilde{\phi}\right\} \tag{2.67}$$

Now, we can expand equation (2.62) to be:

$$\begin{aligned}L\left[\tilde{\phi}_{\Delta}\right]_{\Delta}=&\frac{1}{2\mu}S\begin{bmatrix}\tilde{\phi}_1 & \tilde{\phi}_2 & \tilde{\phi}_3\end{bmatrix}\begin{bmatrix}b_1^2+c_1^2 & b_1b_2+c_1c_2 & b_1b_3+c_1c_3\\ b_2b_1+c_2c_1 & b_2^2+c_2^2 & b_2b_3+c_2c_3\\ b_3b_1+c_3c_1 & b_3b_2+c_3c_2 & b_3^2+c_3^2\end{bmatrix}\begin{Bmatrix}\tilde{\phi}_1\\ \tilde{\phi}_2\\ \tilde{\phi}_3\end{Bmatrix}\\ &-\begin{bmatrix}\tilde{\phi}_1 & \tilde{\phi}_2 & \tilde{\phi}_3\end{bmatrix}\tilde{J}_0S\begin{Bmatrix}\frac{1}{3}\\ \frac{1}{3}\\ \frac{1}{3}\end{Bmatrix}+\frac{1}{2}\,j\omega\sigma_e\begin{bmatrix}\tilde{\phi}_1 & \tilde{\phi}_2 & \tilde{\phi}_3\end{bmatrix}\frac{S}{12}\begin{bmatrix}2&1&1\\1&2&1\\1&1&2\end{bmatrix}\begin{Bmatrix}\tilde{\phi}_1\\ \tilde{\phi}_2\\ \tilde{\phi}_3\end{Bmatrix}\end{aligned} \tag{2.68}$$

For the entire domain of the problem, we need to sum (2.68) for all elements as:

$$L\left[\tilde{\phi}_{\vartriangle}\right]=\sum_{\forall\Delta}\left(\begin{array}{c}\frac{1}{2}\left[\tilde{\phi}\right]^{t}\left[\begin{array}{c}\frac{S}{\mu}\begin{bmatrix}b_1^2+c_1^2 & b_1b_2+c_1c_2 & b_1b_3+c_1c_3\\ b_2b_1+c_2c_1 & b_2^2+c_2^2 & b_2b_3+c_2c_3\\ b_3b_1+c_3c_1 & b_3b_2+c_3c_2 & b_3^2+c_3^2\end{bmatrix}\\ +j\omega\sigma_e\frac{S}{12}\begin{bmatrix}2&1&1\\1&2&1\\1&1&2\end{bmatrix}\end{array}\right]\left\{\tilde{\phi}\right\}\\ -\left[\tilde{\phi}\right]^{t}\tilde{J}_0 S\begin{Bmatrix}\frac{1}{3}\\ \frac{1}{3}\\ \frac{1}{3}\end{Bmatrix}\end{array}\right) \tag{2.17}$$

Now we can get a final corresponding equation as:

$$L\left[\tilde{\phi}_{\vartriangle}\right]=\sum_{\forall\Delta}\left(\frac{1}{2}\left\{\tilde{\phi}\right\}^{t}\left[P\right]^{L}\left\{\tilde{\phi}\right\}-\left\{\tilde{\phi}\right\}^{t}\left\{q\right\}\right) \tag{2.70}$$

Where:

$$[P]^L = \frac{S}{\mu}\begin{bmatrix} b_1^2+c_1^2 & b_1b_2+c_1c_2 & b_1b_3+c_1c_3 \\ b_2b_1+c_2c_1 & b_2^2+c_2^2 & b_2b_3+c_2c_3 \\ b_3b_1+c_3c_1 & b_3b_2+c_3c_2 & b_3^2+c_3^2 \end{bmatrix} + j\omega\sigma_e \frac{S}{12}\begin{bmatrix} 2 & 1 & 1 \\ 1 & 2 & 1 \\ 1 & 1 & 2 \end{bmatrix} \tag{2.71}$$

$$\{q\} = \tilde{J}_0 S \begin{bmatrix} \frac{1}{3} \\ \frac{1}{3} \\ \frac{1}{3} \end{bmatrix} \tag{2.72}$$

$$L\left[\tilde{\phi}_{\vartriangle}\right] = \sum_{\forall\Delta}\left(\frac{1}{2}\left\{\tilde{\phi}\right\}^t [P]^L \left\{\tilde{\phi}\right\} - \left\{\tilde{\phi}\right\}^t \{q\}\right) \tag{2.73}$$

To get a solution for the total domain we should minimize $L\left[\tilde{\phi}_{\vartriangle}\right]$ with respect to $\left\{\tilde{A}\right\}^t$ after finding the total energy for all elements from (2.73) as:

$$\frac{\partial}{\partial\left\{\tilde{\phi}\right\}^t} L\left[\tilde{\phi}_{\vartriangle}\right] = \frac{\partial}{\partial\left\{\tilde{\phi}\right\}^t} \sum_{\forall\Delta} \frac{1}{2}\left[\left\{\tilde{\phi}\right\}^t [P]^L \left\{\tilde{\phi}\right\} - \left\{\tilde{\phi}\right\}^t \{q\}\right] \tag{2.74}$$

To get the solution for the values of $\tilde{\phi}_{\vartriangle}$ at the nodes for all elements, then equation (2.75) should be minimized and. Therefore (2.74) will be:

$$\frac{\partial}{\partial\left\{\tilde{\phi}\right\}^t} L\left[\tilde{\phi}_{\vartriangle}\right] = \frac{\partial}{\partial\left\{\tilde{\phi}\right\}^t} \sum_{\forall\Delta} \frac{1}{2}\left[\left\{\tilde{\phi}\right\}^t [P]^L \left\{\tilde{\phi}\right\} - \left\{\tilde{\phi}\right\}^t \{q\}^L\right]$$

$$\frac{\partial}{\partial\left\{\tilde{\phi}\right\}^t} L\left[\tilde{\phi}_{\vartriangle}\right] = 0$$

$$\frac{\partial}{\partial\left\{\tilde{\phi}\right\}^t} L\left[\tilde{\phi}_{\vartriangle}\right] = \sum_{\forall\Delta}\left[[P]^L \left\{\tilde{\phi}\right\} - \{q\}^L\right] = 0 \tag{2.75}$$

Therefore, the final solution can be obtained by solving:

$$\sum_{\forall\Delta}^{Total}[P]^{L}\{\tilde{\phi}\}=\sum_{\forall\Delta}^{Total}\{q\}^{L} \tag{2.76}$$

In addition, the equation solved algebraically for $\{\tilde{\phi}\}$ after doing the assembly process for the local matrices for $[P]^{L}$ and $\{q\}^{L}$ according to the global scheme of node numbering that used for generating the elements.

FEM analysis provides the solution to (2.76) by applying certain boundary conditions. The local matrices of elements will be added to the corresponding position of the global matrix to be solved for $\{\tilde{\phi}\}$. This leads to the FEM matrix equation

$$[P]^{G}\{\Phi\}^{total}=\{Q\}^{G} \tag{2.77}$$

The solution for (2.77) can be found in any numerical technique like LU decomposition. Where we will sum and add the local matrices of $[P]^{L}$ per each elements as we will do for the local vectors $\{q\}^{L}$ so that we can have our final and global matrix $[P]^{G}$ and vector $\{q\}$ that contains all the data for the elements of the system. The solution will be $\{\Phi\}^{total}$ that contains the values of the known nodes that will be used to find the values of the unknown nodes.

2.5 Boundary Conditions

We use two types of boundary conditions, namely Dirichlet and Neumann [3] to solve the system of matrices in equations (2.51) and (2.77). Dirichlet boundary conditions mean that the potential along the boundary is fixed at a given value and Neumann boundary conditions mean the derivative of the unknown potential at the boundary along the normal direction is zero. Dirichlet boundary conditions can be implemented by considering the node points on the boundary to have known

values. Where our objective will be to use any matrix solver to find the values of the *n*-unknown values $\{A_{uk}\}$.

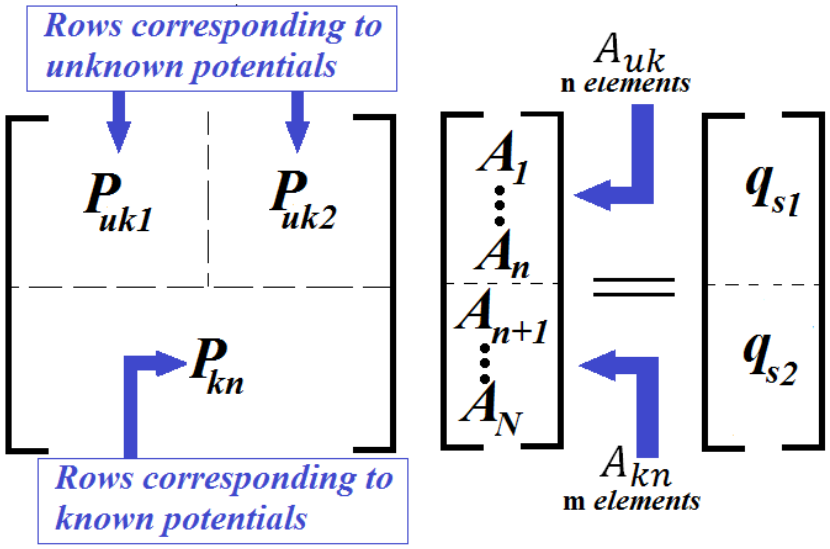

Figure 2-4 FEM solver showing both known and unknown nodes distributions

Figure 2-4 summarizes how we will write our code to solve these equations and how we write our FEM solver by separating known from unknown potentials. LU Choleski decomposition is used as matrix solver and excellent results were achieved.

3 Subregion Method

3.1 Introduction

In our solution, we will use the LU Cheolsky Decomposition Matrix solver. An analogy can be seen from Figure 2-5 between solving both Magnetostatic, Eddy Current and Electrostatic FEM problems [95, 118]. Where in general we can rewrite the governing Poisons equation for Electrostatic problems as:

$$-\varepsilon\nabla^2\varphi = \rho$$

where, ρ is charge density, φ is scaler potential and ε is permittivity. The mapping came from using the same procedure in minimization the functional to end with same equations (2.78) and (2.52), where we can rewrite them as:

$$[P]\begin{Bmatrix}\Phi_{uk}\\ \Phi_{kn}\end{Bmatrix} = \{Q\} \tag{3.1}$$

Where again, [P] and $\{Q\}$ are the global matrices that contain data and properties of the generated elements and physical properties of the problem and $\begin{Bmatrix}\Phi_{uk}\\ \Phi_{kn}\end{Bmatrix}$ will be the scalar potentials vector of the (voltage drops) on each node. Any matrix solver like LU Decomposition can find the values of the unknown potential $\{\Phi_{uk}\}$ given the known potentials $\{\Phi_{kn}\}$ as Dirichlet boundaries through the problem. So, the next step will be to apply the post processing analysis according to the nature of the given problem.

In this chapter, derivations of needed equations that lead to subregions method and how we will use them in designing magnetic devices and solve Magnetostatic problems. These equations will

be improved to solve Eddy Current Problems in order to detect hidden cracks and characterize their shapes.

3.2 Methodology

1) Dividing the area of interest into sub areas, so the whole domain region will be divided into subregions (R_1, R_2, R_3...R_N).

2) Define subregions such like:

   i- Areas where the material parameters have to be modified in the next iteration and solution steps (*it may be one area or more according to the nature of the problem*) and where the calculation results should be saved and recorded at each step; *e.g.* R_1.

   ii- Reminder areas; (all reminder areas else R_1), which we have to deal with computationally only one time. For example, we can define R_2 as separated area as for R_3 as seen in Figure 3-1. However, we will consider that we have two areas in this example: R_1 and $R_2+R_3+R_4$.

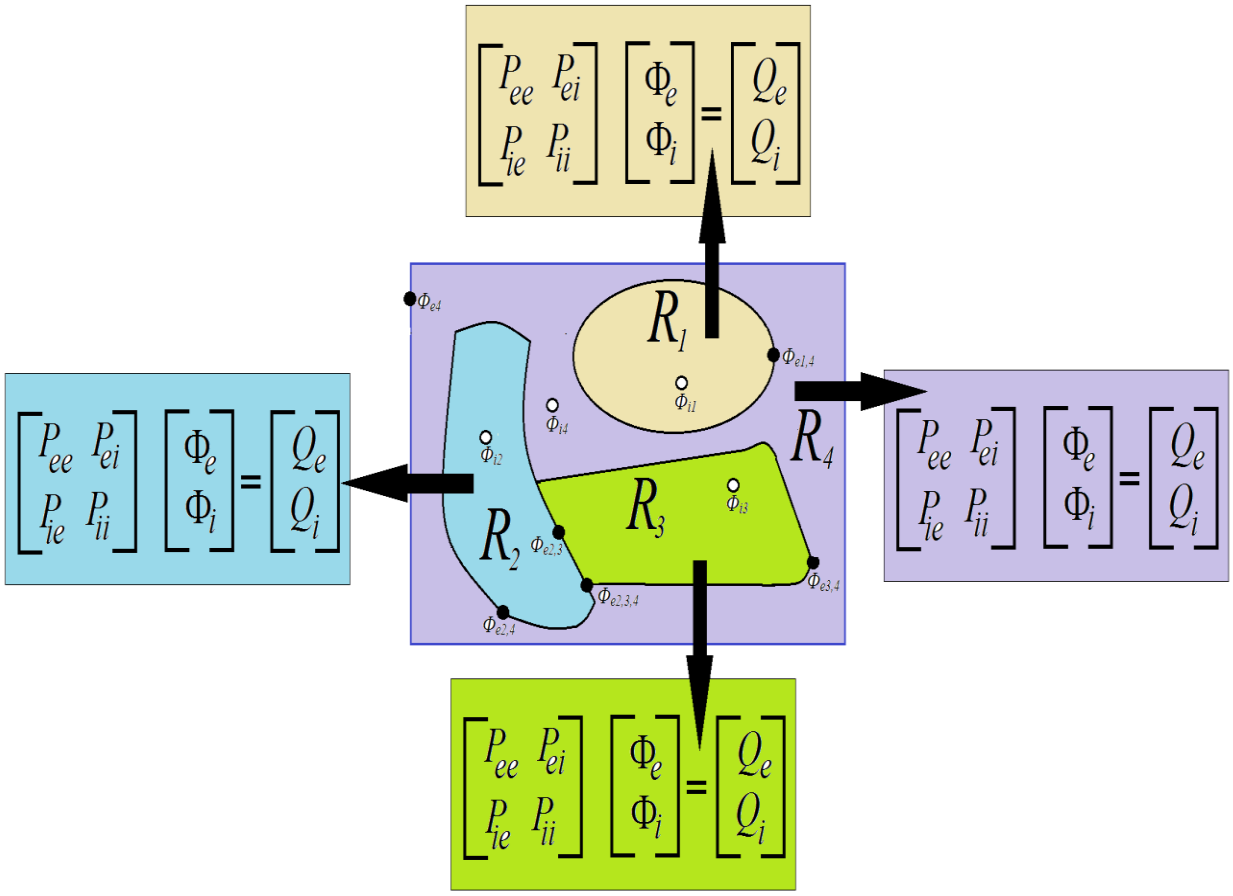

Figure 3-1 Subdivision of the whole solution domain into subregions and interface nodes.

3) Finding the coefficient matrices of the different subregions.

4) Assemble these coefficient matrices separately and reduce them to number of equations related to degrees of freedom that are associated with nodes at subregions interfaces.

5) Finally, the reduced matrices of all subregions will be used to assemble the final global matrix, which will be solved for the reduced system.

Therefore, as much as we repeat solving the associated field problem, we just deal with the desired subregion. This will save computation, time and memory since we deal with reduced system.

3.3 The Subregion Method

In this part, we will show how we will use fundamentals of FEM to solve the field problem using the subregion criteria.

We can now rewrite equation (3.1) in matrix form as in equation (3.2) as a subregional formulation for equation (3.1) as [85]:

$$\begin{bmatrix} P_{ee} & P_{ei} \\ P_{ie} & P_{ii} \end{bmatrix} \begin{Bmatrix} \Phi_e \\ \Phi_i \end{Bmatrix} = \begin{Bmatrix} Q_e \\ Q_i \end{Bmatrix} \tag{3.1}$$

Where equation (3.1) shows the basis of plugging the sub structural analysis in the study of fields by splitting the field into substructures. Where each subregion will have its own subregional matrix-vector of equation (3.1) as shown in Figure 3-1.

The main point of this method is to divide the whole field into number of subdomains. We should be careful about choosing the boundaries, because these boundaries are governed by both the nature of the application and the efficiency of the matrix computations involved. The subscript *e* in equation (3.1) denotes the exterior DOFs along the interfaces between neighboring subregions, as highlighted in Figure 3-1; the DOFs of the interior nodes of the subregion are denoted by the subscript *i*. It should be noticed that the interior nodes are those nodes interior to the subregion where design will change the shape in our FEM solution.

Therefore, for a system contains number of subregions as in Figure 3-1, we have the following nodes:

i- Boundary nodes, such like for usual FEM problems; they may be Dirichlet or Neumann according to the nature of the problem.

ii- Internal or interior nodes and those nodes that are inside the sub-regions.

iii- External or exterior nodes and those nodes are at the boundaries between different sub regions.

Directly from equation (3.1), the first row is:

$$\left[P_{ee}\right]\left\{\Phi_e\right\}+\left[P_{ei}\right]\left\{\Phi_i\right\}=\left\{Q_e\right\} \tag{3.2}$$

$$\left[P_{ie}\right]\left\{\Phi_e\right\}+\left[P_{ii}\right]\left\{\Phi_i\right\}=\left\{Q_i\right\} \tag{3.3}$$

Now, we can continue working on equation (3.4) as:

$$\left[P_{ii}\right]\left\{\Phi_i\right\}=\left\{Q_i\right\}-\left[P_{ie}\right]\left\{\Phi_e\right\} \tag{3.4}$$

From the second row of the partitioned equation (3.1), the potential of the internal DOFs is expressed in terms of the extremal ones as:

$$\left\{\Phi_i\right\}=\left[P_{ii}\right]^{-1}\left\{Q_i\right\}-\left[P_{ii}\right]^{-1}\left[P_{ie}\right]\left\{\Phi_e\right\} \tag{3.5}$$

And this is possible, because the interior fields inside regions are unique since the boundary fields are defined [85].

Inserting the expression for the interior DOFs $\left\{\Phi_i\right\}$ in equation (3.5) into the first row of equation (3.1) will give the reduced matrix equation for the extremal DOFs of the subregion.

Now, we can use equation (3.5) to substitute for $\left\{\Phi_i\right\}$ in equation (3.2) for as:

$$[P_{ee}]\{\Phi_e\}+[P_{ei}]\left\{[P_{ii}]^{-1}\{Q_i\}-[P_{ii}]^{-1}[P_{ie}]\{\Phi_e\}\right\}=\{Q_e\} \tag{3.6}$$

Simplifying (3.6) as:

$$[P_{ee}]\{\Phi_e\}+[P_{ei}][P_{ii}]^{-1}\{Q_i\}-[P_{ei}][P_{ii}]^{-1}[P_{ie}]\{\Phi_e\}=\{Q_e\} \tag{3.7}$$

$$[P_{ee}]\{\Phi_e\}-[P_{ei}][P_{ii}]^{-1}[P_{ie}]\{\Phi_e\}=\{Q_e\}-[P_{ei}][P_{ii}]^{-1}\{Q_i\} \tag{3.8}$$

The exterior DOFs $\{\Phi_e\}$ can be represented as:

$$\left[[P_{ee}]-[P_{ei}][P_{ii}]^{-1}[P_{ie}]\right]\{\Phi_e\}=\left\{\{Q_e\}-[P_{ei}][P_{ii}]^{-1}\{Q_i\}\right\} \tag{3.9}$$

Where, now we can define new expressions for the subregion parameters as:

$$[P_{sr}]=[P_{ee}]-[P_{ei}][P_{ii}]^{-1}[P_{ie}] \tag{3.10}$$

$$[P_{sr}]=[P_{ee}]-[P_{ei}][A] \tag{3.11}$$

where:

$$[A]=[P_{ii}]^{-1}[P_{ie}] \tag{3.12}$$

$$\{Q_{sr}\}=\{Q_e\}-[P_{ei}]\left\{[P_{ii}]^{-1}\{Q_i\}\right\} \tag{3.13}$$

$$\{Q_{sr}\}=\{Q_e\}-[P_{ei}]\{\Phi_{io}\} \tag{3.14}$$

where:

$$\{\Phi_{io}\}=[P_{ii}]^{-1}\{Q_i\} \tag{3.15}$$

Using (3.10-3.16), the coefficient matrices and the excitation vectors on the right-hand side are combined to yield the subregion matrices reduced to the exterior DOFs:

$$[P_{sr}]\{\Phi_e\} = \{Q_{sr}\} \tag{3.16}$$

The modification matrix [*A*], as well as the vector $\{\Phi_{io}\}$ are not obtained by explicit inversion of the coefficient matrix associated with the interior DOFs, but rather by symmetric triangular Choleski Decomposition of [P_{ii}] with subsequent forward and backward substitution with the columns of [P_{ie}]and $\{Q_i\}$ as the right-hand side:

$$[P_{ii}]\{[A]\{\Phi_{io}\}\} = \{[P_{ei}]\{Q_i\}\} \tag{3.17}$$

Therefore, we have now to compute both of [*A*] and $\{\Phi_{io}\}$ from (3.13) and (3.16) respectively by using the symmetric triangular Choleski Decomposition, but first, there are some important properties of the off-diagonal rectangular partition [P_{ie}] and its transpose [P_{ei}]:

1- They are representing the connectivity of the exterior with the interior DOFs.

2- They exhibit sparsity, with only as many non-zero entries in a column as interior nodes are connected to the exterior node of this column; where, this sparsity pattern those partitions is utilized in a column wise calculation of [*A*].

3- The forward and backward substitutions involved in equation (3.18) are carried out only for row numbers higher than the column number of the first non-zero entry in the corresponding row of the sparse matrix [P_{ei}].

So, the important steps now are to find both of [*A*] and $\{\Phi_{io}\}$.

The solution $\{\Phi_{io}\}$ is essentially the potential distribution within the subregion due to all interior field sources and the application of Dirichlet boundary conditions of zero at all external nodes, which is equivalent to isolating this subregion completely from its neighbors.

It is supposed that we have both of [*A*] and $\{\Phi_{io}\}$ for each subregion. Now the next step is to find the condensed matrices [P_{sr}] and vectors [Q_{sr}]for each of the *N*- subregions (*by considering that we have N- subregions*). These nodes and related matrices are clear in Figure 3-2 for different subregions.

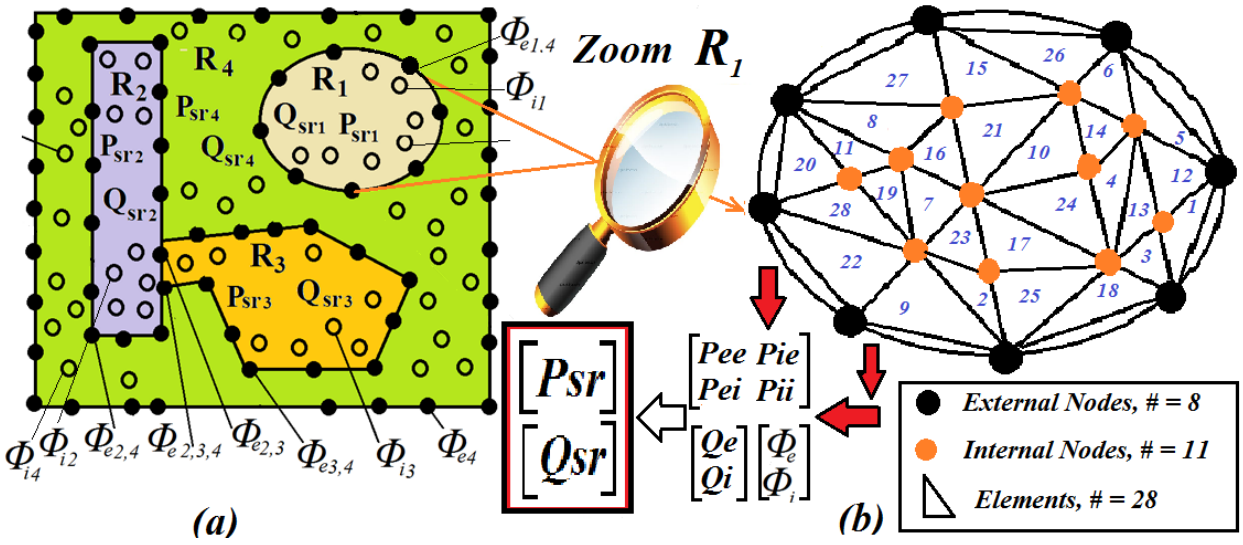

Figure 3-2 Explanation of subregion division

Now, both condensed matrices [P_{sr}] and vectors [Q_{sr}] are assembled into the residual equation for all external DOFs in the same way that the global FEM matrix was assembled from the local element matrices:

$$\left[P_{res}\right]\left\{\Phi_{res}\right\} = \sum_{j=1}^{N}\left\{\left[P_{sr}\right]_j \left\{\Phi_e\right\}_j\right\} = \sum_{j=1}^{N}\left\{Q_{sr}\right\}_j = \left\{Q_{res}\right\} \tag{3.18}$$

This residual equation represents the whole solution domain reduced to the DOFs at the interfaces of all subregions; i.e. all $\left\{\Phi_e\right\}$'s for all subregions. If our design contains just only one subregion of interest, then N=1 in (3.18).

Having computed the solution $\left\{\Phi_{res}\right\}$ of the residual, the data recovery for the interior potential distribution is performed for each subregion separately using equation (3.5). The unreduced, complete equation for the full solution region of (3.1) is thus never assembled and solved. Instead, the solution of the whole system is replaced by the solution of several subsystems of significantly smaller size.

From Figure 3-2, we can now define and understand how to divide the nodes of the given problem into both internal and external nodes. In this figure, we have a little bit complicated and more detailed shape that contains 4 different subregions (R_1, R_2, R_3 and R_4) that all together form the main region. In subregional FEM solution, we start as regular FEM solution, so we can summarize the SFEM solution problems by:

1- Define the problem parameters and start doing the usual pre-processing FEM and use any mesh generation to generate meshes (nodes, elements) to the given problem. hand written mesh generation is used in these explaining examples while other mesh generation techniques as in [117] are used for more complicated problems.

2- Define the regions of the given problem according to given parameters. We define the coordinates and the physical properties for each subregion as in the example in Figure 3-2, we see we have 4 regions, so we need to define the coordinates for each region, for

example, the green area is related to R_4. The other important parameters are the physical parameters for each region, because they are included in the solution of the FEM problem. For example, in Electrostatic solution, permittivity and charge density should be defined for each subregion, while in Magnetostatic problems, permeability and current charge density will be defined for each subregion. This is the core for subregion method; to define the subregion that we want to focus our FEM solution on within our coding. Again, we have now 4 subregions in our example which are (R_1, R_2, R_3 and R_4).

3- Defining subregions is not enough in our analysis, now we must define both the internal and external nodes for each subregion. This step is very important and critical because we will now define these nodes based on the numbering scheme that we used when we generate the nodes [117]. For each subregion, R_1 , the external nodes are those surrounding nodes that surround that region; or in other words those nodes are the interfacing nodes with the other regions, so they may be mutual with other regions. We can see that $\Phi_{e1,4}$ is an example of an external node for R_1 but also it can be considered as an external node for R_4 since it is on the interface between R_1 and R_4 . While R_4 has more external nodes with more than one region as shown in the Figure 3-2. $\Phi_{e3,4}$ and $\Phi_{e2,4}$ are both examples for external nodes between R_4 and both R_2 and R_3 respectively. It is important to know that also Φ_{e4} can be considered as an example of external node for R_4 , because it surrounds this region and bounds it. Now these boundary nodes will be taken in our solution according to their values and whether if they are Dirichlet or Neumann boundary conditions. The internal nodes are those nodes within the subregion and belongs exclusively to that region, so they cannot be found in other regions. These nodes are unique

within each subregion. An examples of the internal nodes are Φ_{i1}, Φ_{i2} , Φ_{i3} and Φ_{i4} in (R_1, R_2, R_3 and R_4) respectively.

4- The next step is to start doing FEM analysis but for each subregion such like in Figure 3-2b, and after that assembly all the solutions for each subregion to get the final answer. To give more details about this point let us take the zoomed R_1 again in Figures 3-2b and 3-3a, now, we deal with R_1 as individual problem. We have the following for this region:

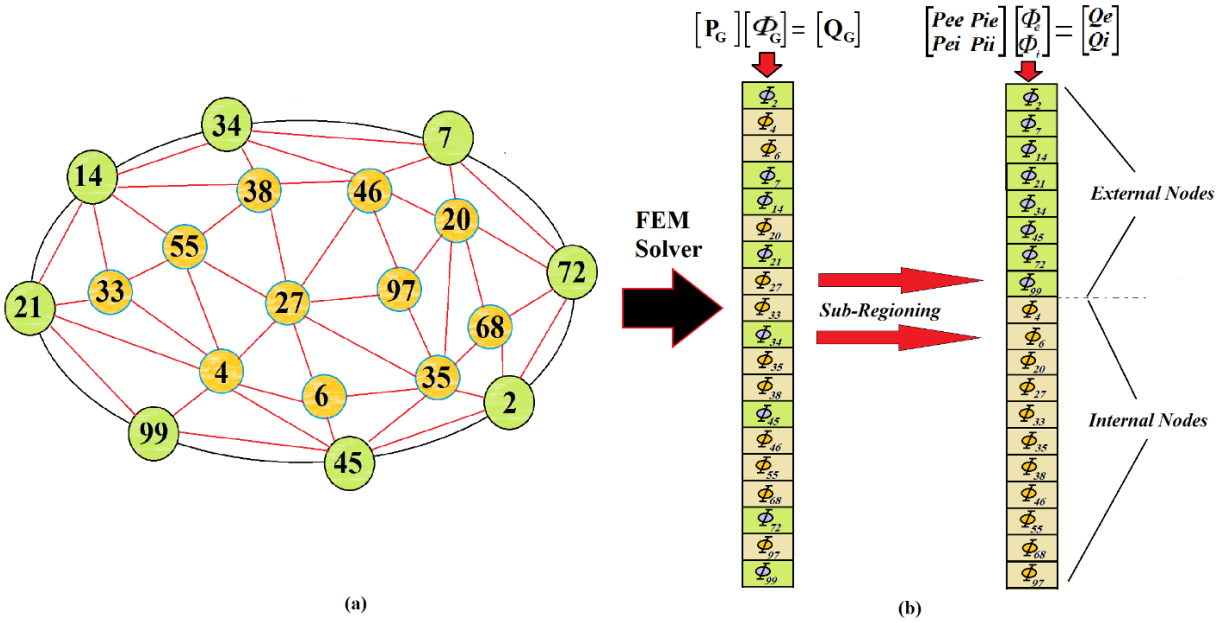

Figure 3-3 Arranging external and internal nodes. (a) Example of subregion with both exterior and interior nodes. All these nodes considered to be unknown nodes. (b) How potentials are arranged in subregional order; exterior nodes first, then interior nodes.

i- We have a bounded region and can be considered as separated region R_1.

ii- Mesh generation was done for this region, so we have related nodes and elements for this region. We can find that this region contains 18 nodes and 28 elements. We can use any mesh generator to do meshing. Now the important thing is that these nodes which map this region should be divided into two categories as defined earlier in this chapter; into both external and internal nodes. In this example, we

have a total of 18 global nodes divided into 10 internal nodes and 8 external nodes**.** The critical thing is that we save the original node numbering scheme, so that we use it again in arranging these nodes into internal and external as in Figure 3-3b.

iii- Now we can use ii to define the new inputs for our FEM solver, we have two inputs: *Coordinate_ Matrix_ One* which contains the coordinates for each node in R_1, which means we will have a 19 by 2 matrix for the coordinates for this region, and each row will be the *x* and *y* coordinates for each node for R_1 respectively. The second input will be the *Data_ Matrix_ One* which is the connectivity matrix that contains the relation between elements and related nodes and define physical properties within each element. The matrix for R_1 in Figure 3-2b will be 28 by 5, where each row will correspond to each element in R_1 and the first three columns will represent the nodes numbering scheme and the reminder two column will be saved for defining the physical properties and give numeric values for these quantities in each individual element.

iv- So, the inputs for our FEM solver will be derived. We can do all the FEM analysis but for each subregion alone as we did for R_1. For example, the system in Figure 3-2a contains 4 subregions, which means that we will do FEM analysis for each subregion after taking boundary conditions in our consideration. Therefore, 4 different global matrices and vectors will be the result, where for each subregion (arbitrary subregion *j*), $[P]_j = \begin{bmatrix} P_{ee} & P_{ei} \\ P_{ie} & P_{ii} \end{bmatrix}_j$ and $\{Q\}_j = \begin{Bmatrix} Q_e \\ Q_i \end{Bmatrix}_j$ as in equation (3.2).

v- This step will be similar to regular FEM analysis, but we will assembly regions instead of elements. As derived in (3.12) and (3.15) , we will derive $[P_{sr}]_j$ and

$\{Q_{sr}\}_j$ for each subregion and use (3.19) to assembly in the final *Global_ Region_ Matrix* and *Global_ Region_ Vector*. Let us take the three subregion example in Figure 3-4, we can now see how the $[P_{sr}]_1$, $[P_{sr}]_2$ are $[P_{sr}]_3$ are assembled in the complete $[P_{sr}]$ matrix to get the solution for the external nodes between the subregions.

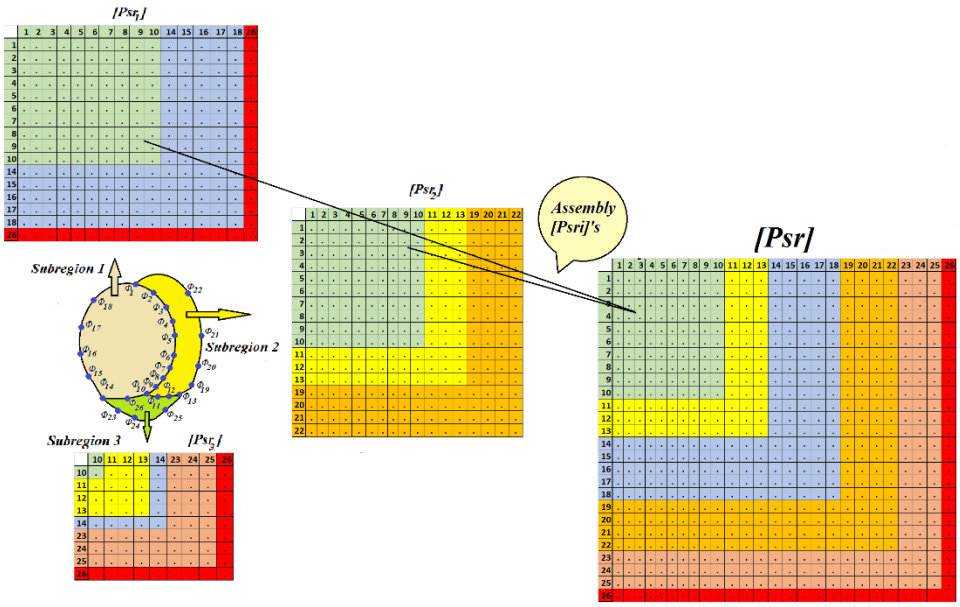

Figure 3-4 Assembly regions to whole domain.

vi- We will now find the values for all the external nodes $\{\Phi_e\}$ for all subregions from solving *Global_ Region_ Matrix* and *Global_ Region_ Vector*. We may use regular matrix solver built in functions in Matlab or numerical techniques for big size problems.

vii- After finding the external nodes for all the system $\{\Phi_e\}$, we can now go to each subregion (arbitrary *subregion j*) individual $\{\Phi_i\}_j$ to find its related internal nodes.

4 Elasticity Mesh Generation Method

4.1 Introduction

One of the outcomes for this project is to detect the hidden cracks within metals, then to evaluate theirs effect, so we can evaluate wither this defect is major or not. The objective for this chapter is for developing a FEM mesh generator that can fit SFEM which separates crack region from the entire domain. Using subregion method with classical FEM analysis will be very hard in case we use an adaptive mesh generator as in [117] that will generate new meshes every time with new numbers and connectivity matrix for the entire domain. The reason of that because we want to keep the same exterior nodes positions between regions. Because these exterior nodes working as an interface between different connecting regions and we should save them. An elastic mesh generating scheme should be used in this case, so that we can detect nodes of interest, then, play with these nodes by changing their positions and keeping the connectivity matrix without any change.

One of the most critical issues in inverse problems is how to choose design parameters and apply optimization in order to get the optimal parameters that fit minimum or maximum of the fitness score. In Eddy Current Problems and especially in the process of detecting and characterizing defects, it is necessary to implement a flexible mesh generator that can be updated each iteration. [114] presented a criterion for changing meshes for design sensitivity computation while preserving continuity of the object function. It was shown to be applicable to various kinds of linear changes of multiple parameters that combine to model changes of nodes, lines and objects in designing poles in Magnetostatic problems. This generator allows repeated solutions with iterated meshes so that it can be employed in a first-order optimization strategy exploiting its faster convergence. This chapter will explain this algorithm through some examples. While, this method

is improved by using it with SFEM in order to solve inverse Eddy Current problems and characterize defects. New defect pattern will be generated each iteration until obtaining the real defect pattern.

4.2 Moving Single Node

By knowing an initial location of the defect, we can isolate this location from the entire problem to reshape the defect. Selecting the design parameters as our master nodes [114]. Then move these nodes within the defect region only (R_2) will grantee that. Moving these master or design nodes will be the source of moving the reminder interior nodes ($A^i_{R_2}$) within R_2. We will consider these reminder interior nodes within R_2 as relative nodes. Figure 4-1 shows these nodes in addition of the external nodes for the region R_2.

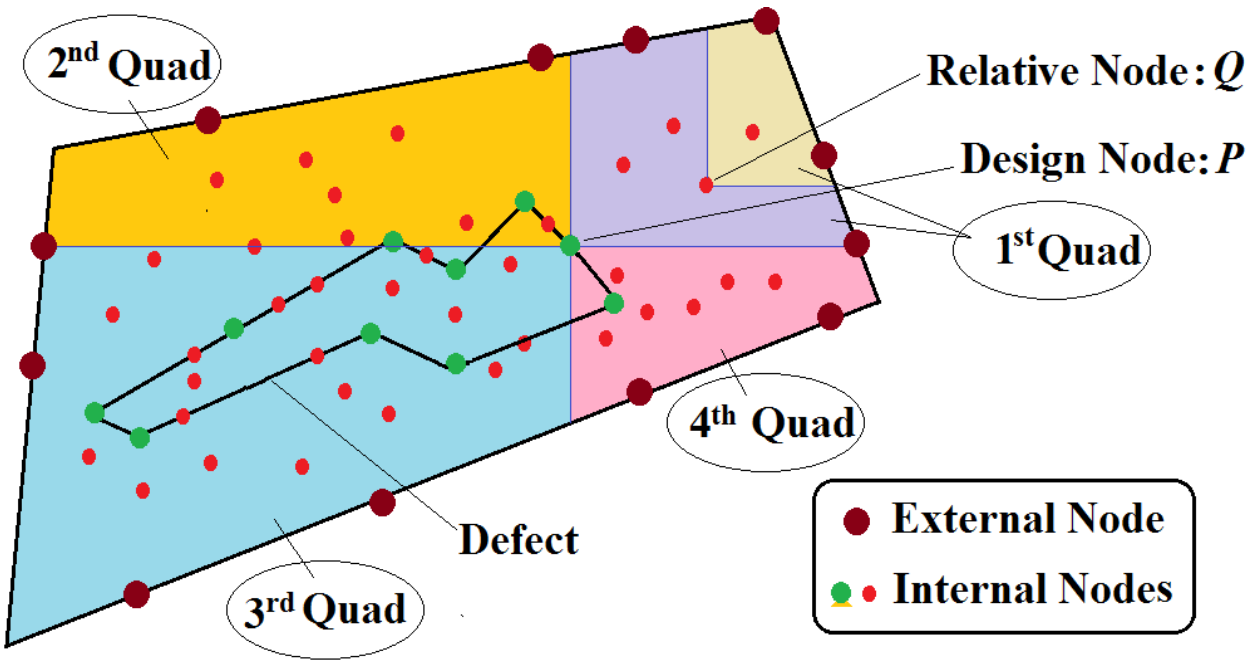

Figure 4-1 General plot representing only the defect region R_2 contains the defect.

We can see the difference between both interior and exterior nodes within this region in addition of dividing the interior nodes to both master (design) nodes and relative nodes.

The exterior nodes $A^{e}_{R_2}$ for R_2 will be fixed, not changed and will be the interfacing nodes with the reminder region R_1 through equation (3.19).

Each iteration of the inverse problem should be done within the preselected region R_2 only; this is the core of SFEM. Only the designing nodes (design parameters) as shown in Figure 4-1 will be changed in each iteration according the value of the given fitness score.

Here we will present the equations for linear movements, where we are going to save connectivity between nodes and as master node (our preselected design nodes) move, other nodes move elastically within a semi rectangular domain where it should start from 90^{o} angle at the moving design node forming parallelogram moving domain boundary surrounding the moving parameter which is the circumference of the defect region R_2. Where master nodes move toward this boundary, nodes between master nodes and R_2 outer boundary will move to crunch element's edge segments between these master nodes and the boundary. Where it moves away, edges are stretched. A single master node moving in a direction (x or y) commonly occurs. This is a special case of two-dimensional moving. In our solution, we consider movement in y-direction. This can be generalized to be in both directions.

Starting by drawing vertical and horizontal lines at the master design node P that divide the region R_2 into four quadrants as seen in Figure 4-1. If we consider the corresponding areas of these four regions are denoted by: $Area_{Qud1}$, $Area_{Qud2}$, $Area_{Qud3}$ and $Area_{Qud4}$. Now, in a certain quadrant, say the first one, if the node P moves a desired distance D in the y-direction (using Cartesian coordinates) all other nodes in the region R_2 are to be moved elastically with respect to the node P. Suppose Q, is a free node not tied to any parameter in the first quadrant and say, it moves by a distance d in the y-direction as P moves. To find the distance it moved related the moving of point P we will draw a vertical and horizontal lines at this relative node Q as we did for P. Now we can

find the area of $Area_{Q\_in\_Quad1}$ as the area of the region made by this relative node Q and the boundary of R_2 in the related quadrant (which is the first one in this case). Then, we can derive the ratio of moving an arbitrary node in the 1st quadrant relative to design master node P as:

$$C_i = \frac{Area_{Q\_in\_Quad1}}{Area_{Quad1}} \tag{4.1}$$

Where C_i defined as the moving ratio with respect to the free node Q_i and this is a key ratio in these elastic algorithms. We note that the area for each quadrant is never zero and this ratio is 1 when Q_i coincides with P. Similarly, a moving ratio can be found if the node Q_i is in the 2nd, 3rd, or 4th quadrant.

Therefore, each y-coordinate node within R_2 will be incremented as:

$$d=DC_{iy} \tag{4.2}$$

Where D can be negative depending on which side of P it is located. That is, the new y-coordinates of points P and Q^k_i will be: $P_{Ynew}=P_Y+D$ and $Q^k_{i,Ynew}=Q^k_{i,Y} + d$ for k=1,2,3 and 4.

Consider the following elements diagram in Figure 4-2. We marked the master node by a blue circle. According to the presented algorithm, we should first find the bigger area so that nodes will move only in this region. We will consider the outer boundary nodes for the bigger rectangular are the fixed nodes that will not move, while other nodes which are inside this rectangle will be free to move different distances and in different directions relative to the movement of the master node. To generate general scheme for moving n-master nodes, we will study moving one master node first and after that, we will generalize the related equations. We see from Figure 4-3 that we mark our master node by big blue circle. This problem may be considered as Magnetostatic problem or

rectangular problem or any other problem since we are still working on the preprocessing of the FEM problem.

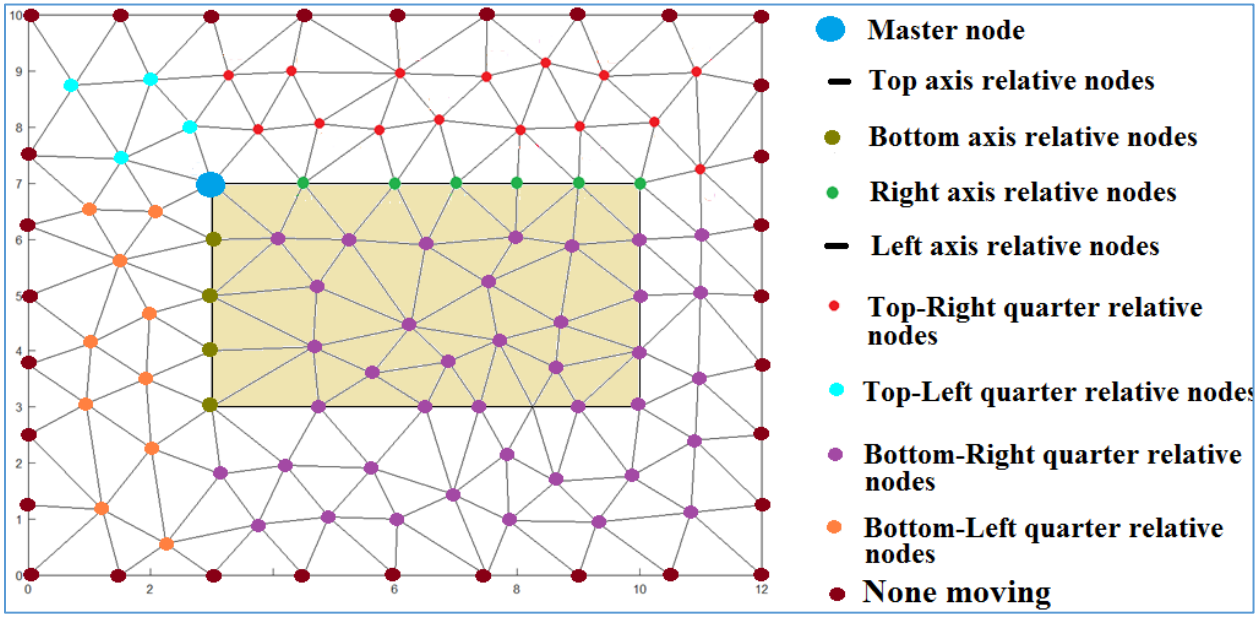

Figure 4-2 Position for: master, relative and none-moving nodes for one master node.

If we fallow the previous steps, then we can see that we will have fixed none-moving nodes. Also, we will have: bottom axis, right axis, top right quarter, top left quarter, bottom right quarter and bottom left quarter relative nodes. It is important to notice that we do not have any relative nodes on the top axis and left axis nodes for this example.

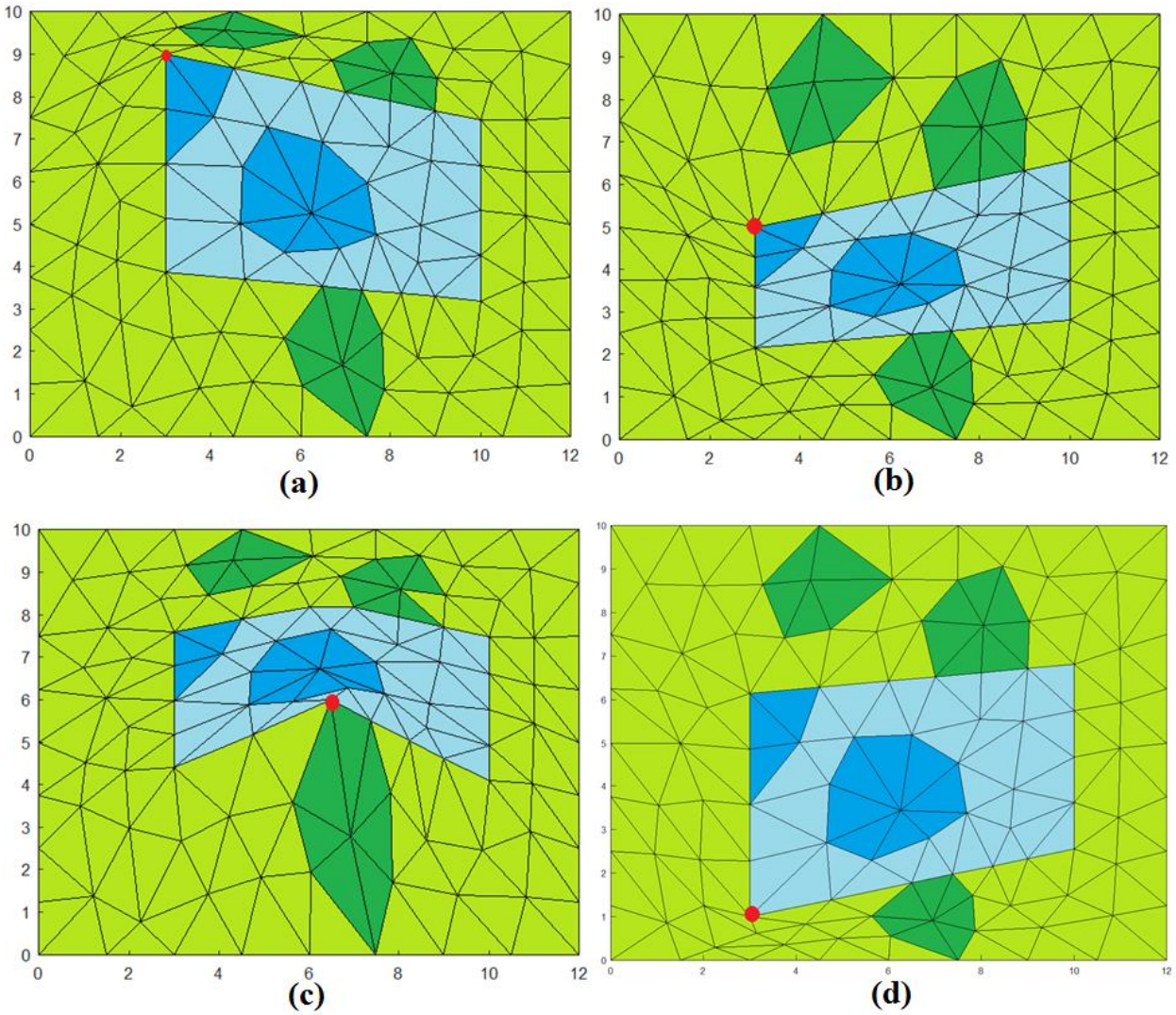

Figure 4-3 Example for moving one master node and the effect for stretching and crunching elements.

It is obvious that moving the master node in Figure 4-3a (the red circled node) will lead to moving other relative nodes, but it will keep and save the same connection between nodes which is the idea of this algorithm. If we move the master node vertically up wards, then we notice how elements become crunched upper the master node, while the lower elements will be stretched. While the opposite thing will be happening if we move the same master node vertically down as in Figure 4-3b. We can see other two different cases of moving master nodes and change the position of the master node in both Figures 4-3c and 4-3d. It is obvious now moving the master

node will crunch the elements that are in the same direction of movement while it will stretch the remanding ones.

4.3 Moving multiple nodes

The actual displacement for n design nodes $P_1, P_2, P_3, \ldots, P_n$ will be: $D_1, D_2, D_3, \ldots, D_n$. If P_1 moves a distance by h_1, then all other nodes, even master nodes will move by related distance. For example, if we have only two nodes P_1, P_2, then: P_1 moves by h_1, P_2 will also move as "another node" in the R_2 boundary by d_2. Similarly, P_1 will also move by d_1 as P_2 moves by h_2 as a master node. Thus, the actual movement of P_1 is h_1+d_1 and this combined total has to be D_1. Similarly, $D_2= h_2 + d_2$. Now let $C_{2,1}$ be the moving ratio of node P_2 with respect to node P_1. Here $C_{2,1}$ determines the movement of P_2 only due to the movement of P_1. Also, let $C_{1,2}$ be the moving ratio of node P_1 with respect to the node P_2. Hence, we can form a matrix, $[C]_{2x2}$, for moving ratios and find displacement, d_1 (due to the virtual displacement of P_2 using (4.2). By the same procedures, d_2 can be found. This can be formulated as follows:

$$\{D\} = [C]\{h\} \tag{4.3}$$

$$\begin{bmatrix} D_1 \\ D_2 \end{bmatrix} = \begin{bmatrix} 1 & C_{1,2} \\ C_{2,1} & 1 \end{bmatrix} \begin{bmatrix} h_1 \\ h_2 \end{bmatrix} \tag{4.4}$$

Equation (4.4) is solved for h_1 and h_2 by inversion and we move the nodes P_1 and P_2, accordingly. The total movement will be as required. To generalize this method for solving n design nodes, we will define $\boldsymbol{v}_{nx1}$ as the vector of actual displacements of all n variable design nodes (including the nodes on the line joining design nodes). Now let $[C]_{n\times m}$ be the matrix of all moving ratios of the m nodes in the moving domain with respect to the n design nodes. All these moving ratios can be easily computed. Taking h_n as the vector of virtual displacements of all n design nodes (including

nodes on the line joining design nodes). The *y*- displacement of each node in the moving domain R_2 can be computed from:

$$y_{new}^{i} = y_{old}^{i} + \sum_{j=1}^{n} c_{i,j} h_j \quad , \quad i \in R_2 \tag{4.5}$$

Other important factor should be taken into consideration which is how other relative nodes on the circumstance of the defect and between the design nodes move because of moving these design nodes. The movement for these nodes can be interpolated refereeing the surrounded design nodes. Therefore, we can guarantee these relative nodes will stay on the same line after moving the design nodes. The following example in Figure 4-4 shows how defect shape can be changed each iteration using elastic SFEM. First, the selected defect region should be selected. Next, a selected predetermined design values should be chosen on the surface of the defect. Those nodes will have the same connectivity and numbing scheme same as all nodes and elements within the selected defect area each iteration. Those nodes will be the design nodes: P_1, P_2, P_3, …, P_n

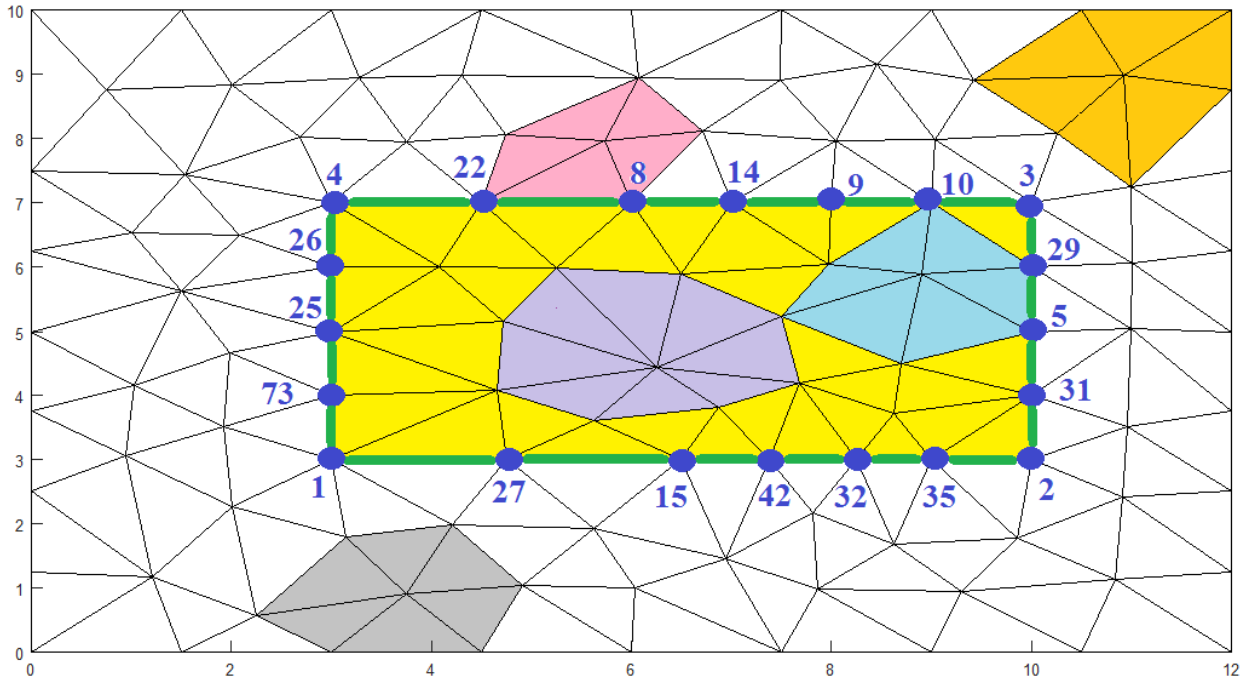

Figure 4-4 System for multiple master nodes surrounds area of interest

The effect of moving multiple design nodes and their effect on the entire system of moving are shown in Figure 4-5. The area of interest is selected as the inner rectangle that maps the defect region. The number of design nodes can be chosen regarding the computational cost with knowing that the maximum number of design nodes we have. In this example, the defect is surrounded by design nodes, where these nodes numbers are: (4, 22 , 8, 14, 9 ,10 ,3 ,1 ,27 ,15 ,42 ,32 ,35 ,2 ,73 , 25, 26, 31, 5, 29).

Moving these nodes will certainly affect the entire elements by different of stretching and crunching ratios and values according to the direction and value for each single movement per each design node as shown in Figure 4-5.

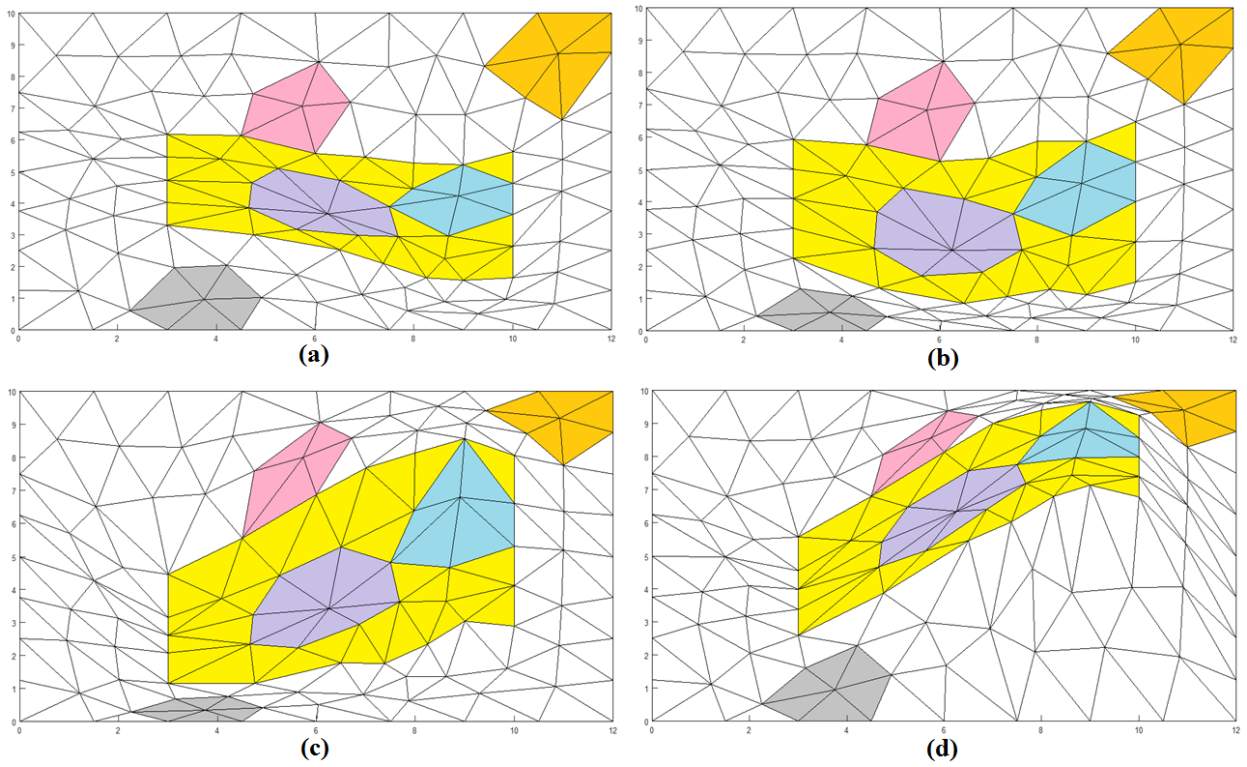

Figure 4-5 Moving multiple of master nodes and their effect on related elements

As shown in Figure 4-5, we can get unlimited patterns for the internal region after each iteration of movement for the design nodes. This will show how defect can change its shape each iteration

until getting the best fitness score function. It is important to mention that each defect pattern in Figure 4-5 has the same design nodes as in Figure 4-4 in addition of the same elements and nodes numbering and connectivity matrix. This technique will be the key for solving inverse problems for characterizing and reshaping structures given certain constraints, as we will see in the next chapter.

5 Computational Validation for Subregion Finite Element Method

This chapter will present several numerical examples that can be solved using SFEM. The presented algorithm is validated by comparing SFEM results with COMSOL, classical FEM and results found in other papers. A computational validation will be presented in this chapter while an experimental validation will be presented in next chapter. Magnetostatic examples will be presented first , since SFEM was derived from solving such problems as in [85]. After that, several examples and cases for ECT problems will be solved in both direct and inverse methods.

5.1 Magnetostatic Problem

Multiple examples will be shown in this chapter to verify the presented algorithm. Simple cases in Magnetostatic cable problems will be shown first to explain how solution domain can be divided into multiple regions. Those examples will be solved gradually until reaching complete design Quasi- Static problem that is characterizing hidden defect in inverse ECT problems using the SFEM.

Example 5.1, Basic Cable problems with few elements.

In this example, a rectangular conductor carries a current density of (J=3A/m^2) is surrounded by air. We need to find the magnetic vector potential values and to draw the field lines for this cable example in Figure 5-1. The relative permeability for all regions is 1.

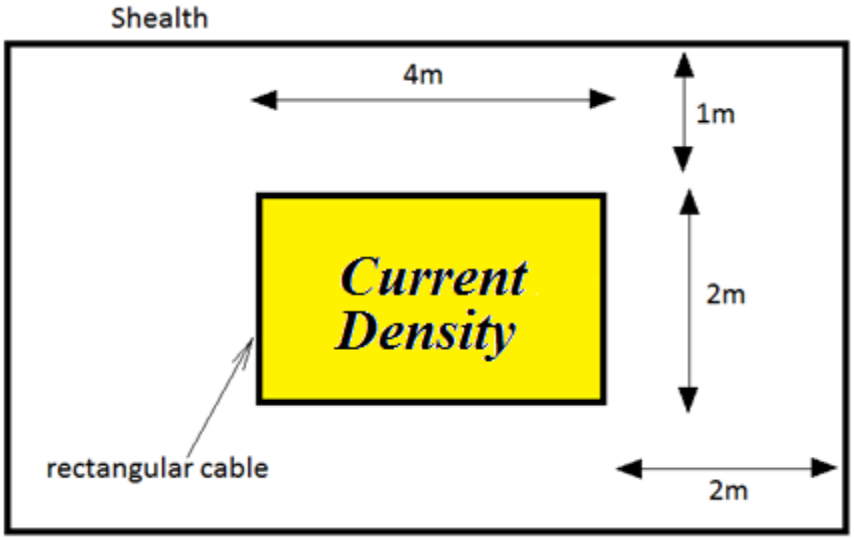

Figure 5-1 Cable System of rectangular conductor carries current density of (J=3A/m^2) surrounded by air

After applying FEM technique as in [95, 118], Magnetic vector potential field lines can be drawn, (choosing 45 nodes, 64 elements) as in Figure 5-2. The fields plot is true according to solving Maxwell's equation.

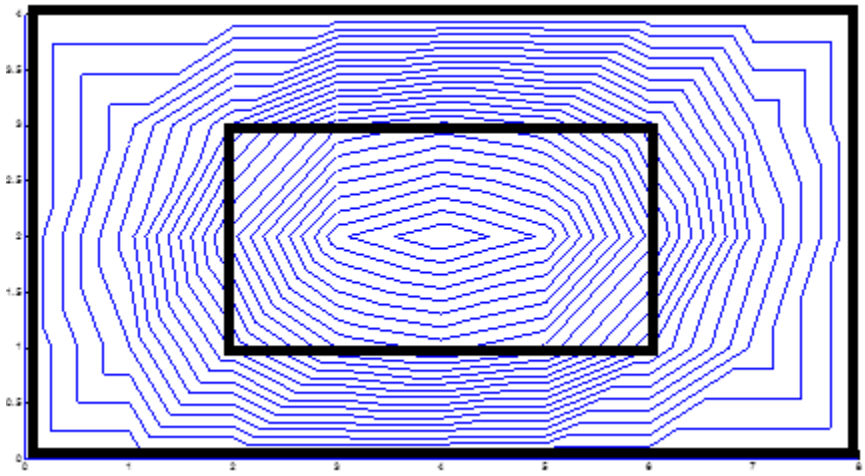

Figure 5-2 Potential lines distribution for the cable example for limited number of elements

The aim for this thesis is to do subdomain analysis, one subdomain example is to divide the problem area as in Figure 5-3. While we can also divide our problem area into multiple forms according to the given parameters and conditions.

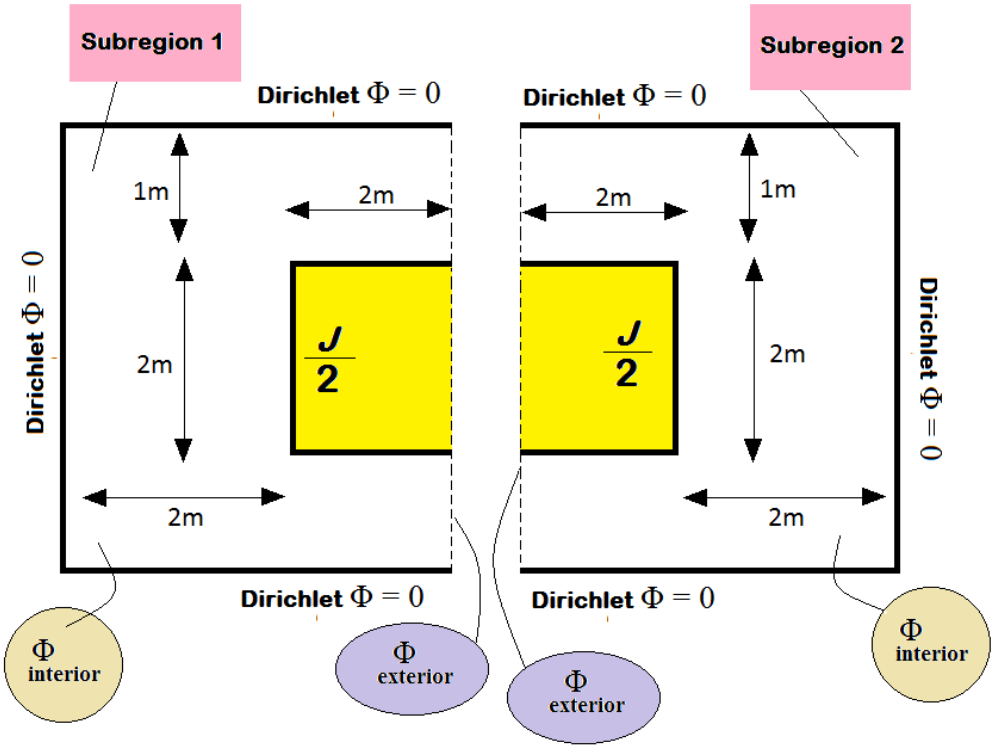

Figure 5-3 Subdivision of the whole solution domain

According to Figure 5-3, the solution domain in Figure 5-1 can be divided into two subregions (1 and 2) as in Figure 5-3. Dividing the solution domain to two or more solutions will be the first step in SFEM and will minimize processing time as was shown in Chapter 3.

Example 5.2, Cable problems with higher number of elements.

In this example, subregion method will be used to find magnetic vector potential lines in addition of increasing number of elements and nodes. We will solve this example in detail so it will explain the procedure that we used in the presented analysis. We increased the number of elements to 1012 elements that distributed into 550 nodes. We will divide our problem into internal and external subregions. The internal subregion will be the rectangular conductor which carries a current density of (J=3A/m^2). The external subregion will be the surrounded free space. The relative permeability for both two regions is 1.

According to subregion method, we should define the subregions in addition of both internal and external nodes. As a preprocessing step, we have used the mesh generation which was presented in [117] to generate meshes for both regions. Therefore, we can now summarize the solution steps into the following steps:

1- Define and name the solution subregions that we will use in our analysis. As seen in Figure 5-4:

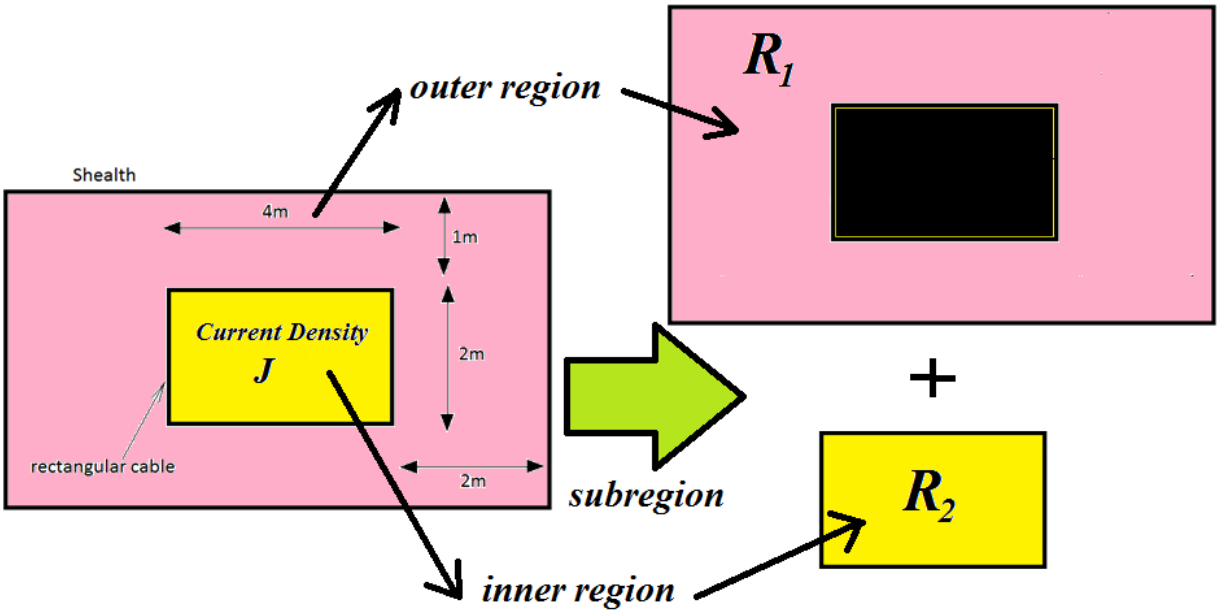

Figure 5-4 Define both regions air (R_1) and conductive cable (R_2)

2- Therefore, we have now both of R_1 and R_2 as the outer and inner subregions respectively. Now we must mesh each subregion individually, but we must keep the numbering scheme as like we did it for the complete problem, so that we can get our solutions from all subregions. We have a total of 1012 elements for the complete problem. For R_1 , we used 758 elements as in Figure 5-5.

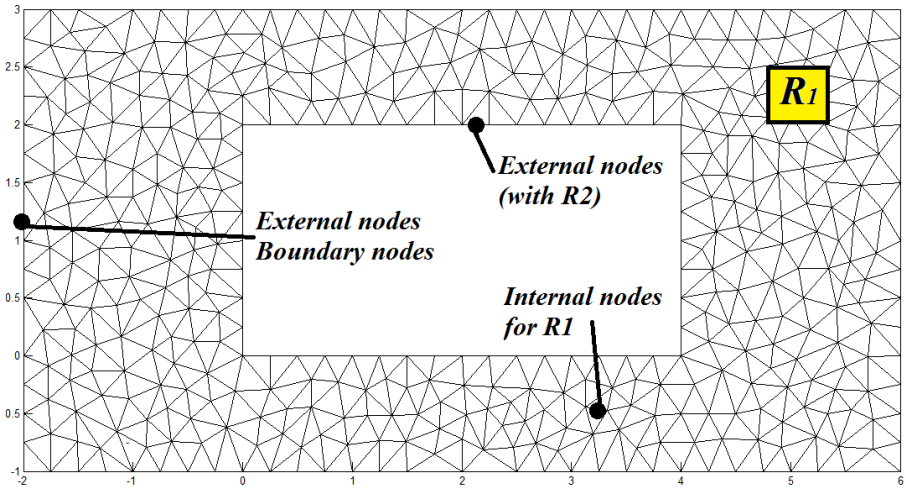

Figure 5-5 Region 1 elements distribution

The total number of nodes for R_1 will be equal to number of external nodes added to number of internal nodes and this will be equal to the number of edge nodes with other regions (R_2) in this example in addition to number of boundary nodes added to number of internal nodes within R_1, which will be the summation of (48, 86 and 312). The result will be 446 nodes while we have 758 elements for R_1.

3- Now we will repeat step (2) for R_2. The preprocessing FEM analysis for R_1 will generate elements for R_1 as in Figure 5-6 as:

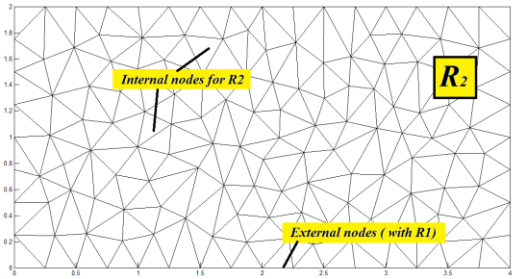

Figure 5-6 Region 2 elements distribution

Now we have to compute the number of nodes for R_2 as we did for R_1, the total number of nodes for R_2 will be the number of external nodes for R_2 added to number of internal nodes for R_2 which

is equal to number of edge nodes with R_1 since we do not have boundary nodes in R_2 added to number of internal nodes for R_2 as 152 nodes, while we have 254 elements for this region.

4- Now, we used the subdomain equations to find the values of magnetic vector potentials at the external nodes and then use these values to find the values for the internal magnetic vector potentials for both R_1 and R_2. After that, we can plot the vector potential fields for both regions as:

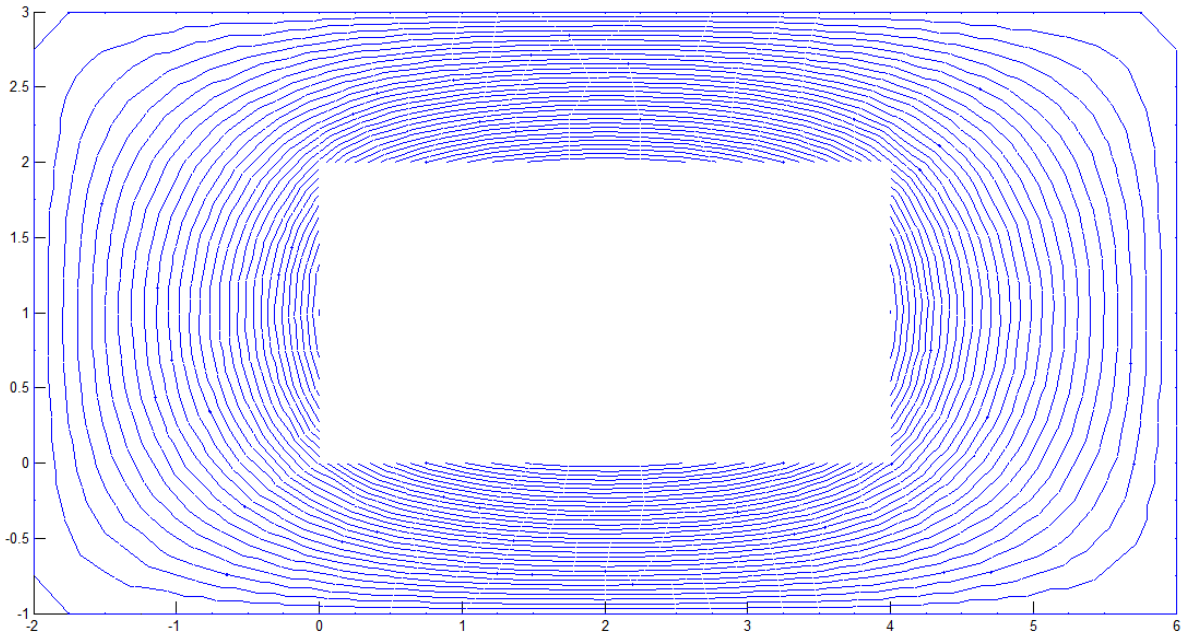

Figure 5-7 Vector potential plots for R_1

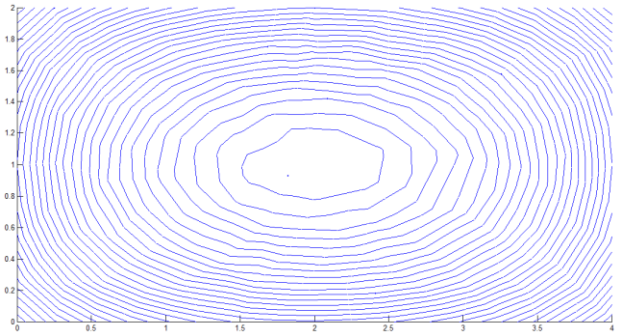

Figure 5-8 Vector potential plots for R_2

The results in Figures 4-7 and Figures 4-8 show an exact matching between the plots of vector potential lines for both cases (classical FEM solution) and SFEM solution for the same problem and both solutions are true.

5.2 Forward Eddy Current Problem

In this section, several examples are presented to verify using SFEMSFEM in solving ECT problems. The main objective for the presented method is to simplify solution for big size and complicated problems by choosing small subregion represents defect location and change its parameters without the need to implement FEM method again for the total problem in each iteration.

In this part, 2D model for coil carrying AC current inducing magnectic flux density to generate an eddy currrent will be used to detect hidden metalic defects. This study is done for different defect parameters including shapes, angles and depths of the cracks. Meshing diagram then equipotential lines will be plotted with different defect structures. In addition, magnetic flux density will be calculated at certain measuring points. Finally, some analysis will be done based on the final values. Defect shape, size and position will affect the resultant magnetic density values at the measuring points. To model that, the magnetic flux density will be treated as function of the following defect parameters: $\{x, d, l, w, \theta\}$ as shown in Figure 5-9.

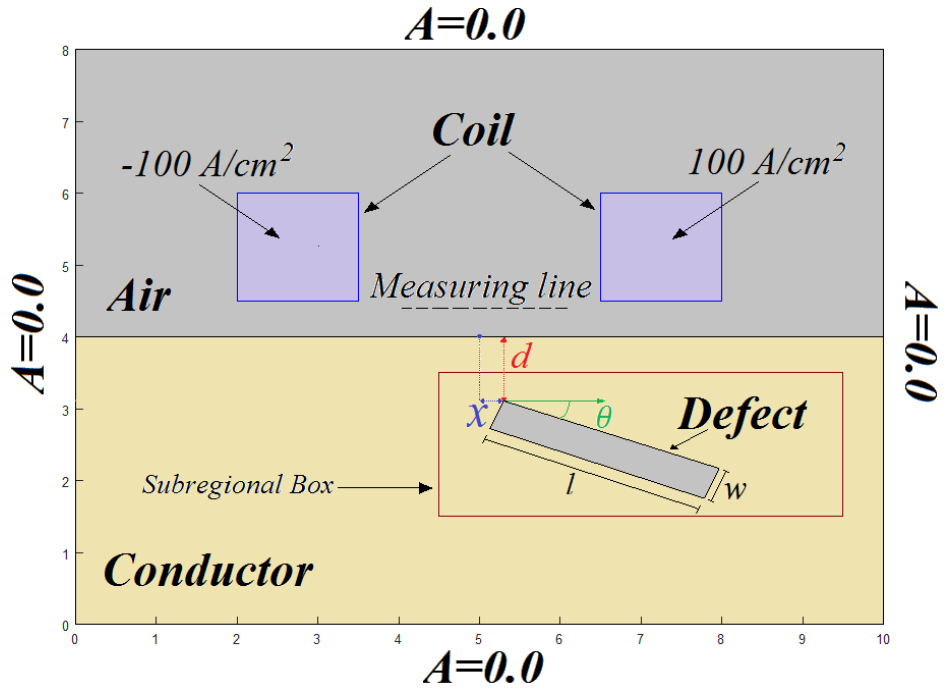

Figure 5-9 The 2D model for the given problem with a given numerical values showing the box that separates total area to both regions one and two.The region inside the box will be R_2 while the reminder region is R_1

Where, x: is the horizontal distance between the defect and the center of the domain which gives an indication about the horizontal defect position with respect to coils, d: is the depth of the defect in the material far from the material surface; which gives an indication about the vertical position of the defect and how it can be detected comparing to skin depth value. While l and w are both defect length and width respectively. Finally, θ is the clock-wise rotation angle of the defect from the horizontal line parallel to the material surface. The box which surrounds the defect will separate the entire domain of soliton into two subregions; subregion two (R_2) which is the area inside the box and subregion one, (R_1) which describes the reminder area of the problem. It is clear that the box that is chosen is general and suitable for all cases; which means it may cover part of the conductor and the air according to the position of the defect and its closeness to the steel surface.

To summarize the methodology that used in solving ECT problems using direct SFEM such in Figure 5-9, a flow chart is used as in Figure 5-10 to explain solution process step by step starting

from giving values of the physical properties and ending by getting the results. The core issue of the solution is how defect region is selected and separated from the entire region as was done in Figure 4-1. The parameters for bigger domain which represents the reminder region R_1 will be saved for the entire of the structure. To update the defect itself like changing its physical parameters through the presented algorithm, FEM will not be used each time once defect's properties are changed through the entire solution. It is enough to separate the defect from the problem and call it as region two and change these parameters including width or length or orientation while keeping the FEM data for region one fixed each iteration. This will lead to get values of the magnetic flux densities at the pre-determined measuring points. All what needed is to update the defect region related profile (R_2).

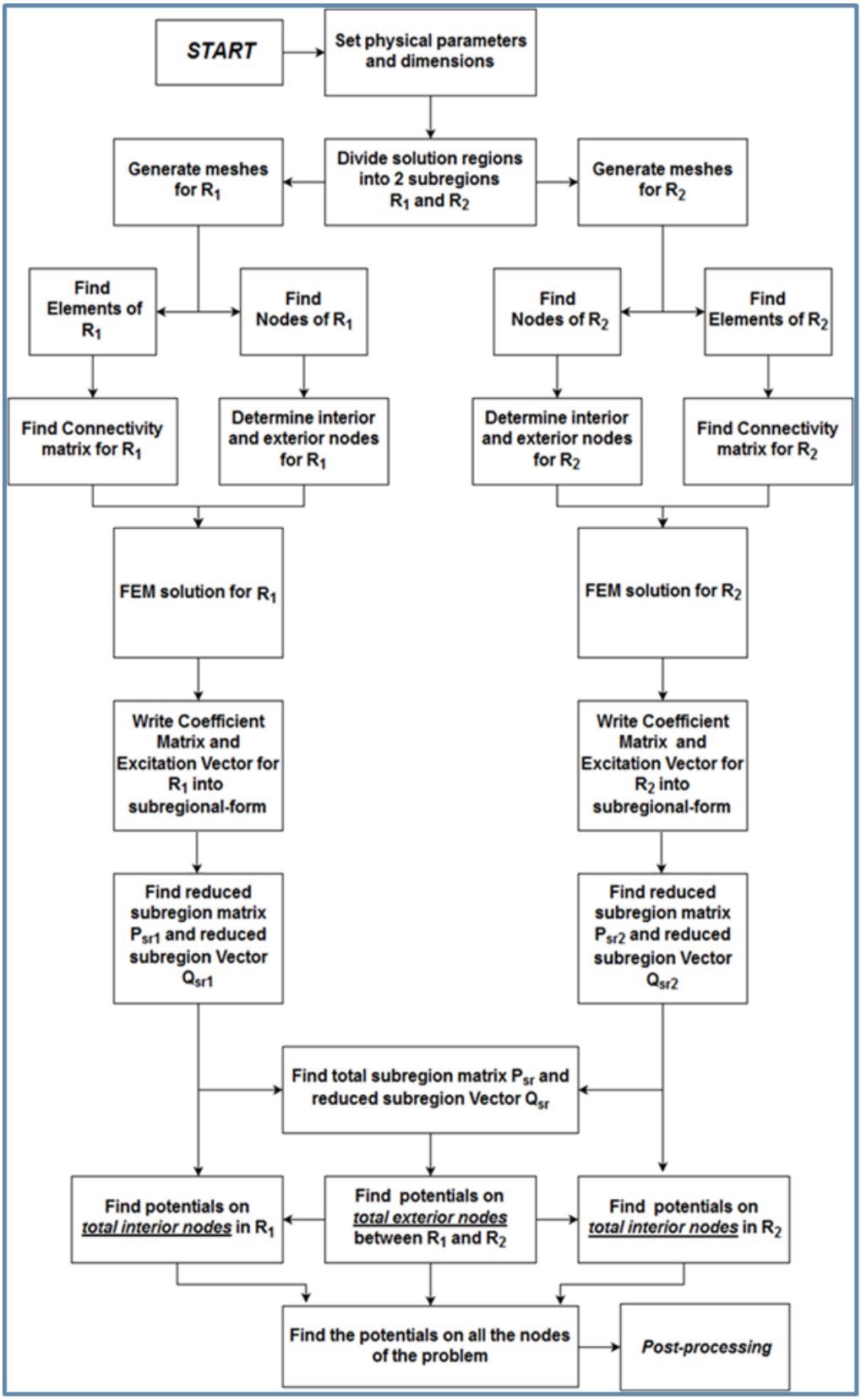

Figure 5-10 Flow chart for solving direct ECT problems using SFEMSFEM

From programming point of view, a mesh generator should be used to generate meshes for different predetermined subregions. An automatic parameter-based mesh generator that used for several inverse Magnetostatic problems [117] was used to generate elements and nodes for each region. The important point, even these nodes and elements are generated for two separated subregions, then the related data for both nodes and elements numbering scheme will be saved for both regions; for example, if region one contains two elements and region two contains three elements, then, total number of elements will be five but with two elements in region one like element two and element five and the reminder elements will be for region two which are elements one, three and four. After finding the related nodes and elements for both subregions, FEM now can be used for both subregions. The basic step is to update FEM solution by rearranging nodes to both interior and exterior nodes for both subregions to use them later to get the solution. Choleski Decomposition is used twice in this algorithm; the first time when both subregion matrix $[P_{sr}]$ and subregion vector $\{Q_{sr}\}$ were found as seen from equations (3.12) and (3.15). The second time when final FEM solution is used to find potential values at all external nodes in (3.19). Where the resulted values at these external nodes will lead to find the reminder values of potentials in the interior region for both subregions (3.6).

The algorithm that is shown in Figure 5-10 will be applied for different defect cases and parameters for the model that was introduced in Figure 5-9. This example will be presented to validate the proposed technique in solving some of ECT problems. The following examples in this section will show how we can use SFEM in solving direct ECT problems.

Example 5.3, Evaluating Equipotential Lines for Different Defect Shapes

In this example, subregion method is used in deriving and plotting magnetic potential lines. As for classical FEM method, meshing both R_1 and R_2 will be the first step after considering the defect area as a separated region from the entire region. After that, our FEM solver will be used to get the values of potentials in both interior and exterior nodes for both subregions. Next, these potentials will be used to find the values of the potentials for the reminder nodes. Finally, a post processing algorithm can be used for plotting the magnetic fields for the total domain. The defect in this example will have the following fixed parameters based on Figure 5-9 $\{x = 0.0, d = 0.5\text{cm}, l = 2.5\text{cm}, w = 0.1\text{cm}\}$ and different angles of defects rotation of: 90^o, 0^o, 30^o and a no defect case. The following steps must be followed to get the final solution

1. Generating meshes after determining both subregions.

The first part in solving subregion problems is to determine these subregions. A fixed model dimensions of 8 cm by 10 cm will be divided equally to upper and lower air and conductive halves respectively. The AC current will flow in the coils with a current density of ± 100A/cm^2 (the negative sign refers to the opposite direction of the current through the coil). This current will induce the coil magnetic flux density that will induce the eddy current at the surface of the conductor. This conducer's conductivity is 1000S.m^{-1}. Four cases will be analyzed in this part based on Figure 5-11 depending on the defect characterizations. All the cases will share the physical properties and dimensions of {x=0.0,d=0.5cm,l=2.5cm,w=0.1cm}, while no defect case will be taken in our study in addition to three different defect angles of (0^o, 30^o and 90^o). The meshing diagram for each case for both regions is shown in Figure 5-11.

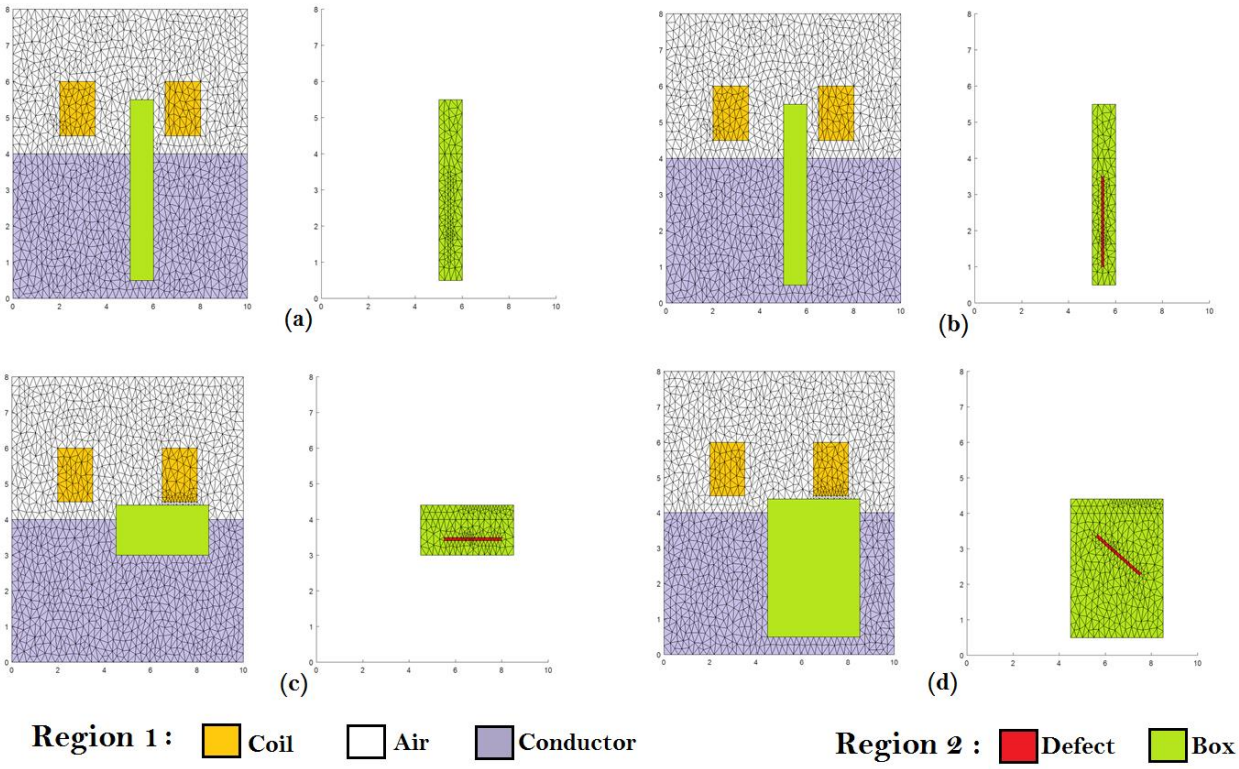

Figure 5-11 Meshing diagram for both regions (1 and 2) as tabulated in Table 5-1 effected by a defect with the following parameters: $\{x = 0.0, d = 0.5cm, l = 2.5cm, w = 0.1cm\}$ and different angles of rotations. (a) No defect Case. (b) 90^o Defect angle. (c) 0^o Defect angle. (d) 30^o Defect angle.

Taking the defect as a separate region regardless of the reminder of the domain will simplify the solution for advanced applications. Dirichlet boundary conditions of zero potential is applied to all boundaries for the total problem since no symmetry was used. It can be seen that Region 1 contains the meshing of the coils, part of the air and part of the conductor, while Region 2 contains the remainder part of the air and the conductor in addition to the defect itself. According to [117], the minimum elements area will be 0.05cm^2. These relatively small elements were automatically used in critical and narrow spaces. Table 5-1 shows meshing data used in generating both regions for all cases in Figure 5-11.

Table 5-1 Meshing data including number of nodes and elements for both regions (one and two) for the current example and processing time for all cases.

	No Defect		90^o Defect angle		0^o Defect angle		30^o Defect angle	
	R_1	R_2	R_1	R_2	R_1	R_2	R_1	R_2
Number of Nodes	1275	154	1275	154	1292	191	1157	347
Number of Elements	2380	260	2380	260	2409	329	2118	623
Processing Time (s)	39.69		44.69		59.09		56.53	

Increasing the number of elements will increase processing time. In the 30^o defect angle case, more elements are used for meshing the two regions, since angular defect will occupy more rotational area within the metal, so, processing time (getting the final potential values) at all nodes will take the longest time.

2. Plotting potentials for both subregions.

After generating the meshes for both subregions, FEM analysis will be applied for both subregions (1 and 2) according to the flow chart in Figure 5-10. There will be three separate sets of nodes: I- The outer boundary nodes where all Dirichlet potential values at these boundary nodes equal to zero, so these values are known in our solution. II- External nodes between the two-separated subregions where, the potential values on these nodes are found using equation (3.19). Now the outer boundary nodes are also external nodes to the related region which is Region one in this case, but since they have a given predetermined values, then, those can be considered as a separate set of nodes. III- The internal nodes for each subregion, which are all found after knowing the values of the potentials on all external and boundary nodes, and equation (3.6) is used to find the potential at these nodes. After having the values for the total potentials at all nodes, vector potential can be

plotted in a 2D-xy plane for both regions. Figure 5-12 shows the complete plot for the potential values for the same previous example that used in Figure 5-11.

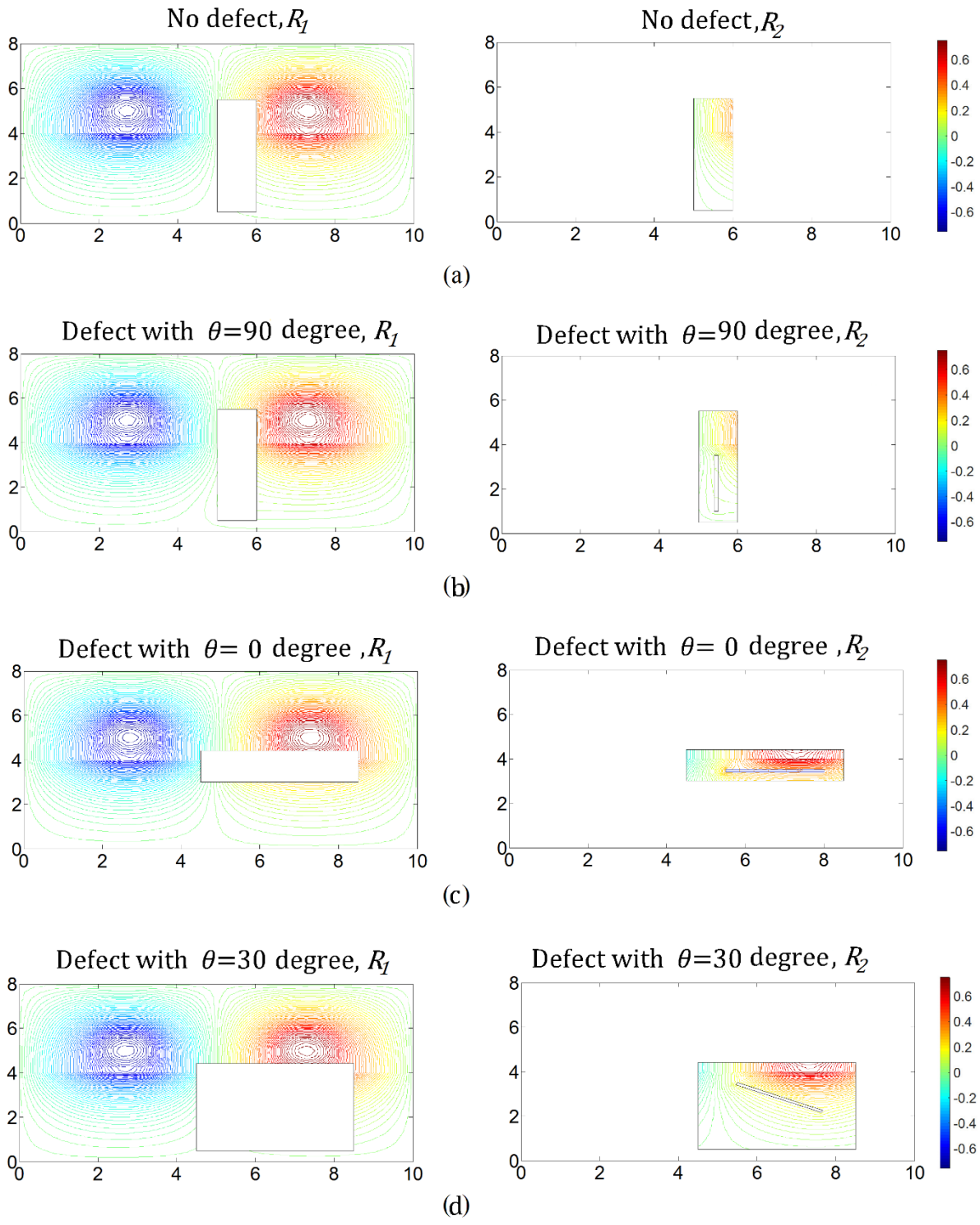

Figure 5-12 Equipotential lines for both regions (one and two) for example in Figure 5-11. (a) No defect case. (b) 90° Defect angle. (c) 0° Defect angle. (d) 30° Defect angle

It is clear that each case represents a defect angle that has two vector potential plots for both defect and reminder regions. Where each case represents different defect angle. In Figure 5-12a, a no

defect case was introduced, so a non-interrupted potential can be noted as expected. While, in Figure 5-12b and Figure 5-12c a 90^o and 0^o defects angles affected potential lines respectively, and an interrupted potential fields due to these defects were resulted. In Figure 5-12d, a 30^o defect angle was studied, where some interrupted potential fields were resulted due to the defect presence. The results in Figure 5-12 shew how fields distributed in both regions R_1 and R_2 in each case and how equation (3.19) was used to connect both regions solutions to the final one. More details about the field lines and final values can be more obvious when recombining fields in both regions after using same coordinates for the original domain as in Figure 5-13.

3. Plotting field lines for the complete problem.

Figure 5-13 shows the complete plot for the field lines for each case of the defect angles. Merging both regions to return to the original domain will connect the separated field lines.

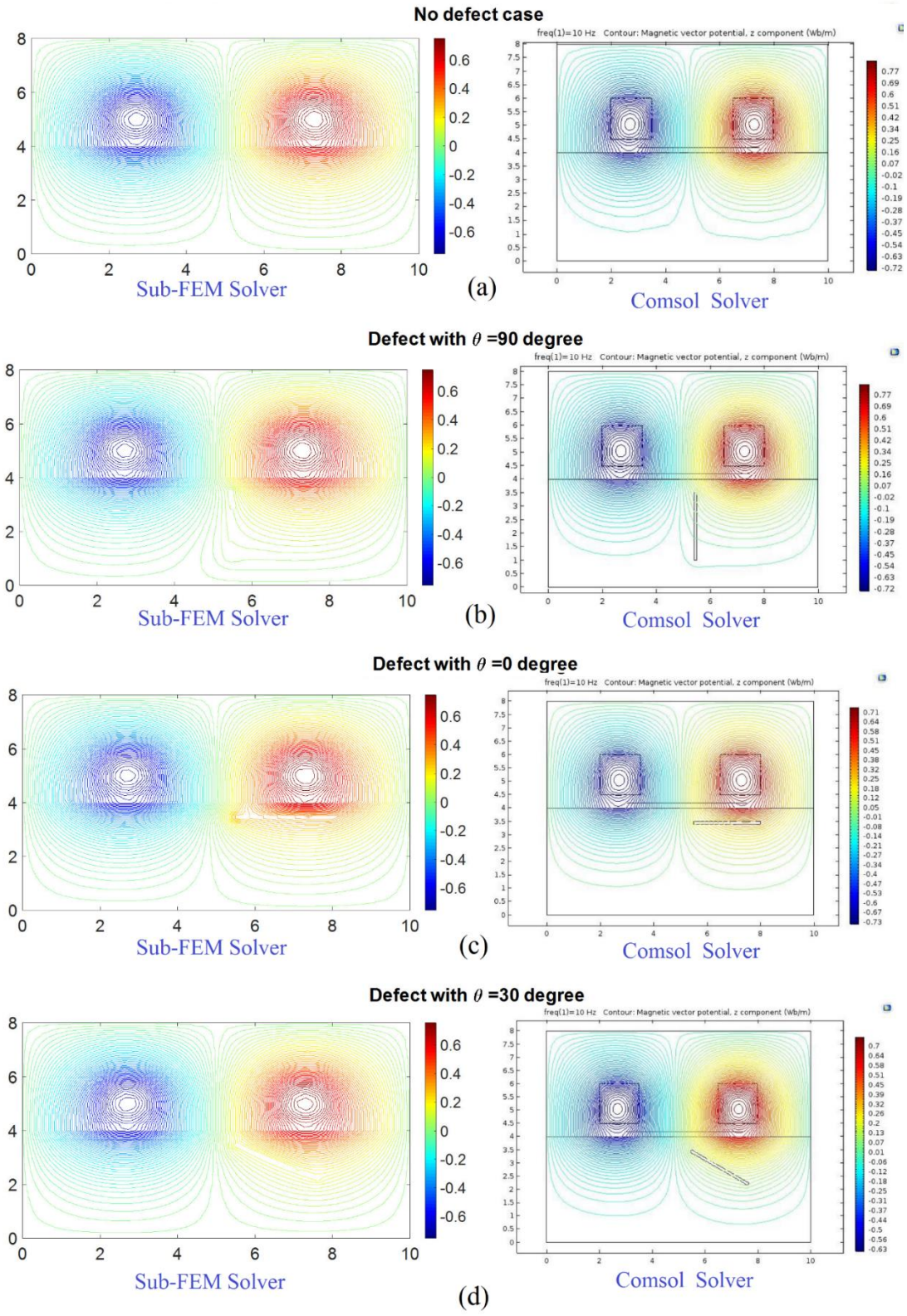

Figure 5-13 Final plot for the magnetic equipotential lines for example in Figure 5-11. (a) No defect Case. (b) 90^{o} Defect angle. (c) 0^{o} Defect angle. (d) 30^{o} Defect angle.

COMSOL was used to validate results achieved by SFEMSFEM solver. An excellent matching between both SFEMSFEM solver and COMSOL solver is clear from plotting the potential lines per each case in Figure 5-13. It is now clear that there will be no interrupted of fields when defect free problem exists as shown in Figure 5- 13a and dividing the problem will help us in saving time if our solution is repeated for different physical properties for the elements who are saved in R_2. Changing the defect angle will lead to make changes in the fields and will resulted in interrupt some fields. The values of magnetic vector potentials, then, the plot for these potential lines in defect region can give a mark of having defect as noticed from the total plot for the complete domain in Figure 5-13 for the four presented cases. Detailed study of changing the properties of the defect will be presented in the next examples.

Example 5.4, Comparison Between Classical and SFEM

A classical FEM solver was used to solve same exact examples in addition to COMSOL validation by meshing total domain area R instead of defect region R_1 and reminder region R_2 in equation (3.2) to triangular elements where a first order two dimensional trail function $\tilde{a}(\xi_1,\xi_2,\xi_3)$ was used to represent any point inside these elements as:

$$L\{\tilde{a}(\xi_1,\xi_2,\xi_3)\}=\sum_{\forall\Delta}\left(\iint_{\Delta}\left(\begin{array}{l}\frac{1}{2\mu}\left(\nabla\tilde{a}(\xi_1,\xi_2,\xi_3)\right)^2-\tilde{J}_0\tilde{a}(\xi_1,\xi_2,\xi_3)\\+\frac{1}{2}\,j\omega\sigma_e\tilde{a}(\xi_1,\xi_2,\xi_3)^2\end{array}\right)dR\right) \qquad (5.1)$$

Where, (ξ_1,ξ_2,ξ_3) are the triangular coordinates for any point (x,y) inside each element. A comparison between presented SFEMSFEM and classical FEM results for 90° defect rotation angle at some measuring points is presented in Figure 5-14. These points are:

[(3,4.2), (3.5,4.2), (4,4.2), (4.5,4.2), (5,4.2), (5.5,4.2), (6,4.2), (6.5,4.2), (7,4.2), (7.5,4.2),] (cm).

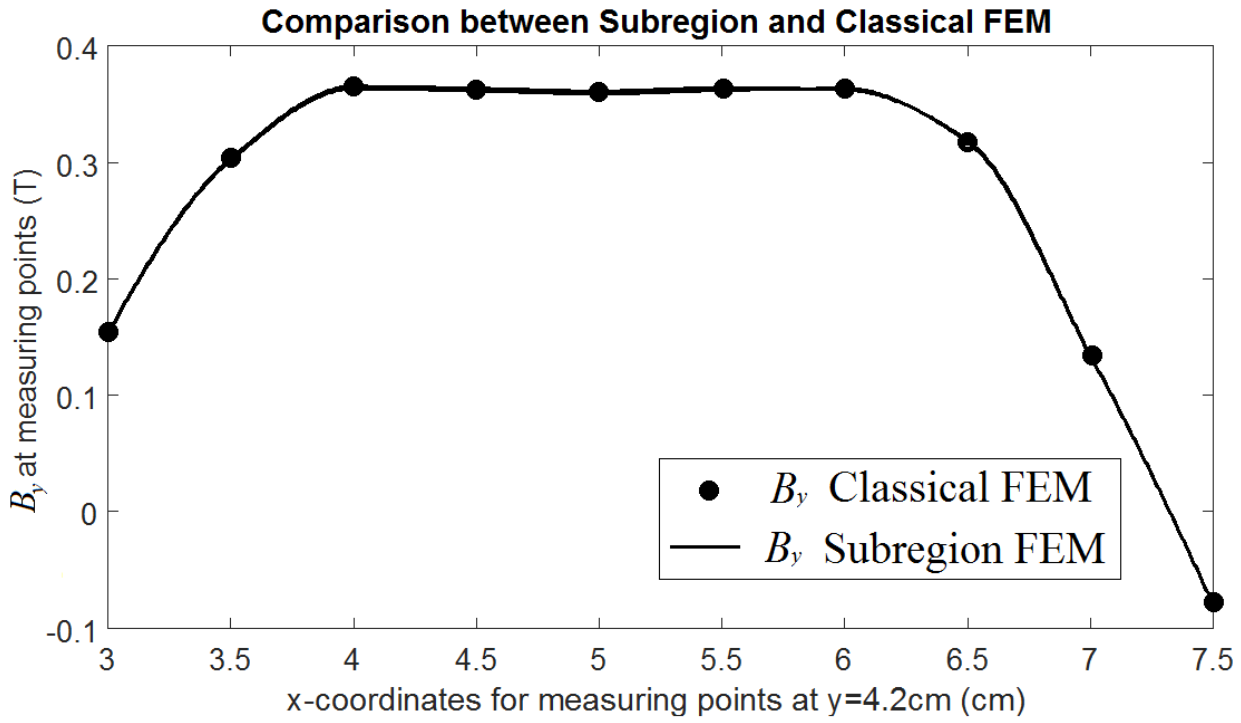

Figure 5-14 Magnetic Flux Density in the y-direction for the 90^o defect problem at some measuring points

Figure 5-14 shows an excellent agreement between the values of the perpendicular magnetic flux densities B_y at the these points found using the SFEMSFEM and those which were found through the classical FEM method as in [115] and through solving equation (5.1). The final results through classical FEM method for any problem should map those found through subregion method. They are both FEM but with different meshing and dividing schemes.

The main purpose of using the subregion method is to save computations and processing time especially for large problems. Dividing the original problems into separated profiles, then saving the data for each profile and use these profiles later in the SFEMSFEM method is an effective way for dealing with these large problems.

Example 5.5, Maximum Value of Magnetic Flux Density Ratio

It is important to study the relation of changing some of the physical parameters of the defect to setup a robust algorithm to detect these hidden defects. In this example, multiple parameters will be analyzed using SFEMSFEM. The effect of changing some of the numerical parameters that are related to the defects dimensions and positions while keeping the reminder parameters fixed as shown in Figure 5-9. Next, SFEMSFEM will be applied once, twice or more according to the nature of the problem and how many times these parameters changed. After that, magnetic vector potentials will be found and it was noticed that interruption to these lines happened due these defects and this will give a flag whether if there is a hidden defect or not. However, in more advanced problems, like optimization and inverse problems, this will be not enough, since measuring vector potential lines inside the conductor region will be difficult. So, some measuring points will be appointed at the surface of the conductor to measure the resultant magnetic flux density that results from both the eddy current and the AC current in the coil. In this example, pre-determined 10 points will be located for the model in Figure 5-9 with keeping the values for conductivity and current density fixed. These points are:

[(3,4.2), (3.5,4.2), (4,4.2), (4.5,4.2), (5,4.2), (5.5,4.2), (6,4.2), (6.5,4.2), (7,4.2), (7.5,4.2),] (cm). Finding the values for magnetic flux density at all these points will be the next step in our solution.

By changing defect parameters like: length, rotation angle, width or depth, these values for magnetic flux densities will be changed at the these measuring points as these values will be changed for the entire domain. The values for resultant B_y due the existence of the defect at these measuring points will be named as B^i_{defect}. Then the effect on flux density R^i_B will be calculated for each defect and tabulated as the normalized difference between $B^i_{nodefect}$ and B^i_{defect}. By considering the maximum of R^i_B, the defect detecting ratio will be defined as [115]:

$$R(\theta,d,l) = max\left(100 \times \frac{B^i_{nodefect} - B^i_{defect}}{B^i_{nodefect}}\right) \tag{5.2}$$

where, $R(\theta,d,l)$ is the maximum value of flux density ratio between flux changes caused by the defect and flux without the defect, where a defect with length l is at depth d from the material surface and rotated by angle θ clock-wise from the horizontal line parallel to the steel surface as seen in Figure 5-9. Figure 5-15 shows multiple examples of different defects sizes and positions parametric studies. This will give an excellent handout for detecting these kinds of defects once they are existing.

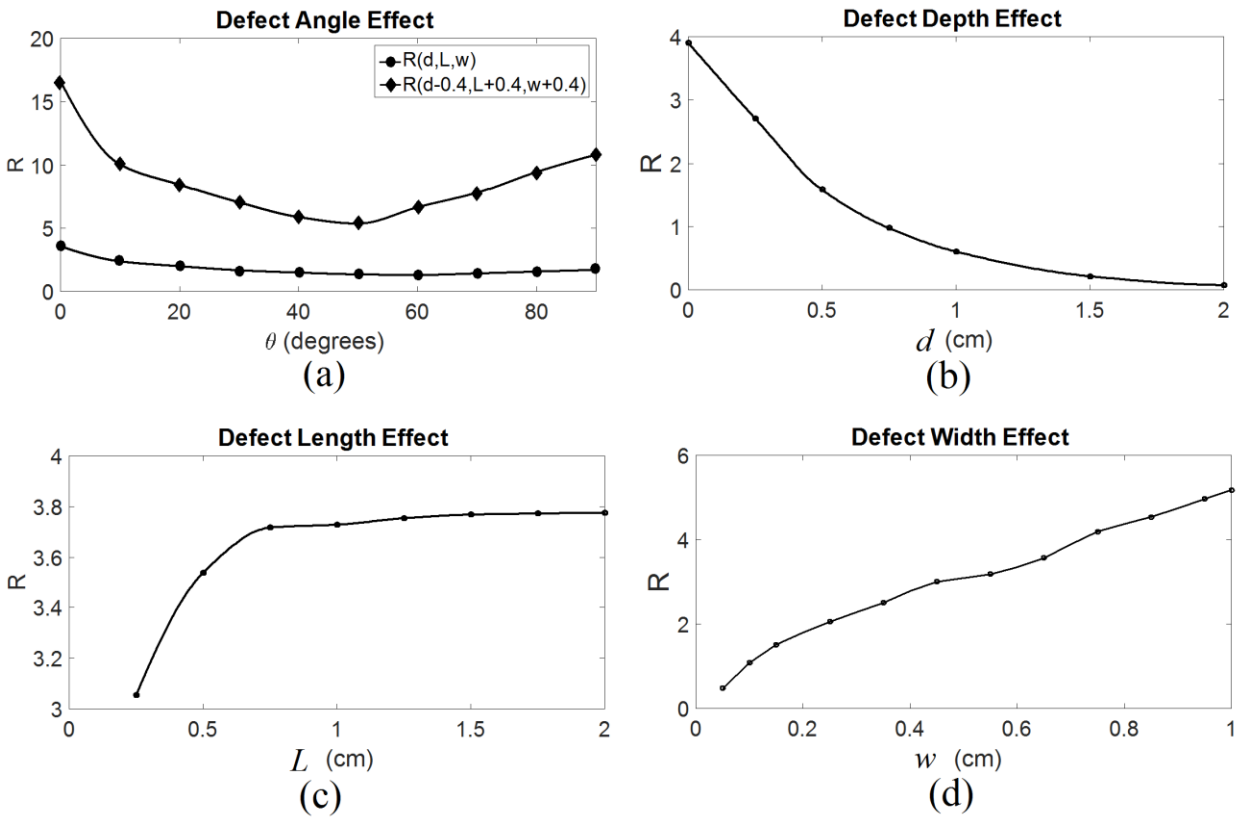

Figure 5-15 The relation between $R_{(\theta,d,l)}$ and the variance of some properties: (a) with the defect angles. (b) With the defect depth from steel surface. (c) With the defect horizontal displacement from the right edge. (d) With the defect width.

Figure 5-15 shows how ratio $R(\theta,d,l)$ varies with defect parameters. When $R(\theta,d,l)$ is high, there will be a higher chance that the defect will be detected. Figure 5- 15a shows how $R(\theta,d,l)$ varies with angle θ, $R(\theta,d,l)$ goes to a maximum when $\theta = 0^0$. That can be clear for both cases presented in Figure 5- 15a, where, *x* was chosen to be -1cm, *d*=0.5cm, *w*=0.8cm and *l*=1.6cm for the first smaller defect while *x* was chosen to be -1cm, *d*=0.1cm, *w*=1.2cm and *l*=2cm for the second larger one. Those values of *R* show that there will be higher chances for detecting horizontal orientation defects. And this chance reduces by increasing the rotational angle of the defect with the horizontal axis between (40^o- 60^o) and starts to increase slowly until $90^{o,}$. *R* started from 16.62 at 0^o and decreased to 5.3 at 50^o and increased again to be 10.81 at 90^o for the larger defect with

$R(d-0.4, l+0.4, w+0.4)$ while R started from 3.54 at 0^o and decreased to 1.28 at 60^o and increased again to be 1.69 at 90^o for the smaller defect with $R(d, l, w)$. That is obvious for the large and surface closer defect more than the smaller one which has more depth inside the metal. The depth of penetration will be the same for both cases, while the skin depth will affect directly the probability of detect the defect with different depth *d* values as shown in Figure 5- 15b which shows the result of increasing the perpendicular distance between a defect with *w*=0.75cm, *l*=1cm, *x*=1cm and θ=45^o and the conductor surface at *y*=4cm. The values of *R* show that while increasing this distance *d*, then *R* will be decreased too. The skin depth is calculated at the operated frequency as 1.592cm. The defect has better chance to be detected if $d \leq 1.592$ cm so that the eddy current will have tangible values, which it can flows within the defect position and then can change the values of the magnetic flux densities at the measuring points. The large value of *R* (*R* =3.9) when no gab between the defect and the conductor surface is due to the flow of eddy current along the surface. The defect would interrupt the flow of eddy currents which would find it difficult to go deep because of the value of the conductivity of the defect and due to skin effect. The example in Figure 5- 15c takes fixed values for *w*, *d*, *x* and θ as 1cm, 0.5cm 1cm and 90^o for the same operating frequency of 10 Hz. It is noticed that the values of *R* increased sharply by increasing *l* up to 0.75cm, while the increase in *R* becomes slow at values of $l \geq 0.75$ cm. This is due to skin depth of 1.592cm, since the part of the defect that is locating out the depth of penetration distance will be harder to be detected and will have small contribution on the value of *R*, but it will still affect the resulted magnetic flux density values at the measuring points. A study of the relation between defect length *l* with *R* is presented in Figure 5- 15c. It is shown that increasing the length of the defect will be a sign of increasing its size, so that, it will be resulted in increasing the interpretation of the eddy current and then increasing the values of *R*. Figure 5- 15d shows the relation between width of the

defect and $R(\theta,d,l)$ which considered as the relation between detecting the defect and its size too. It is shown that for a fixed depth d=0.2cm and angle of rotation θ= 60°, $R(\theta,d,l)$ will increased by increasing w at fixed x=1cm and length l=1.5 cm.

Defining x; the horizontal distance of the defect from the entire domain's center and the defect as was shown in Figure 5-9 will give an indication regarding the coil horizontal position due to defect. Taking three values of x as: x_1=-2.25cm, x_2=0 cm and x_3=2.25cm respectively and plotting the value of R at these horizontal distances as shown in Figure 5-16a for w=1cm, l=4cm and θ=12°.

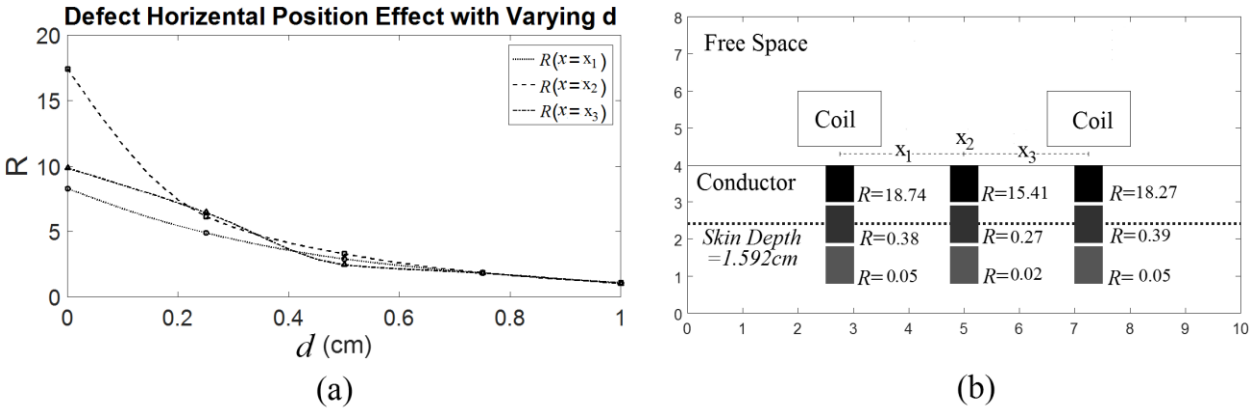

Figure 5-16 Horizontal defect central distance effect on R for three different x values: x_1=-2.25 cm, x_2= 0 cm and x_3=2.25 cm. (a) R at x= x_1, x_2 and x_3 vs. d as the depth of the defect for w=1cm, l=4cm and θ=12° . (b) Values of R according given values for both x and d in Table 2 where w =0.5 cm, l=1cm and θ=90°

It is shown that the horizontal position of the defect will affect its detection probability. By moving horizontally away from the coil center position, the strength of the eddy current density will be decreased. And this can be shown for plotting R as a function of d for three horizontals x distances of: -2.25 cm, 0 cm and 2.25 cm as seen in Figure 5- 16a. At deeper perpendicular distance (large value of d compared to skin depth of: 1.592 cm), R-values will be close to each other as excepted. Figure 5- 16b shows some discrete values of R with given values of x and d in to Table 5-2 where w =0.5 cm, l=1cm and θ=90°.

Table 5-2 Values of R for both x and d where w =0.5 cm, l=1cm and θ=90°

	d=0 cm	d=1.1cm	d=2.1 cm
x=-2.25 cm	R=18.74	R=0.38	R=0.05
x=0 cm	R=15.41	R=0.27	R=0.02
x=2.25 cm	R=18.27	R=0.39	R=0.05

It is shown that R has large values when no gabs between these defects and conductor surfaces, while these defects will have smaller vales of R by increasing d . Three values of x were chosen, two of them directly at the center of the coils where R will be the maximum at these locations due to the larger values of eddy current on these points since they are directly below the coils. While the values of the eddy currents decrease by moving far from these points as moving toward x_2, where R will still have relatively high value at this point if d=0 but R will decrease by increasing d for the three cases as shown before in Figure 5-15.

Example 5.6, Minimization Processing Time for Direct ECT Problems

Figure 5-17 shows how using SFEMSFEM will be used to minimize processing time. Define T_{R2} and A_{R2} as:

$$T_{R2} = \frac{t_2}{t_{Tot}} \tag{5.3a}$$

$$A_{R2} = \frac{A_2}{A_{Tot}} \tag{5.3b}$$

Where: t_2 is time for processing region two only which is the defect region, t_{Tot} is the total time for processing the complete domain with both regions one and two, A_2 is the area for region two and A_{Tot} is the total area for both regions one and two.

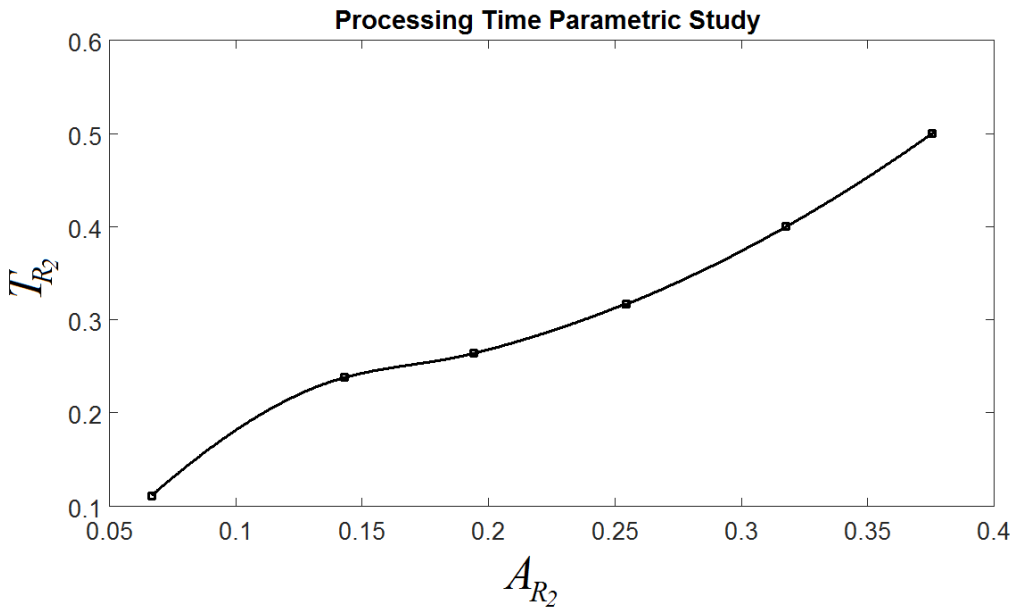

Figure 5-17 Normalized subregion areas (different areas for both R_1 and R_2) for the same 90° defect problem Vs. Normalized processing time for region R_2, R_1+R_2=80cm^2

Increasing A_{R_2} that's defiantly will increase T_{R_2}. The maximum value for processing time will be when A_{R2}=1 where SFEMSFEM will be turned to classical FEM by making the selected region of defect represents the entire domain. This result is logical if the total area increased by increasing both areas of R_1 and R_2 since increasing the areas of the solution domain will increase the number of meshes and makes it takes longer time in processing. Table 5-3 shows how increasing the number of elements for both regions or one region (R_1 or R_2) for a fixed domain (fixed dimensions) will increase processing time for the case shown in Figure 5-11b.

Table 5-3 Study the effect of controlling the minimum element area of the given problem for a fixed 90^o defect problem in Figure 5-11b with fixed area of $80cm^2$

Elements minimum area (cm^2)	Number of elements in R_1	Number of elements in R_2	Number of elements in total domain	Processing time for total domain (s)	Processing time for R_2 (s)
0.05	2380	260	2640	38.4	4.4
0.04	2952	288	3240	71.6	10.5
0.02	5902	445	6347	515.5	45.6
0.01	11942	792	12734	4179.3	380.3

The first case in Table 5-3 shows that processing time needs 38.4s to get values of the potential fields at all nodes for the problem that was described in Figure 5-11b. Updating the profile for R_2 will not need 38.4 s again for getting the required answer. It will take 4.4s to update the data profile for R_2 and solving the SFEMSFEM equations (3.19) to get the magnetic potential fields at all nodes. Finally, the same solution process will be for both cases as plotted in Figure 5-13b. That means a big save in time will be achieved as mentioned before.

5.3 Inverse Eddy Current problem

An inverse problem in science is the process of calculating from a set of observations the causal factors that produced them: for example, calculating an image in computer tomography, source reconstructing in acoustics, or calculating the density of the Earth from measurements of its gravity field.

In our work, we need to use the concept of inverse problems to re-characterize defect shapes so we can evaluate whether these defects are major or minor and then if they will affect the performance of the system or not.

We will use two optimization techniques in our analysis, Genetic Algorithm and Simulated Annealing optimization techniques. I will use same method and updates codes which have been used in [115, 116] for similar problems.

The first step for characterizing the defect will be to detect its location. After that we will use inverse problem techniques to characterize it. After detecting the defect, we investigated more on defect characterization. Defect Characterization means knowing its size, shape, physical construction and properties, exact location. Next, we measure its effect on the total performance.

Our comparison will be with no defect case. By knowing the response when there is no defect, if the response is different because of the crack whether its hidden inside the material or not, the test object is presently flagged as defective and the plate is sent for repair without assessing if the defect is serious enough for removal from service. In my work, this technique is extended here for purpose of characterization. An iterative approach is presented that repeatedly employs SFEM technique for modeling the forward problem to characterize the shape of defects in a steel plate.

The defect can be assigned to several design parameters, that will be used to characterize its shape as seen in Figure 5-18.

The defect can be assigned to design parameters. Predicting that we know the defect design parameters as we get these results from the experimental testing. That will be used to characterize defect shape as seen in Figure 5-18.

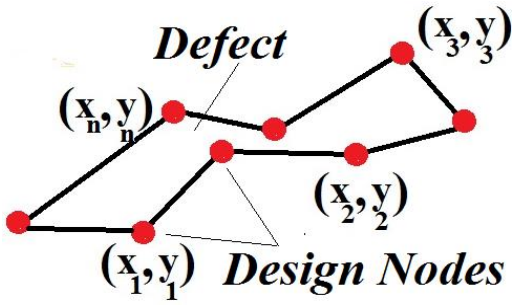

Figure 5-18 Defect model with design parameters

Those design parameters are presented by matrix [*h*] as:

$$\{h\} = \begin{bmatrix} x_1 & y_1 \\ x_2 & y_2 \\ \bullet & \bullet \\ \bullet & \bullet \\ x_n & y_n \end{bmatrix} \tag{5.1}$$

where these *x* and *y* coordinates in $\{h\}$ represent key points for the unknown defect. We are free to choose these points as we can see from Figure 5-18. The best choice for these points will come after solving the inverse problem by choosing the appropriate optimization technique.

An object function *F* is defined as the sum of the squares of the difference between computed and measured (defect) performance values at measurement points at all measuring points,

$$F\left(\{x_1, y_1\}, \{x_2, y_2\}, \cdots, \{x_n, y_n\}\right) = \sum_{i=1}^{measuring\ points} \left(B^i_{Calculated} - B^i_{Measured}\right)^2 \tag{5.2}$$

F will represent the object shaping function. By minimizing the object function *F* with respect to the parameters by any of the optimization methods, the characteristics of the defect can be estimated.

The computational process in the defect identification system is shown in Figure 5-19. It needs to solve the design parameters $\{h\}$. First, the mesh needs to be generated for the given design

parameter. Mesh generation is a very important part of FEM analysis based design optimization. Instead of solution using classical FEM method [108, 109, 111, 112], we will not be able to use a parameter based mesh generator as in [117] , because in every iteration, the mesh must be generated automatically when design parameters change. These types of special parametric mesh generator will generate different numbers and sets of elements in each iteration to calculate the magnetic vector potential. The subregional inverse FEM problems objective is to divide the solution area into different regions. After that, we will pick up our region, which will be our work region that contains the requested design. Generating new meshes with new number of elements and nodes inside this region will make applying equation (3.2) and then (3.6) and (3.19) impossible because of changing the number of the potential values at the interior nodes not changing their values. The source of stability for these equations is to keep this number fixed in each iteration. Triangles must be modified for flexible, nonstop optimizations way to save connectivity matrix and then save the connection between nodes and the same number of the interior nodes to apply the SFEM in our inverse problem. This can be done by applying an elastic mesh generating technique which was introduced in Chapter 4. The authors of [114] apply this method to reduce processing time in some Magnetostatic pole design problems. We updated this method to use it in Eddy Current problems.

The objective for our analysis is to compute the magnetic vector potential for all the system. After computing vector potential values, the magnetic flux density $B^i_{Calculated}$ is computed and the object function F is evaluated. When the object function F is minimum, the parameters $\{h\}$ will be found. If F is not minimum, the design parameters will be changed using the optimization method being used for the known defect which is known as true profile. $B^i_{Measured}$ should be calculated first. Then faking that we do not know the shape of the defect, we generated hundreds of different shapes of

defects using our algorithm. $B^i_{Calculated}$ was calculated each time. Comparing $B^i_{Measured}$ and $B^i_{Calculated}$ the object function F is evaluated each time and optimized. When F is minimum, the reconstructed shape of the defect is generated.

The block diagram in Figure 5-19 explains in detail how we can detect and characterize a hidden crack in metals using our proposed algorithm.

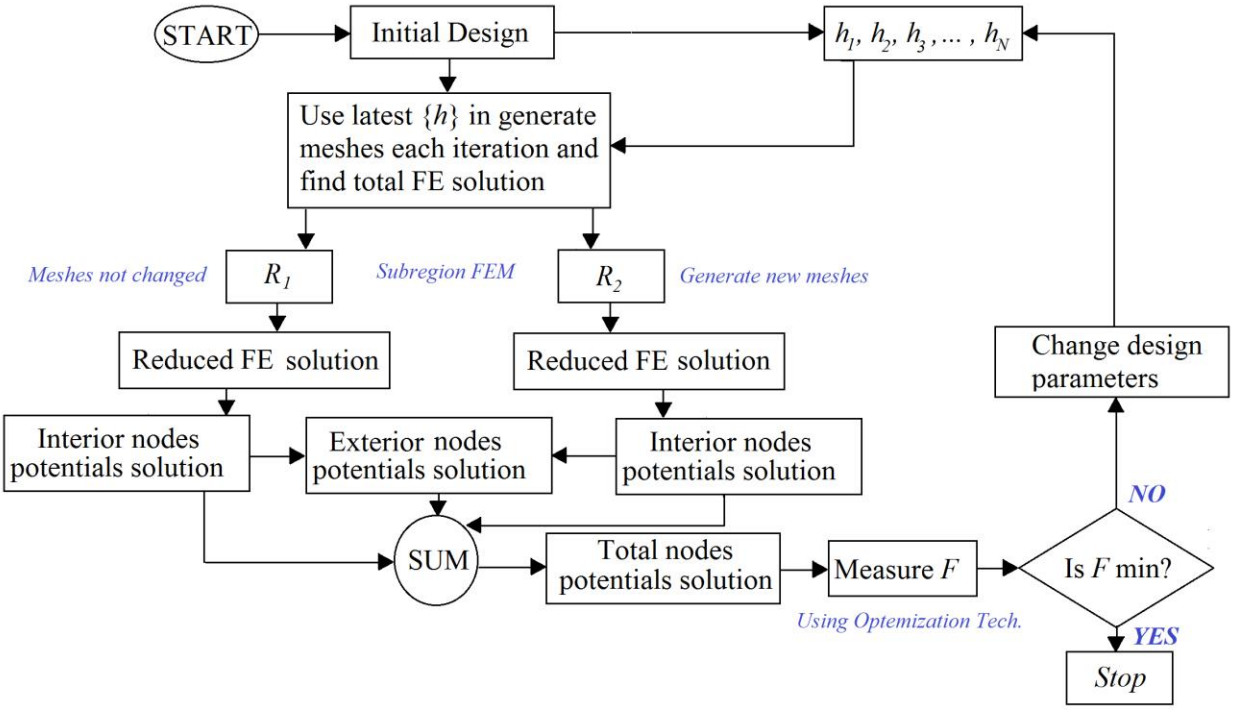

Figure 5-19 Design cycle for solving inverse ECT using SFEM

The first step is to do a complete FEM Analysis for the whole problem. We will find the values of magnetic vector potentials for all nodes. After that we will find the values for the magnetic flux density in all elements. We can see the values of the magnetic flux densities at some measuring points too.

Our first mission in our solution is to know if we have a crack or not. Then we need to know whether this crack is tangible and affected the performance of the system or not. We can determine an initial location for that defect by measuring the values for the magnetic flux densities in all elements and compare these values with no defect values.

The following plot in Figure 5-20 shows the values of the magnetic flux density for each element in no defect case for the problem in Figure 5-9. This can be saved as a reference file to be used later.

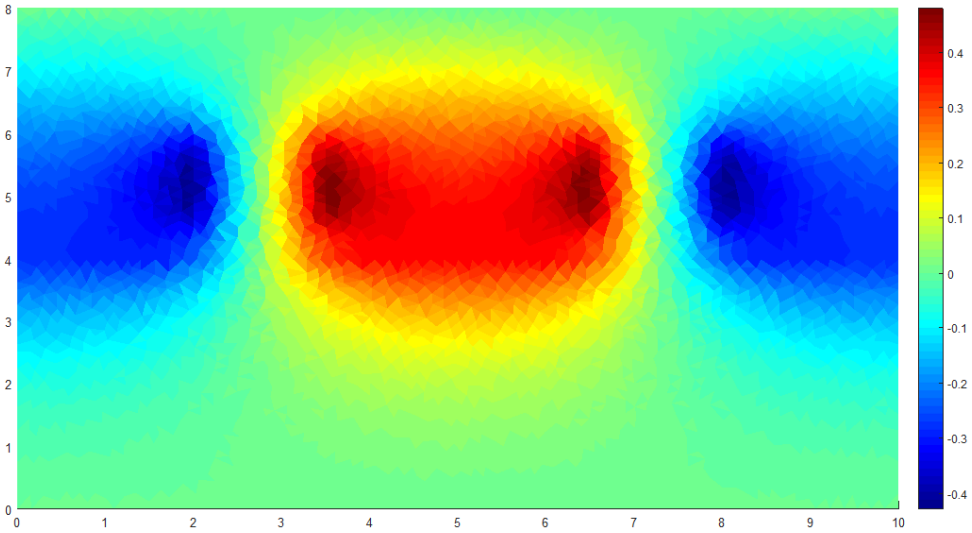

Figure 5-20 Finite Element Solution for the entire domain which finds the magnetic flux density at each element in no defect case.

There is a complete symmetry for this plot. The highest values of the magnetic flux densities will be in the middle distances between the two coils and that is logical since the both locations will have the summation for the positive two values of the magnetic flux densities. We used the values of the magnetic flux densities in the no defect case as a reference for detecting the initial position of the defect if it is existing.

Now, we will return to the original problem for Figure 5-9 and we will consider that we have an arbitrary 2D defect as shown in Figure 5-21.

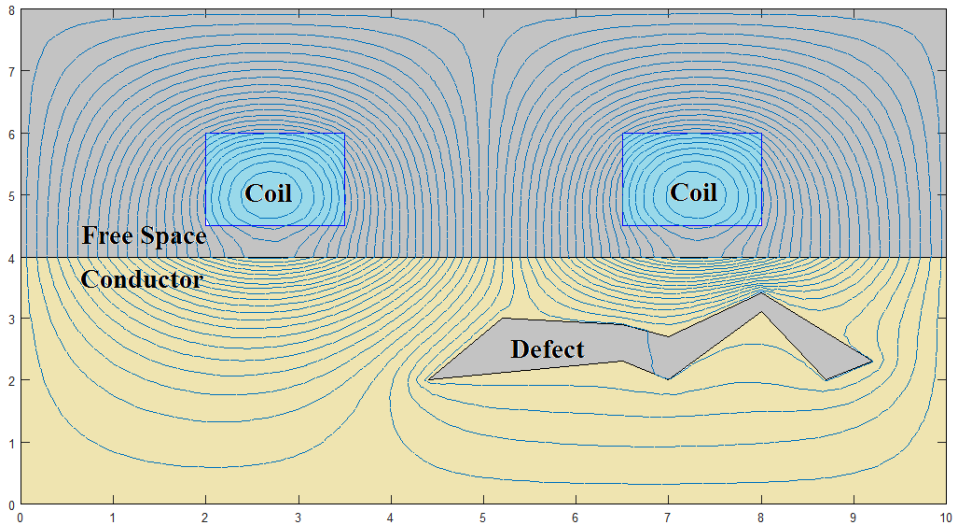

Figure 5-21 Arbitrary 2D defect and resulted vector potential lines

We can see the victor potential lines in the same plot and we can notice the change in these lines because of the defect. To choose the initial defect region R_2 we need to make a calculation for magnetic flux density for the entire domain. After that we can choose our regions and then apply the subregion method.

The following plot shows how magnetic flux density distributed along the entire domain of the problems.

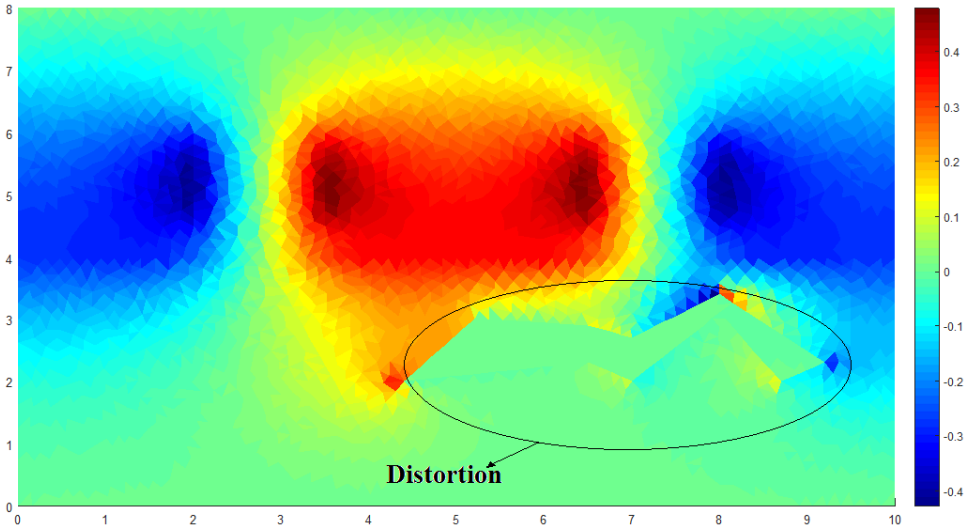

Figure 5-22 Finite Element Solution for the entire domain which finds the magnetic flux density at each element in defect case.

We can notice that there is a distortion in the selected area. We can compare this result with that in Figure 5-20 when the magnetic flux density was plot in the no defect case. This region is selected as defect region (R_2). To give more details about this region, the following figure shows the plot of the difference between magnetic flux densities in defect and no defect cases as:

$$B_{difference} = B_{defect} - B_{nodefect} \tag{5.3}$$

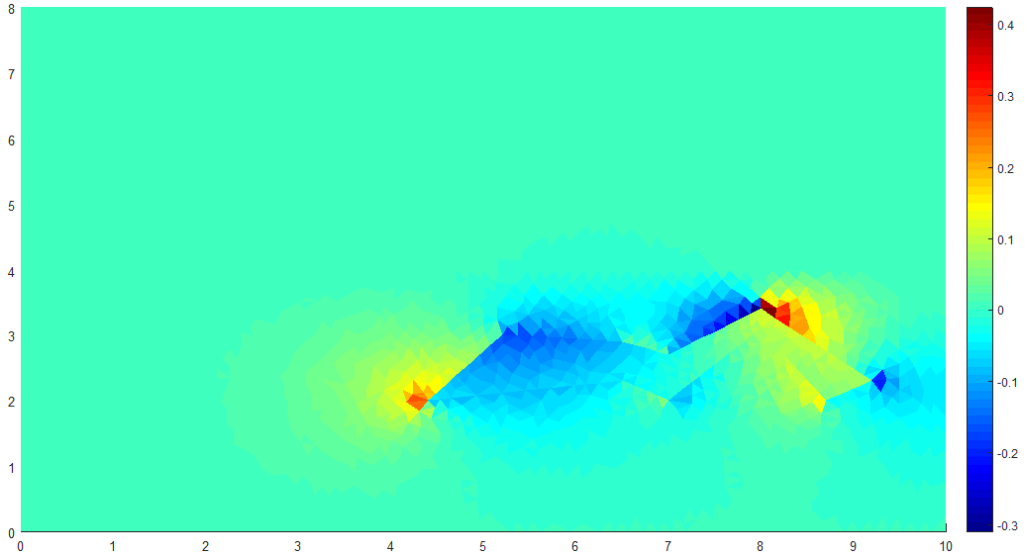

Figure 5-23 Difference of magnetic flux densities between defect and no defect cases at each element.

The difference has tangible values at the defect location, where its values floating around zero while we move far from the defect position. All these results will give us an indication of the crack location, also it may give an initial guess regarding its shape.

After that we can setup a defect subregion area named R_2. In this step, we will apply the SFEM method to find magnetic vector potentials in this region R_2 and the reminder region R_1. This will be done as we did in first part of this chapter in. In this step, we will divide nodes to interior and exterior nodes. These nodes will be the key of our solution. When we obtain all these values of the magnetic vector potentials, then we will reconnect the FEM solutions for both regions R_1 and R_2

again to find the total solution, so we can find the values of the magnetic flux densities at the measuring points. Then we will use inverse problem techniques to get the best defect shape characterization. In our work, we used both Genetic Algorithm and Simulated Annealing Optimization Techniques as colleagues used in their previous research in [115, 116]. We see from the block diagram in Figure 5-19 that we calculated our cost function at the measuring points. According of the resulted values, we can determine whether to stop our solver or continue to reshape the defect. If we find F in equation (5.5) is not minimum, then we will get a conclusion that our solution is not optimal. That means the generated defect is not close to the original one. Therefore, we will need to generate new meshes. The presented technique is to use a flexible elastic131 method in generating the new meshes. We will use the technique which was introduced in Chapter 4 for only just the predetermined defect region, which is R_2. This means we will not change the connectivity matrix for the entire domain. And we will move nodes according to a mathematical scheme within R_2 but under the condition of saving and keeping the same connection between these nodes. This process of solving is clear in the Figure 5-19 which means we only play with nodes not the elements. And this will save time and will be more flexible and will give accurate results. The purpose of using this technique in this time is we are using subregion technique. This means we divided each region to both interior and exterior nodes. We have positions for the exterior nodes at the interface between these two regions. And to get a final solution for any problem that used the subregion method migrate with FEM, we should combine both regions using the interfacing exterior nodes between regions. These positions contain information that cannot be changed. So, using any other meshing algorithm inside R_2 may change:

1) Number of nodes even interior or exterior in R_2.

2) The position of the exterior nodes in case we keep the same number of nodes while generating new meshes.

So, I found that the best solution is to use this technique of saving connectivity scheme and generalize it to fit all kinds of problems. Therefore, we will keep changing the position of the interior nodes within the defect region R_2 until reaching the optimal values of F which is the minimum value. In this case we will stop the algorithm and we can return to our profile of the interior nodes inside R_2 to select defect nodes. Then we characterize it and find its shape. We should know that we can do a lot of constrains in our solution. Each constrain has its special purpose. And that will be clear from the solved example.

Example 5.7, Reconstruction Shape of the Hidden Defect by Using SFEM

Consider the following model in Figure 5-24 which is used to validate the Subregion Finite Element Method in solving ECT Problem. The objective for this problem is to detect the hidden defect, then to characterize it using the proposed algorithm. The coil (with $\mu_r = 1.0$, and current density $J = \pm 100\ \mathrm{A/cm^2}$) excites the magnetic field in the steel plate (with $\mu_r = 100.0$ and current density $J_0 = 0.0$). The conductor is surrounded by air (with $\mu_r = 1.0$ and current density $J = 0.0$). The magnetic flux density in the *y*-direction B_y is measured at $y = 4.5$ cm, $4\ \mathrm{cm} \leq x \leq 6\ \mathrm{cm}$ using 10 points as shown in Figure 5-24 labeled as the measuring line.

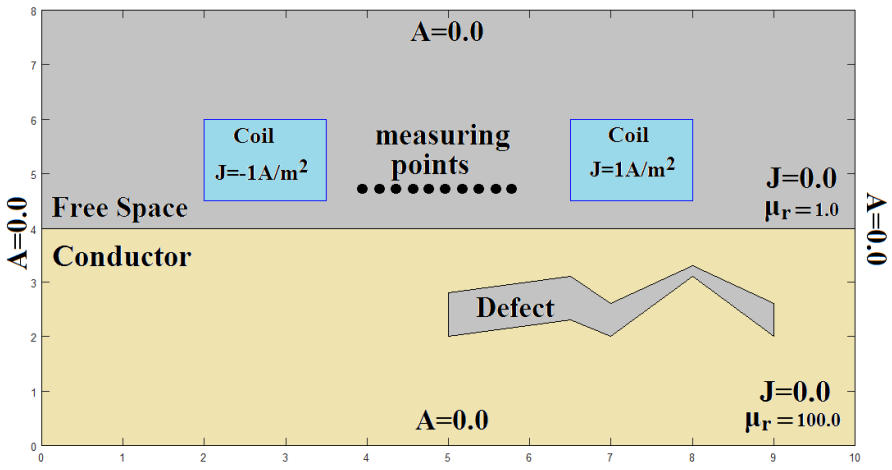

Figure 5-24 Given parameters for a 2D ECT problem in Example 5.7 with the true defect.

On each node on the defect, the vertical displacements are selected as design parameters. In our numerical model we have 10 geometric parameters instead of 8 as used in [115, 116] contained in the vector $\{h\}$:{ h_1, h_2, h_3, h_4, h_5, h_6, h_7, h_8, h_9, h_{10}}. This will give more accurate results. The measuring line located at y = 4.5 cm, is sampled to ten equally spaced points and tolerance boundaries on $\{h\}$

To start our solution, R_1 and R_2 should be selected first; next our design parameters will be identified inside R_2. Those design parameters should be on the surface of our predetermined defect as in Figure 5-18. Each design variable is represented by 10 bits to be used later in Genetic Algorithm. For testing, defect was used with the following fixed design parameters nodes coordinates:

$$\{(5,2),(6.5,2.3),(7,2),(8,3.1),(9,2),(9,2.6),(8,3.3),(7,2.6),(6.5,3.1),(5,2.8)\}$$

Starting from these points, $\{h\}$ will be calculated each iteration to find the original defect shape as we chose the y-directions of these design parameters as:$\{h\}$= {2.0. 2.3, 2, 3.1, 2, 2.6, 3.3, 2.6, 3.1, 2.8} cm and computed the field $B^i_{Measured}$ at the measuring points.

These design parameters will be treated as our design nodes in our method of solution. An initial defect shape will be generated with saving the node numbering as done for the first time of these designing nodes. After that SFEM will be used to change positions for these nodes until getting our solution which will be the most accurate defect shape and the reconstructed $\{h\}$ will be generated each iteration to match the measurements $B^{i}_{Measured}$.

After determining the defect region and name it as R_2, the remainder area will be considered as a fixed region with fixed nodes and elements and this will be R_1 as shown in Figure 5-25.

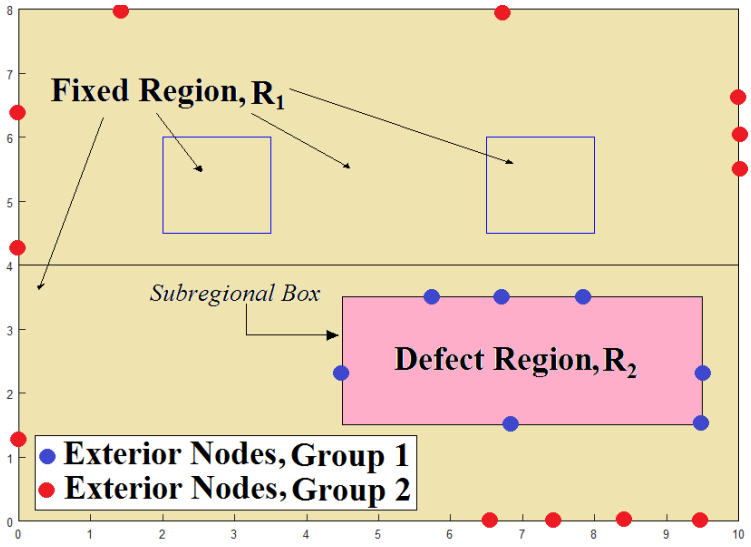

Figure 5-25 Dividing the entire problem domain to R_1 and R_2 and showing exterior (interfacing) nodes for both regions.

The next step will be to determine groups of nodes for each selected region. Each region should have two sets of nodes; interior and exterior nodes. At least one set of exterior nodes should be common between both regions for applying subregion method.

For the reminder region; the bigger one R_1, will consists of two sets of the exterior nodes (Group 1 and Group 2) as shown in Figure 5-25 where the exterior nodes in Group 1 of nodes will be at the interface between both of R_1 and R_2. Those are the common nodes between both regions. Those nodes will be used in equation (3.19) as the interfacing exterior nodes between both regions. Nodes

that belong to Group 2 are also considered to be exterior nodes for R_1. Those are the boundary nodes and their values are upon the given data. In our example, zero potential values are imposed for these nodes.

The reminder nodes within region R_1, which are not belong to Groups 1 and 2 will be saved as the interior nodes for R_1 and will be used in equation (3.6). Our SFEM solver is designed to determine both interior and exterior nodes for R_2 where nodes belong to Group 1 are exterior nodes for R_2. Those are the common set of nodes in R_1. While the reminder nodes inside R_2 are considered as interior nodes for R_2.

After selecting nodes for both regions, a sub-regional Finite Element solution will be implemented for both regions. The important issue will be in creating two profiles for both regions. Then saving results in these two profiles to be used later in the inverse part to detect the shape of the defect. The profile that contains the resulted data of R_1 will be fixed and created only one time. While continuously updating data in the profile that is related to R_2. This is because SFEM will continue among the given iterations until achieving the optimal solution which is the best score function value. That means the best reconstructed shape of the hidden defect which happened at minimum value of F in equation (3.5). To update the data for R_2, new meshing scheme will be generated every iteration. The only things that will have changed will be the position of the nodes and the values of their resulted vector potential values, Changing the position of the interior nodes in R_2 means that a resulted change on the predetermined design parameters and the magnetic flux density is then calculated $B^i_{Calculated}$ along the measuring line. The object function F is evaluated by comparing $B^i_{Calculated}$ with $B^i_{Measured}$.

It is necessary to impose constraints to get a single defect [115, 116]. So, to maintain a realistic shape with a single defect, node 10 is on top of node 1, node 9 on top of node 2, node 8 on top of

node 3 and node 7 on top of node 4 and node 6 on top of node 5, as shown later in Figure 5-18, where 10 nodes are used as designing nodes and by imposing the constraints as $h_{10}>h_1$, $h_9>h_2$, $h_8>h_3$, $h_7>h_4$ and $h_6>h_5$: Therefore, single and realistic defect will be created

In our simulation, both of Genetic Algorithm and Simulated Annealing as used in [115, 116] are used as optimization techniques to calculate fitness score function each iteration. These optimization techniques will be used to find and calculate the best fitness score. To apply these optimization techniques in our proposed method, the object function F is calculated at each iteration. After that, new meshes inside the defect region R_2 will be generated using the elastic meshing and then get new defect shape each iteration until having the best defect shape. Next, evaluate the performance of the complete system by calculating F. Figure 5-26 shows the block diagrams for both optimization techniques used in this SFEM solution. Both methods gave excellent results. Those block diagrams can be plugged in the main SFEM flow chart in Figure 5-19 for optimization and calculating F and then make the decision of processing continuity or not.

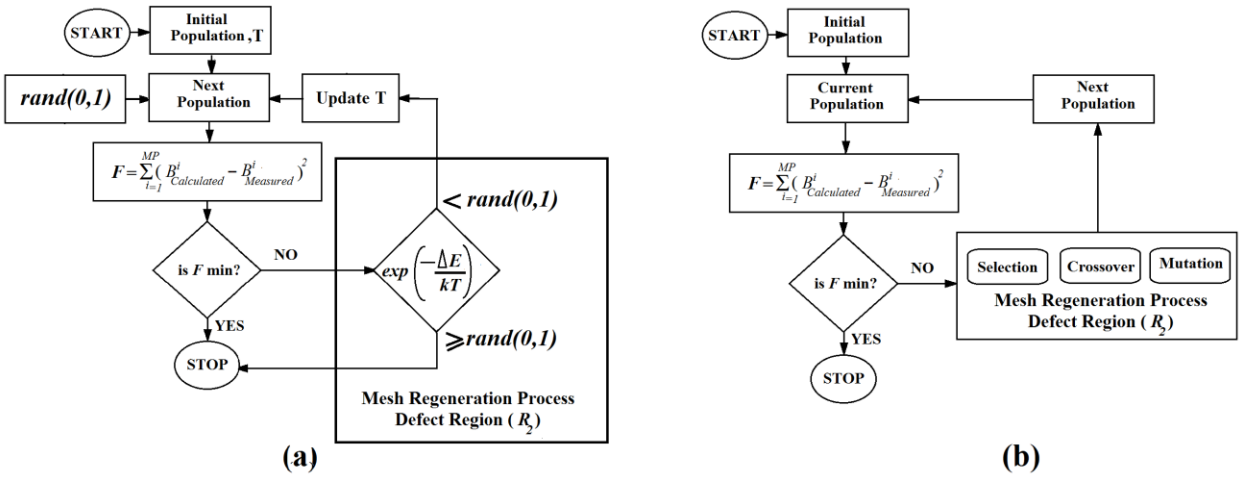

Figure 5-26 The used optimization techniques in the presented inverse SFEM ECT problem in order to get the optimal defect construction [115, 116]. (a) Using Simulated Annealing (SA). (b) Using Genetic Algorithm (GA)

Several simulations of defect characterization problem were run and the results were tabulated using both optimization techniques. The best fitness score using Genetic Algorithm was achieved when the population size is 48 for the 25 iterations as shown in Table 5-4.

Table 5-4 Fitness scores and processing time using GA for different iteration numbers.

Population size	5 iterations		15 iterations		25 iterations	
	Time(s)	*F*	Time(s)	*F*	Time(s)	*F*
6	409.22	0.0785	951.12	0.0541	1914.21	0.0453
18	700.21	0.0614	1801.21	0.0497	3001.15	0.0281
30	1085.55	0.0480	3459.17	0.0270	4701.55	0.0146
36	1294.64	0.0329	4139.13	0.0118	6424.32	0.0054
42	2538.98	0.0144	4859.64	0.0032	6613.05	0.0013
48	3722.83	0.0063	4481.67	0.0014	7309.36	0.0005

The verification of Genetic Algorithm is achieved by increasing both iteration numbers and populations size which means better values and being closer to the optimal solution of the fitness score.

The best fitness score using Simulated Annealing was calculated through:

$$P(E) = e^{\frac{\Delta E}{kT}} \tag{5.7}$$

Where $E=\Delta f$, k is Boltzmann constant , T is average value of f and P will be generated randomly each iteration to achieve the optimal value of the fitness score. Δf is the difference between current and previous score values. When we change the coordinates y_{old} from previous to current values $y_{current}$, this will lead to change F from f_{old} to f_{new}. $\Delta f = f_{new} - f_{old}$ which is equivalent to E in Simulated Annealing.

Excellent results were found using Simulated Annealing optimization as shown in Table 5-5.

Table 5-5 Fitness scores and processing time using SA for different iteration numbers.

Iterations	10×10	20×20	30×30	40×40	50×50
F	0.0784	0.0530	0.0391	0.0272	0.0214
Time (s)	40.21	45.77	54.43	60.43	75.15

It is clear that increasing number of iterations will make solution closer to optimal value. In addition, this will increase processing time as done using Genetic Algorithm in Table 5-4.

Our objective in this study is to get an accurate shape for the hidden defect so we can study its effect on the entire system. This is clear from fitness score values per each case using Genetic Algorithm. In our solution, Genetic Algorithm needs more computational time in processing since it takes three steps in determining the next population which are: selection, crossover and mutation. It is binary coded algorithm; it takes time to convert to real numbering system in our computational solution.

Perfect matching between both defects profiles as seen in Figure 5-27 that shows the optimum shape of the reconstructed defect vs the accurate one. To measure the accuracy of the reconstructed defect, the length from the centroid of the true profile to each point was calculated using equation (5.8).

$$e = \frac{\sum_{i=1}^{n}\left(\frac{r_{true}^{i} - r_{reconstructed}^{i}}{r_{true}^{i}}\right)}{n} \tag{5.8}$$

where r_{true}^{i} is length from the centroid to the true profile, and $r_{reconstructed}^{i}$ is the length from the centroid to the reconstructed profile, where n is the number of coordinates in the profile.

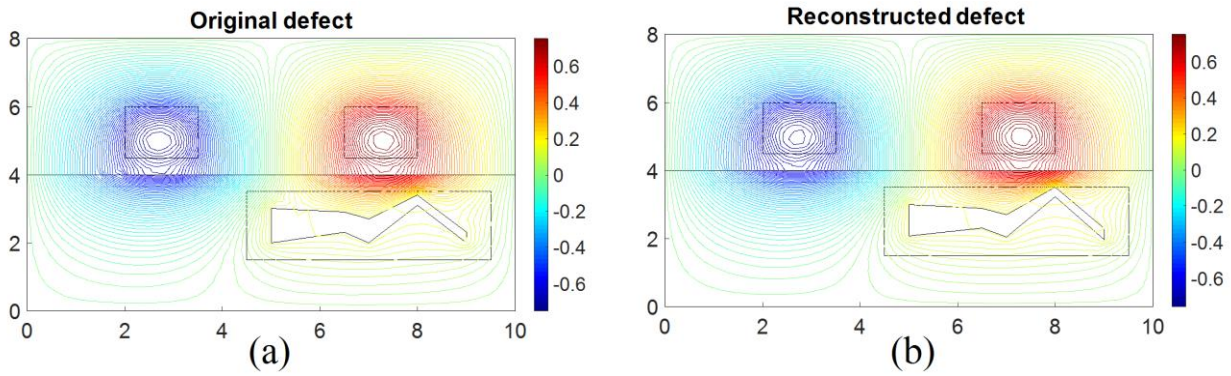

Figure 5-27 Equipotential lines using SFEM (a) Original Defect. (b) Reconstructed Defect.

The calculation process for our numerical model is calculated using equation (5.8). The resulted values are all tabulated in Table 5-6.

Table 5-6 Calculating defect accuracy for computational example.

Original Node number	**Design Parameter number**	**True Defect Profile**			**Reconstructed Defect Profile**			$\left(\frac{r^i_{true} - r^i_{reconstructed}}{r^i_{true}}\right)$
		x	y	r^i_{true}	x	y	$r^i_{reconstructed}$	
9	h_1	5	2	2.1189	5	2.069652	2.096983	0.010372
10	h_2	6.5	2.3	0.6403	6.5	2.298805	0.64106	0.001167
11	h_3	7	2	0.7	7	2.044291	0.655709	0.063273
12	h_4	8	3.1	1.0770	8	3.220627	1.12741	0.046774
13	h_5	9	2	2.1189	9	1.96676	2.130174	0.005291
14	h_6	9	2.3	2.0396	9	2.293784	2.040836	0.000602
15	h_7	8	3.4	1.2206	8	3.5	1.280625	0.049129
16	h_8	7	2.7	0	7	2.697894	0.002106	*eps*
17	h_9	6.5	2.9	0.5385	6.5	2.875489	0.529902	0.015996
18	h_{10}	5	3	2.0223	5	2.987524	2.020562	0.000896

This calculation gives error e = 2.1%, which means an accuracy of 97.9% in the average reconstruction of the defect. For the reconstructed profile, the finite element solution of the magnetic vector potential is shown in Figure 5-27 where COMSOL was used to validate the SFEM results as shown in Figure 5-28.

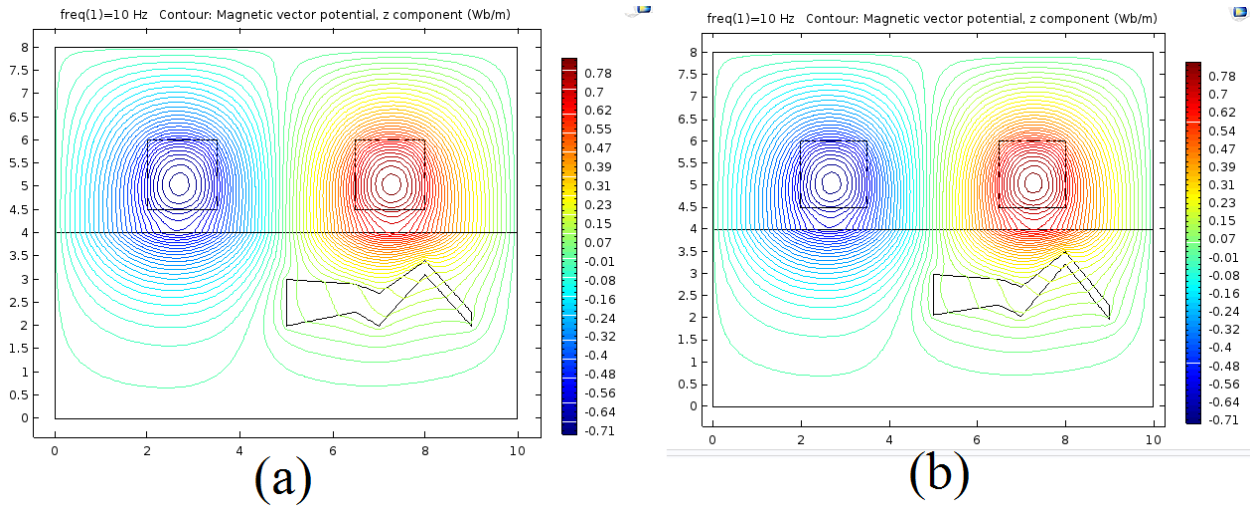

Figure 5-28 Equipotential lines using COMSOL (a) Original Defect. (b) Reconstructed Defect.

An excellent agreement between the values of the magnetic vector potentials using COMSOL in Figure 5-28 and SFEM in Figure 5-27 which can be used in applying SFEM in other physical problems.

Those results of the vector potential lines will be evaluated later in a post processing terminology to evaluate the performance of the system that contains this defect. From the resulted vector potential lines, we can notice the effect on these potential lines. Moreover, this maybe a source of technical problem.

Modeling SFEM by using GA with 25 iteration and population size of 45 will be used to prove that using SFEM can be considered as an excellent mathematical method, which can be used, in regular lab CPUs to perform computations. Figure 5-29 shows how using SFEM will be used to minimize processing time. Defining T_{R2} and A_{R2} as done before for direct SFEM as:

$$T_{R2} = \frac{t_2}{t_{Tot}} \tag{5.9a}$$

$$A_{R2} = \frac{A_2}{A_{Tot}} \tag{5.9b}$$

Where: t_2 is time for processing region two only which is the defect region, t_{Tot} is the total time for processing the complete domain with both regions one and two, A_2 is the area for region two and A_{Tot} is the total area for both regions one and two.

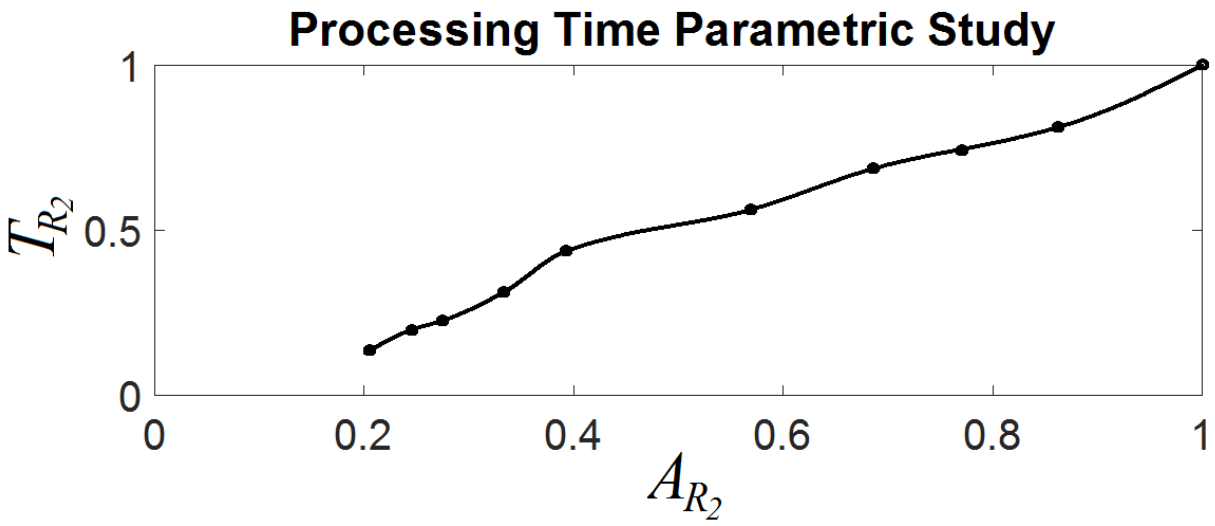

Figure 5-29 Normalized subregion areas (different areas for both R_1 and R_2) Vs. Normalized processing time for region R_2, R_1+R_2=80cm^2

Increasing A_{R_2} that is defiantly will increase T_{R_2} because of increasing FEM processing area. The maximum value for processing time will be when A_{R2}=1, where SFEM will be equivalent to classical FEM by making the selected region of defect represents the entire domain. Time minimizing ratio between SFEM and classical FEM is not fixed; it is a positive value less than or equal to 1.0; (0.1 as seen in Figure 5-29; this value depends on the area of R_2) and it becomes 1.0 when defect region R_2 represents the total region R_1+R_2. The used optimization technique and choosing population size and iteration numbers and constrains affect SFEM processing time. The main conclusion will be by increasing processing time when defect region area R_2 increases as shown in Figure 5-29. For more accurate results, R_2 should be allocated carefully according to

magnetic flux values for the entire domain. To achieve convergence of solution, it is recommended to choose R_2 with at least twice element length distances from boundaries and primary defect circumference.

6 Experimental Validation for Subregion Finite Element Method

An experimental validation to SFEM will be presented in this chapter in addition to COMSOL and conventional FEM that were presented in Chapter 5.

Multiple samples were tested to validate the presented results in the NDE Lab in MSU, where we use TMR sensor to collect data by scanning it through some measurement points. An elongated coil has been used as an excitation coil. The input voltage used was 10 V_{pp} with the required testing frequency. We used a frequency range of (10 Hz-1 kHz). The following constrains should have been taken in consideration while setup the experiments:

- The sensor needs to be scanned above the excitation coil.
- The sensor position above the coil might not be in the best location, we could not scan under the coil.
- We could not select the points that are theoretically the best as a measuring points, the best that we can do is to measure above the coil as close as possible.
- The objective of this dissertation is to validate the presented algorithm in solving 2D- ECT problems by doing an experimental setup that validate the presented computational examples presented in Chapter 5.

The experimental setup was done for testing the following samples: aluminum with edge defect, steel with surface defect and aluminum with subsurface defect. Excellent results have been achieved.

The following block diagram in Figure 6-1 shows how we setup our experiments to test our samples.

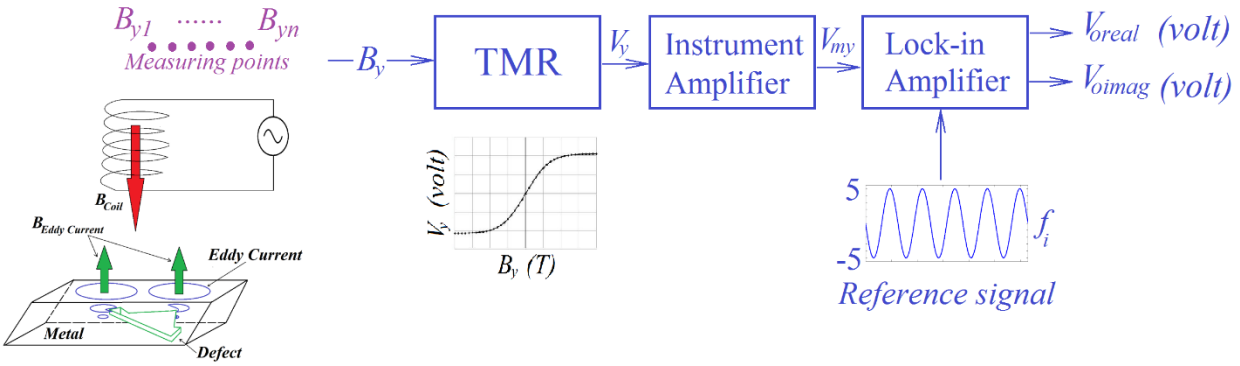

Figure 6-1 Eddy Current Testing using TMR sensor used in our experimental Validation

The excitation coil that contains the AC input voltage will be the source for the first part of the magnetic flux density at the predetermined measuring points B_{Coil} (T). While, the eddy current will contribute the second part as $B_{Eddy\ Current}$ (T). We are dealing with 2D-problem, so we will choose B_y as the normal values that we are planning to test using TMR sensor at these measuring points. The TMR sensor is placed on a scanner that scans the surface of the tested sample where it will read the values of the normal magnetic flux densities B_y (T). Then it will convert these values to a related voltages V_y (volt). it is necessary to note that we are plan to have values of B_y lie in the linear region of the sensor. Therefore, we will have a proportional output voltages. If the values of B_y are high, then there is a chance to input the saturation region of the sensor. This will be a limitation for the coil size. These voltages V_y (volt) are small related to input values, so we need to amplify these values. To do that, we will use an instrument amplifier with a gain G_m. The output of the amplifier (V_{my})then will be: $G_m V_y$ (volt). This amplified signal will be then input to a lock-up amplifier to measure phasor parameters for V_{my} (volt). We can use the same input voltage as a reference voltage to measure the phase of the output signal. This lock-in amplifier has low-pass filter in addition of a circuit that used to amplify the signal. Therefore, the output of this lock-in amplifier will be two readings, the first one as real output signal V_{oreal} (volt) and imaginary signal as V_{oimag} (volt). There may be a small phase shift in the output voltages due to the existence of the

low pass filter in the lock-in amplifier. Where we can then find a relation between the resulted output voltages and the magnetic flux density values. This relation is linear and the resulted signal will be a scaled version for B_y. More details will be explained through this chapter.

6.1 Edge Defect Experimental Setup for Aluminum Sample.

An initial validation for 2D SFEM is done on the edge of healthy Aluminum sample as shown in Figure 6-2.

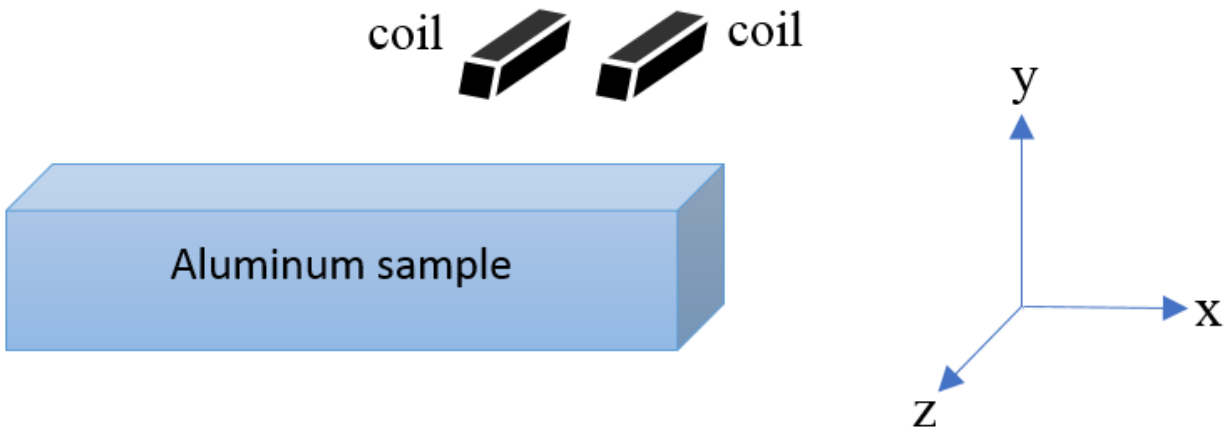

Figure 6-2 Aluminum sample and coils position for edge defect example

This setup in Figure 6-2 is used to start doing an experimental validation with SFEM by considering the adjacent free space region to one of the edges as a free space defect. The setup of the model is shown in Figure 6-3, where it will be considered that this sample as the defect is infinitely long in the *z*-direction with limited dimensions in the *xy*-plane. This will be converted to the experiment by taking a sample, where edges for coils and sample are far away from 2D cross section in addition of taking a measuring points of the normal magnetic flux density B_y that show the effect of this edge defect.

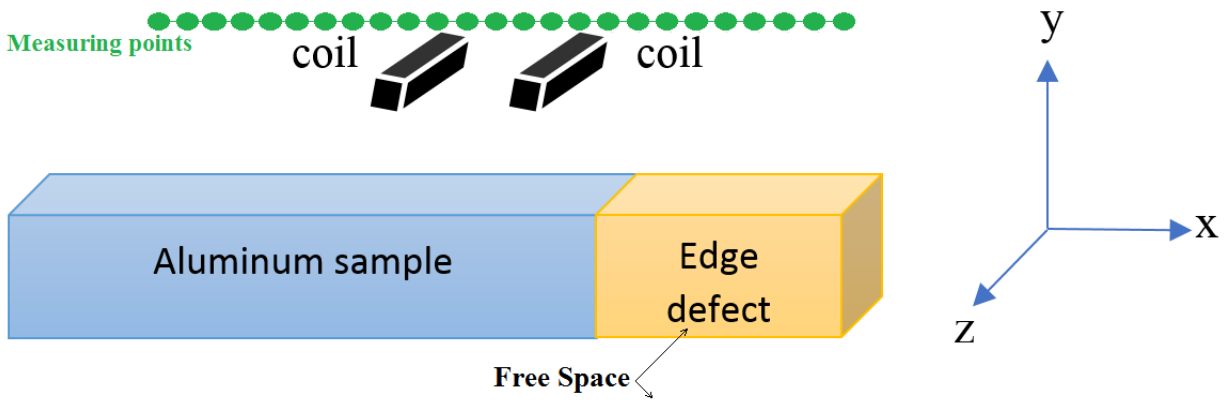

Figure 6-3 Aluminum sample with edge defect and coil positions

It is important to determine the optimal positions for these measuring points that will give the required details regarding the experiment.

To evaluate the performance of the existence of the edge defect, a line of measuring points should be allocated above the coils centered at the middle point between the coils that cover part of the sample and part of the defect. In this way, a perfect study will be done to study this defect.

An elongated coil is used to create an experimental validation according to a 2D geometry. The coil is long enough along one axis to reduce the effect from the coil edges on the fields over the center of the coil. The line of measurements is across the center of the coil as indicated in Figure 6-4a. The coil consists of 15 turns coated wire with diameter of 0.1 mm. The current flowing in the wire at 1000 Hz frequency is measured to 70 mA. The cross section of the coil is 0.5 mm^2, other dimensions in the setup are given in Figure 6-4c. The conductive sample is an Aluminum alloy T6061-T6 with a conductivity of 25 MS/m.

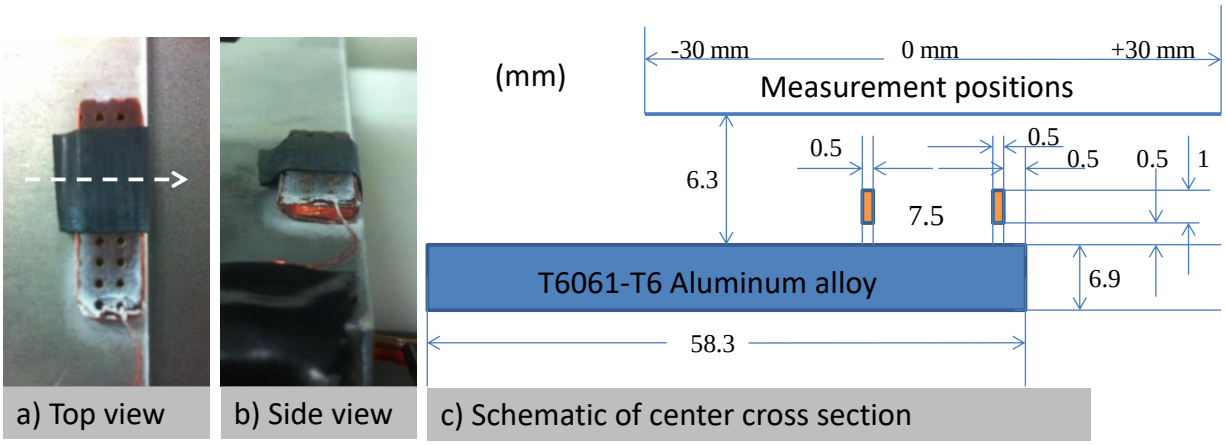

Figure 6-4 Experimental steup for testing the Aluminum sample with coils position. (a) Top view. (b) Side view. (c) Sample and coils dimensions and positions.

The coil is mounted on the sample close to the edge. The edge will introduce asymmetry of the induced currents and the magnetic field above the sample. A magnetic field sensor using a tunneling magnetoresistive (TMR) element is used to measure the component of magnetic field normal to sample top surface. The TMR sensor is mounted on a PCB with a circuit to amplify the sensor output signal. The TMR sensor is placed in the sensor fixture and scanned over the coil. The sensitivity axis is normal to the sample top surface. The setup is shown in Figure 6-5.

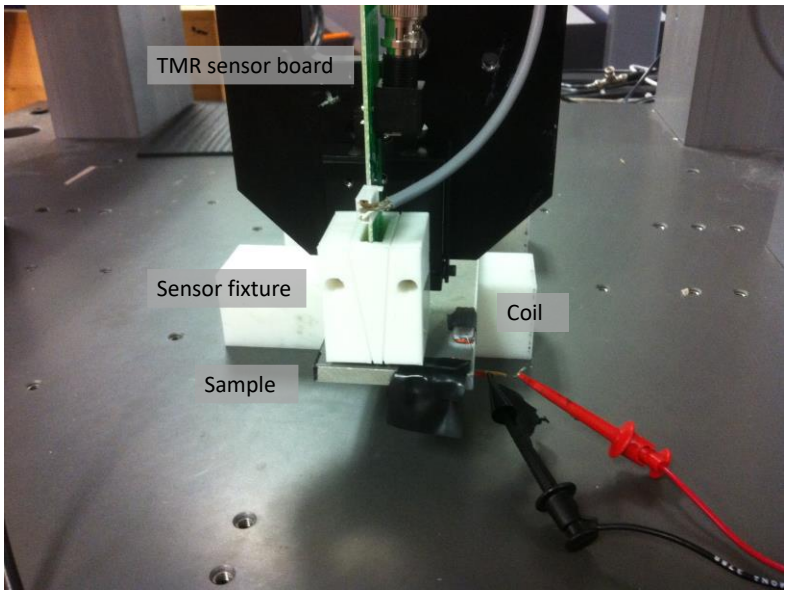

Figure 6-5 TMR sensor mounted in scanner to measure magnetic flux density at measuring points.

A sinusoidal voltage with 1000 Hz frequency is connected to the excitation coil. The overall experimental setup is shown in Figure 6-6.

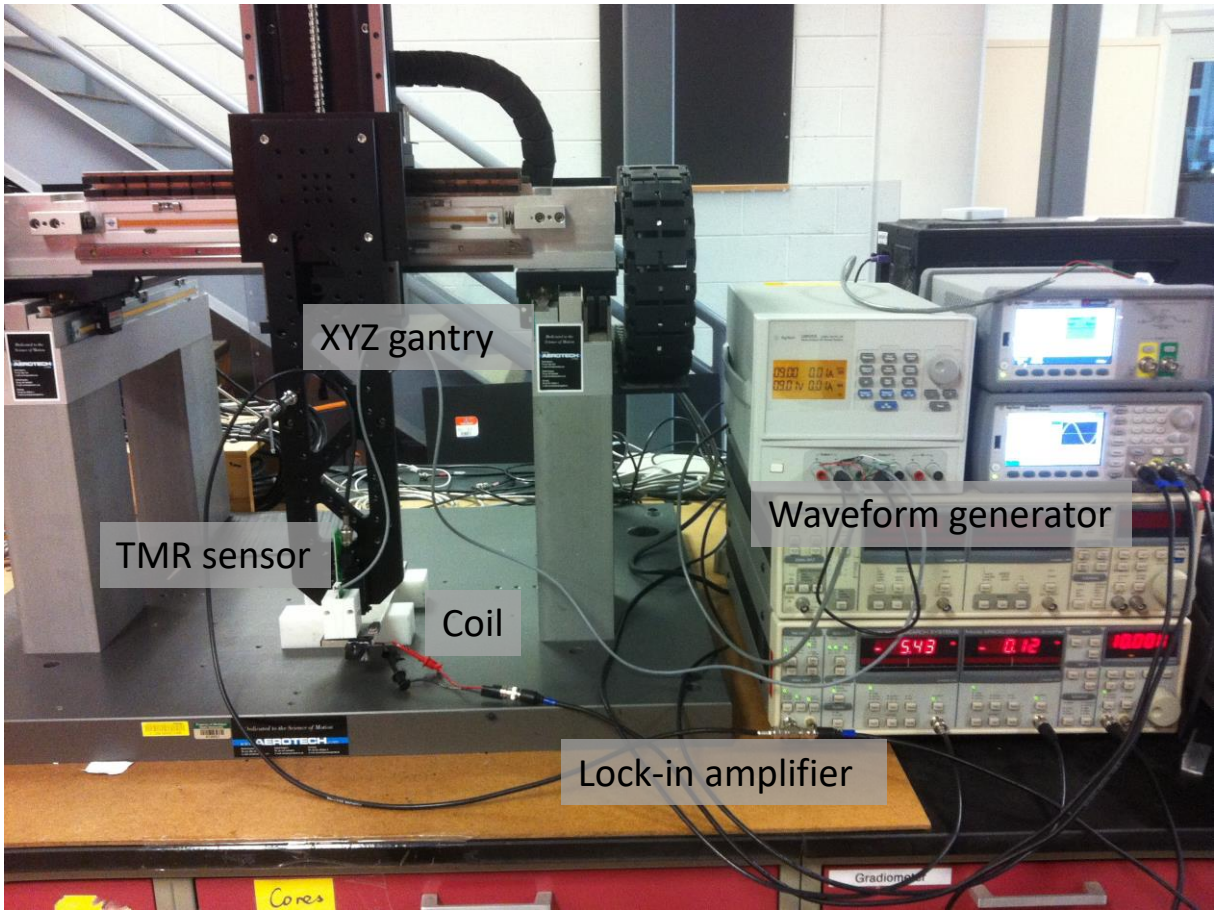

Figure 6-6 Complete experimental setup for the experiment .

A lock-in amplifier model 830 from Stanford Research Systems is used to enhance the signal output from the TMR sensor. Equation (6.1) gives the model of the input signal to lock-in amplifier:

$$V_s = K_s cos(\omega t + \varphi_s) \tag{6.1}$$

where K_s is amplitude, ω is angular frequency, φ_s is phase angle. Equation (6.2) shows reference signal, which should have the exact same angular frequency ω as the input signal and pre-specified constant amplitude K_r.

$$V_r = K_r cos(\omega t + \varphi_r) \tag{6.2}$$

These two signals are multiplied according to equation (6.3).

$$V_m = V_r \cdot V_s = \frac{1}{2} K_r K_s [cos(\varphi_s - \varphi_r) + cos(2\omega t + \varphi_r + \varphi_s)] \tag{6.3}$$

The result consists of two frequency components. If the low pass filter is set correctly, the high frequency component will be removed and the output is the baseband signal given by equation (6.4):

$$V_{out} = \frac{1}{2} K_r K_s cos(\varphi_s - \varphi_r) \tag{6.4}$$

There are two multipliers in the lock-in amplifier with reference signals shifted 90° in phase. The two outputs are given in equations (6.5) and (6.6), which are correlated to the in-phase and quadrature component of the signal respectively as,

$$V_X = \tfrac{1}{2} K_r K_s cos(\varphi_s - \varphi_r) \tag{6.5}$$

$$V_Y = \frac{1}{2} K_r K_s sin(\varphi_s - \varphi_r) \tag{6.6}$$

The reference signal to the lock-in amplifier is obtained from the excitation current, to ensure the references have the exact same frequency as the signal and that the measured in-phase and quadrature components are related to the exciting current. The schematic of the experimental setup is shown in Figure 6-7.

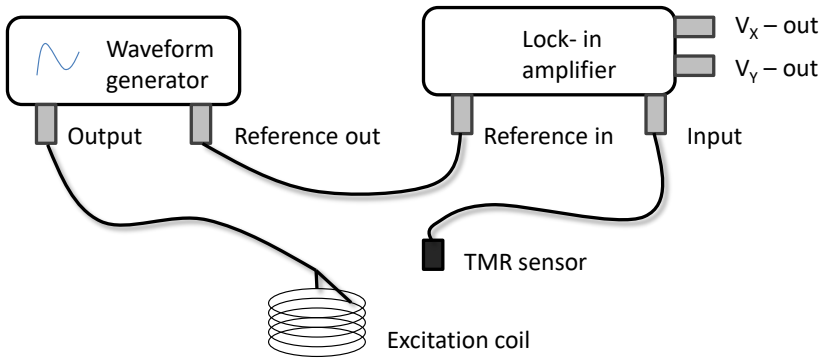

Figure 6-7 Schematic of the experimental setup shows inputs and outputs for the lock-in amplifier.

The results from scanning the TMR sensor over the center line of the excitation coil, as described in Figure 6-4, are presented in Figure 6-8. The asymmetry of the fields due to the edge of the sample is seen in the collected data which is proportional to the component of the magnetic field normal to the sample top surface (B_y). The measurements are acquired at 6.3 mm from the sample surface scanning the TMR sensor over the excitation coil.

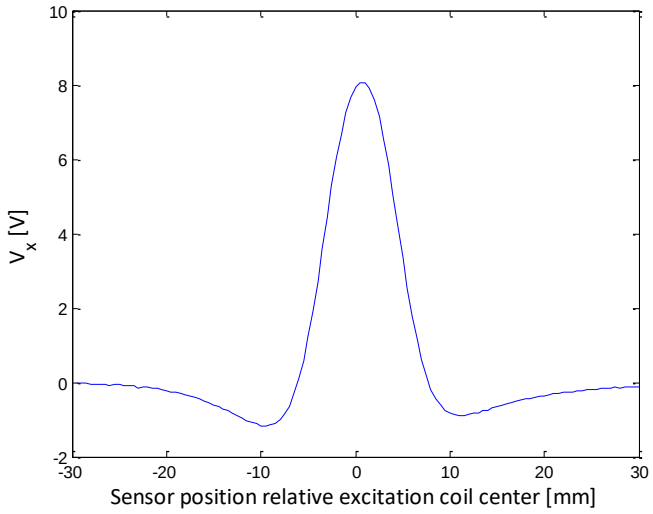

Figure 6-8 Experimental results using 1000 Hz excitation frequency

The tested values will be used then to make an analysis for the edge defect.

6.2 Edge Defect Experimental Setup for Aluminum Sample

To make an equivalent 2D computational model, the Aluminum sample will be located in a very large space, so the outer boundaries which are the Dirichlet boundary conditions will not affect the resulted potential lines. Then values of the magnetic flux densities at measuring points will not be changed too. The 2D equivalent model for the experiment is shown in Figure 6-9.

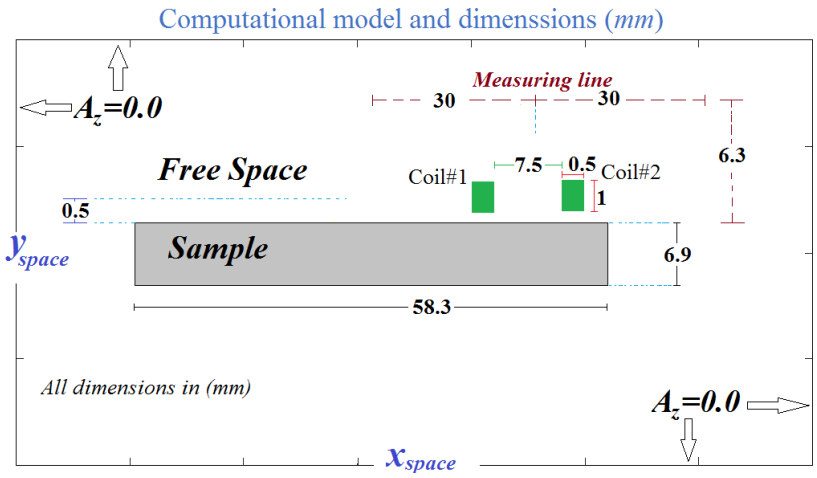

Figure 6-9 Computational model for Aluminum sample to be in SFEM and COMSOL.

The used sample in this experiment is T6061-T6 Aluminum alloy with conductivity 25 MS/m. The equivalent current densities in both coils are: $\pm 2.1\times10^{6}$ A/m^2 where all dimensions are in mm as shown in the schematic in Figure 6-4c and 6-9.

The following results are for the values of normalized magnetic flux density values at the measuring points.

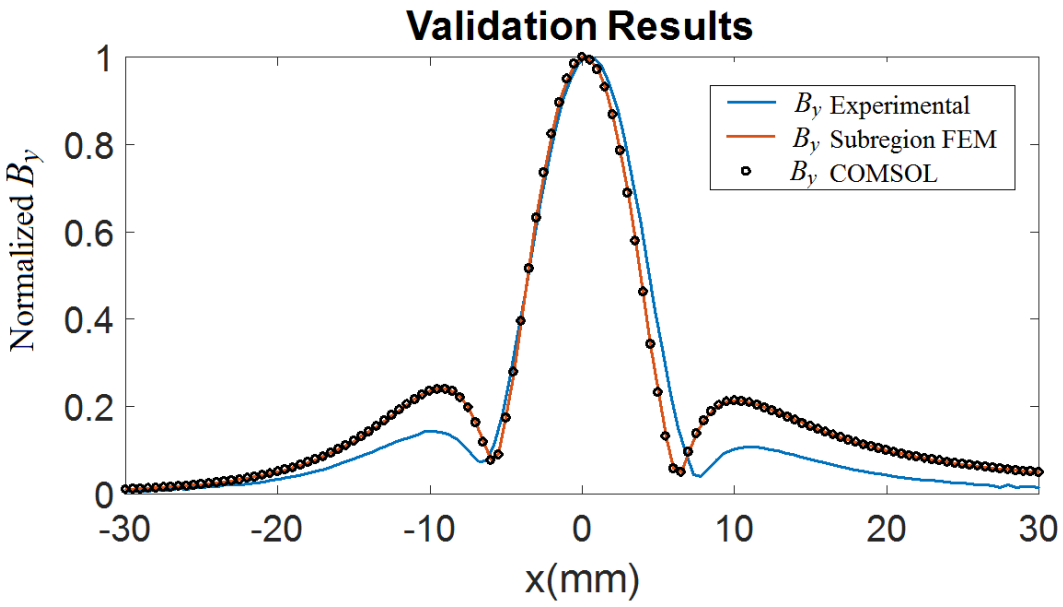

Figure 6-10 Normalized magnetic flux density values at measuring line

These results were taken when f=1kHz. Where we use COMSOL to compare the experimental with the presented SFEM solver results to validate the experimental results. Unsymmetrical shape for the values of the normalized magnetic flux densities is shown according to the defect existence for the positive values of the measuring points. These values give an indication of having a defect in this region where an excellent agreement between COMSOL and SFEM and the experimental values as shown in Figure 6-10.

6.6 Steel sample with surface defect experimental validation.

This part objective is to verify using SFEM in detecting surface defect. After that, use the same experiment setup and experimental data to characterize this defect using SFEM.

This experiment was done in the Non-Destructive Lab in Michigan State University with the same experimental setup as done for the aluminum sample. However, we replaced that aluminum sample by Mild steel plate (0.15 - 0.30% carbon and Fe) with relative permeability of 2000. The conductivity of this steel sample is found to be: 6.3×10^6 S/m. Figure 6-11 shows a top schematic

for the steel sample with defect and sample dimensions. The thickness of this sample is equal to 10 mm.

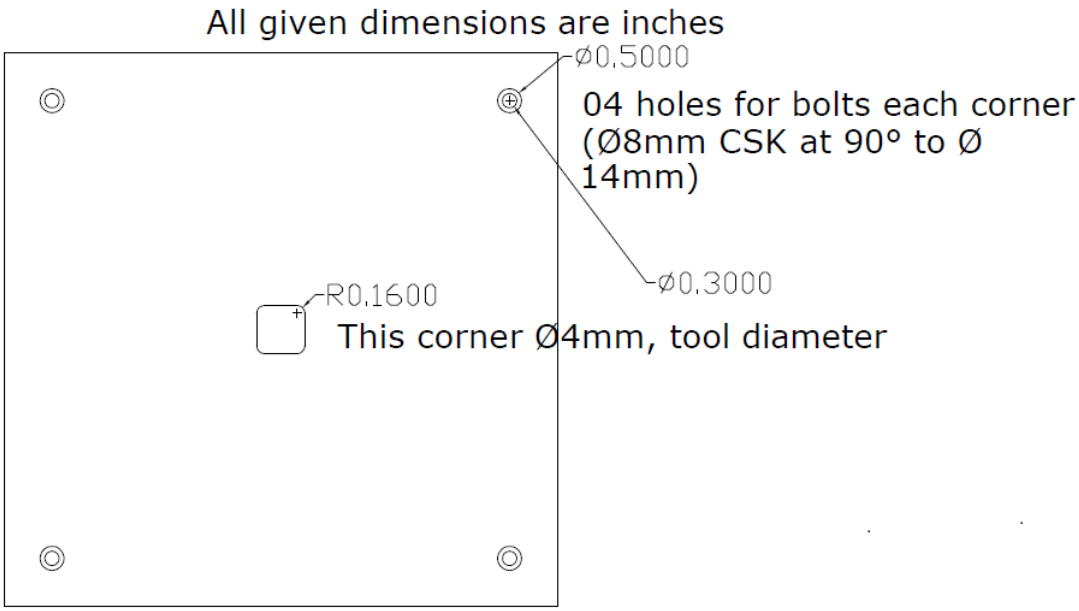

Figure 6-11 Top schematic for the steel sample with defect

Figure 6-12 shows a top view for the surface defect. The 3D dimensions for this surface defect dimensions are (cm): 2.54 ×1.27 ×0.635.

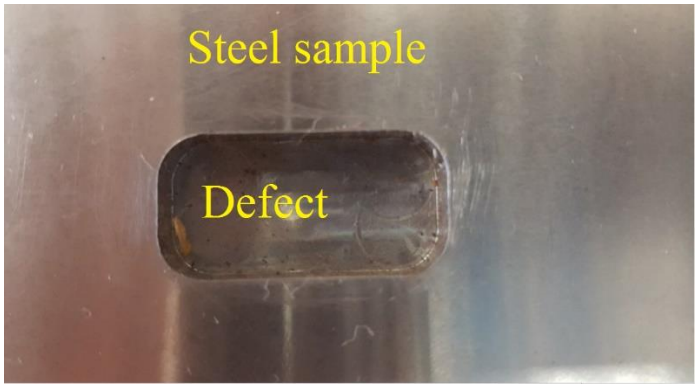

Figure 6-12 Top view for the surface defect

The steel sample was tested in the lab with lift off distance coils equal to 1.5 mm from steel surface, The center of left coil is located over the center of the defect and the distance between coils is 8 mm. We used 11000 points as our sampling points where the used frequency used was: 100Hz.

We used 50 mA current that passed through 250 turns coil with a square cross-sectional area of: 3mm×3mm. So, the resulted current density in both coils has been found as: $\frac{250\times 50}{3\times 3} = \pm 1.389\times 10^{6}$ A/m^2.

Figure 6-13 shows how this coil is fixed and mounted on the top of steel sample.

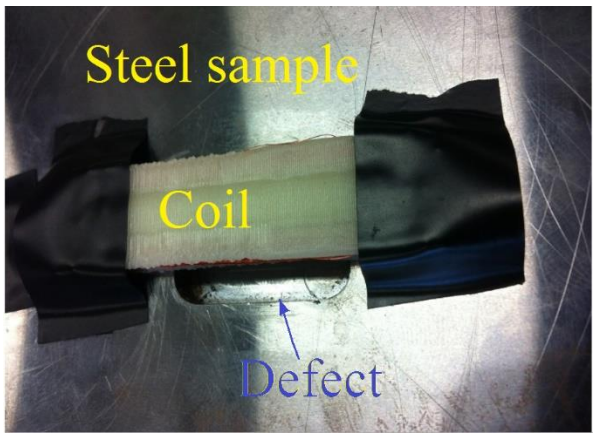

Figure 6-13 Coil position at the top of steel sample

As mentioned, we used 11000 sampling points as measuring data. In addition, the measuring line has taken on 10.6 mm above the steal surface and its length was 110mm.

A computational setup was used for both COMSOL modeling and SFEM, the following 2D setup will be used to convert the computational work to 2D.

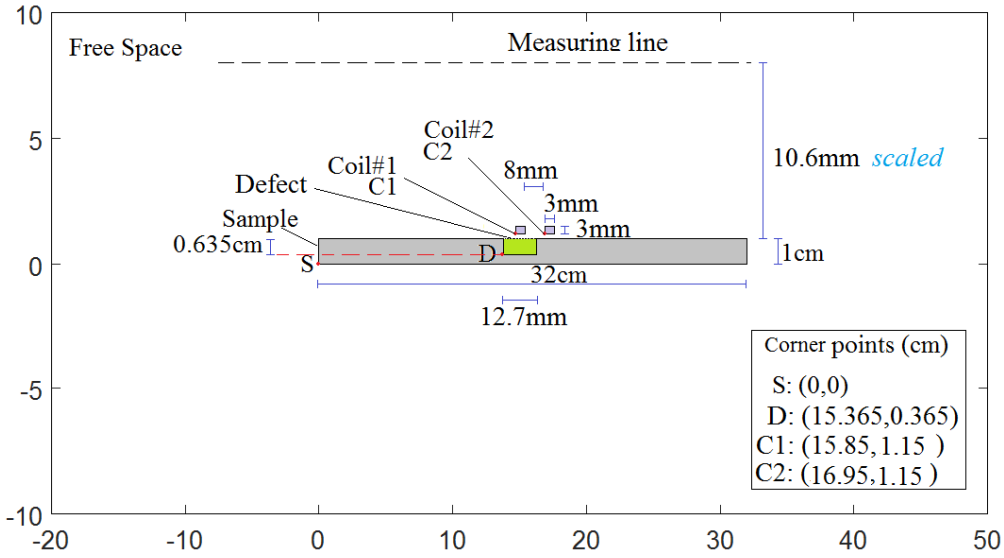

Figure 6-14 Computational model for steel sample used for simulation in SFEM

We used a measuring line between points (119.3mm,20.6mm) to (229.3mm,20.6mm). We used this measuring line to find values for normal magnetic flux density (B_y) as measuring the output voltage for the lock-in amplifier. Therefore, we can use these values in our solution. The experimental values for the real part of the output voltage is shown in Figure 6-15.

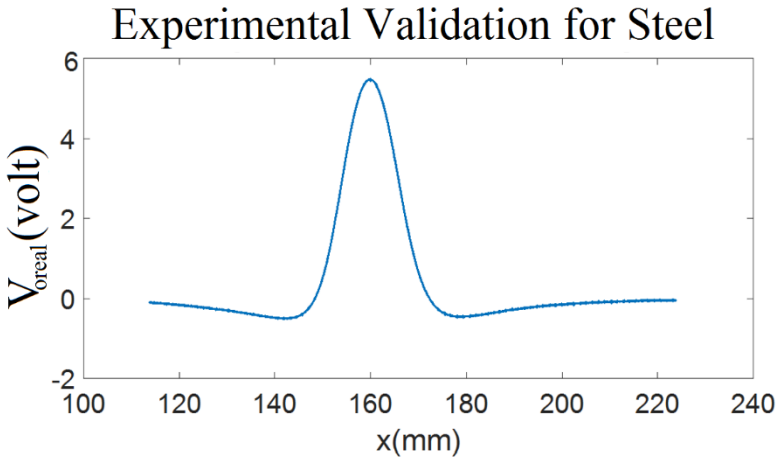

Figure 6-15 The experimental values for real part for output voltage

It is noticed from Figure 6-15 that there is very small sign for asymmetry due to the defect. The maximum values for the magnetic flux density will be at the center between the coils. This small

intangible asymmetry is due to low values for skin depth according to the high values of the permeability and conductivity for the used steel sample. This will make this defect too hard to be detected in the given parameters. In addition, we noticed some noise added to these data. The source for noise is due to using low pass filter in the experiment and to surface roughness and sample microstructure.

A parametric study by varying both conductivity σ and permeability μ_r for the steel sample is presented in Figure 6-16.

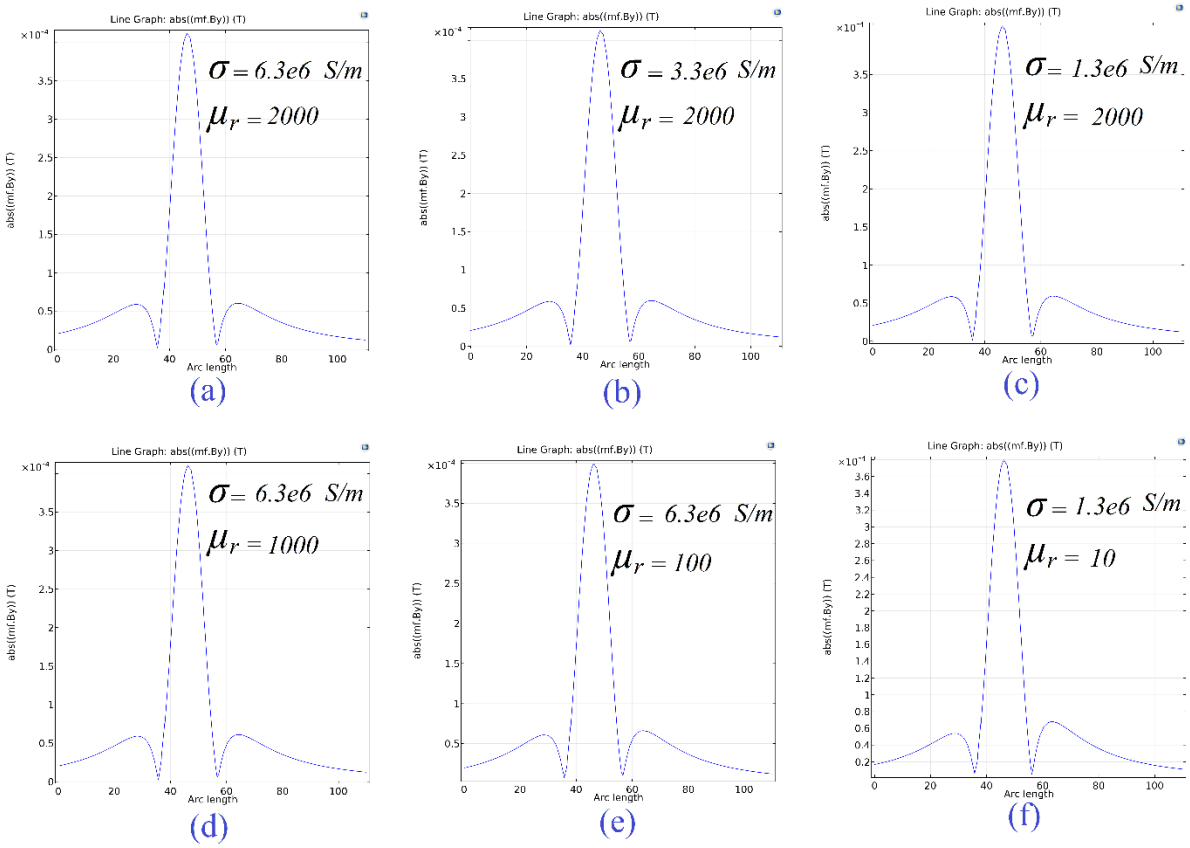

Figure 6-16 Parametric study for absolute values for the normal magnetic flux density values at the measuring points

Decreasing these values and running the simulation for testing the steel sample using COMSOL will give us more asymmetrical shape for the output signal which is representing the absolute for normal magnetic flux density at the measuring points.

Figure 6-17 shows a comparison between COMSOL, SFEM and experimental results. Finding the normalized values for normal magnetic flux density (B_y) will give an indication for both the validation and detecting the defect.

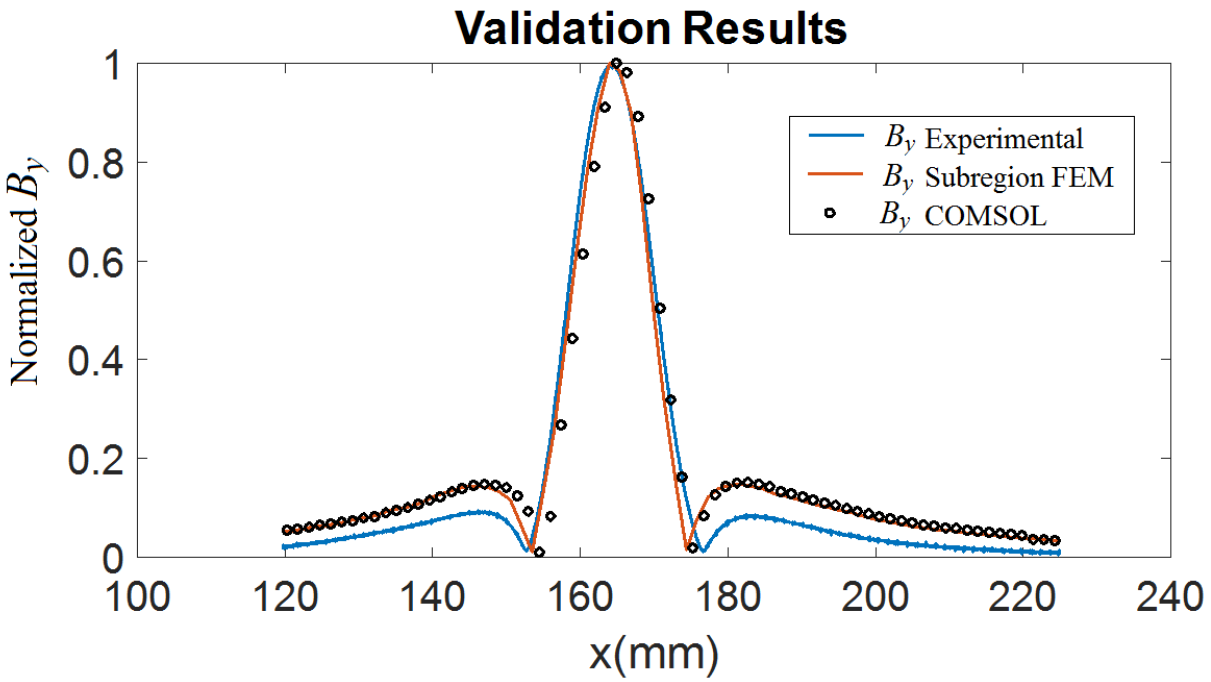

Figure 6-17 Normalized magnetic flux density values at measuring line

The results in Figure 6-17 shows an excellent matching between the normalized values of the magnetic flux density at the measuring points.

According to multiple factors like the existing of low pass filters and due to electrical circuits components used in the experimental setup, there may be phase shift between the experimental

and FEM values in addition to scaling. This shift may affect the results if we are taking the real part of the magnetic flux density. To solve this, we took the absolute values for magnetic flux density values. It is also noticed that there is some noise in the experimental results. The source of noise may be electrical or due the roughness of the steel surface. In addition, it may be resulted from the molecular construction for the steel in addition to noise that resulted from using low pass amplifier in the experiment itself.

6.7 Subsurface Aluminum Defect

In order to characterize hidden defect, we will study subsurface defect in Aluminum sample (T6061-T6). In this study, we will be able to validate our presented SFEM algorithm in this thesis, where an initial validation was done in section 6.2 for a healthy sample with edge defect. The setup shown in Figure 6-18 will be used for experimental validation.

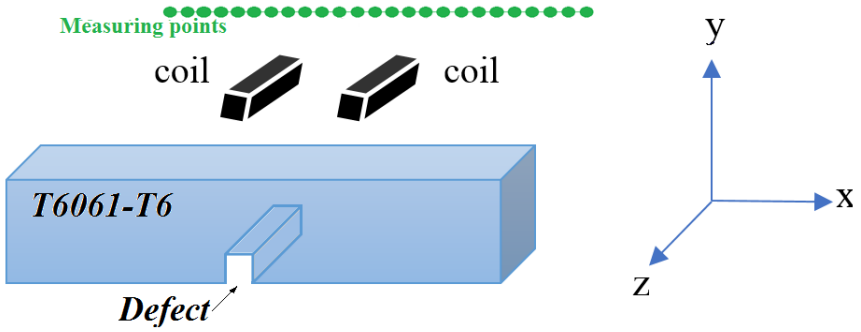

Figure 6-18 Aluminum sample and coils position for subsurface defect

It will be considered that this sample as the defect is infinitely long in the *z*-direction with limited dimensions in the *xy*-plane. This will be converted to the experiment by taking large sample with respect to the coils in addition of taking a measuring points of the normal magnetic flux density B_y that show the effect of this internal defect.

To evaluate the performance of the existence of this subsurface defect, a line of measuring points should be allocated above the coils. In this way, a perfect study will be done to study this defect.

An elongated coil is used to create an experimental validation according to a 2D geometry. The coil is long enough along one axis to reduce the effect from the coil edges on the fields over the center of the coil. The line of measurements is across the center of the coil as indicated in Figure 6-19.

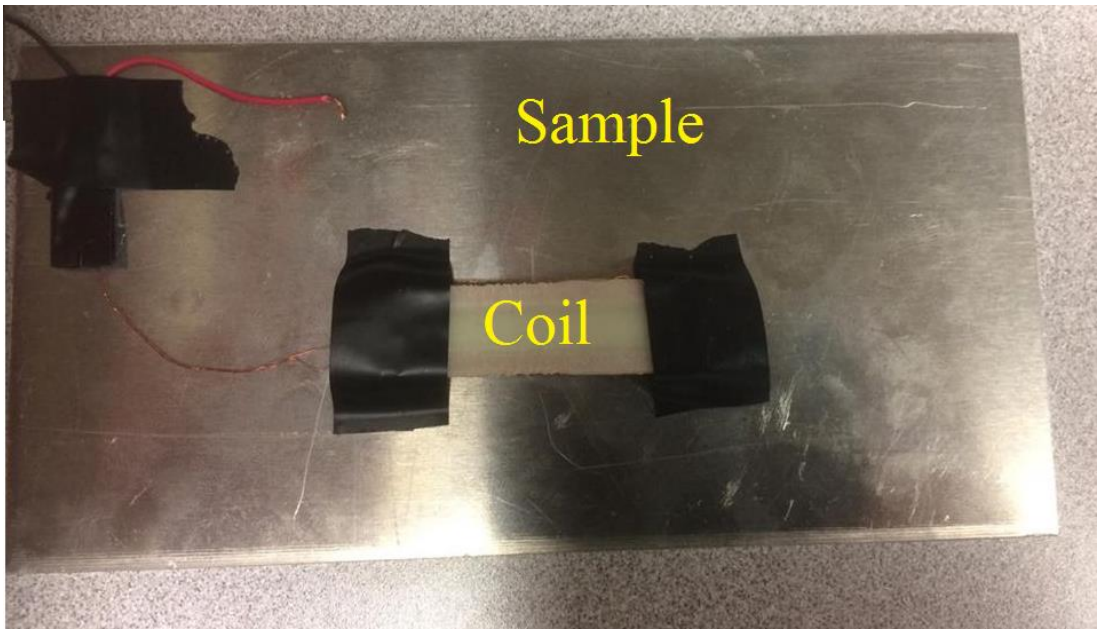

Figure 6-19 Top view for the aluminum sample with the coils

The sample was tested in the NDE lab with lift off distance coils equal to 1.5 mm from aluminum surface, where the center of left coil is located over the defect and distance between coils is 8 mm. We used 12000 points as sampling points where we tested the sample at multiple frequencies; 10Hz, 100Hz and 1kHz.

We used 50 mA current that passed through 250 turns coil with a square cross-sectional area of: 3mm×3mm. Therefore, the resulted current density in both coils will be: $\frac{250\times 50}{3\times 3} = \pm\ 1.389\times 10^{6}$ A/m^2. The conductive sample is an Aluminum alloy T6061-T6 with a conductivity of 25 MS/m.

Figure 6-20 shows the bottom view for the sample with defect.

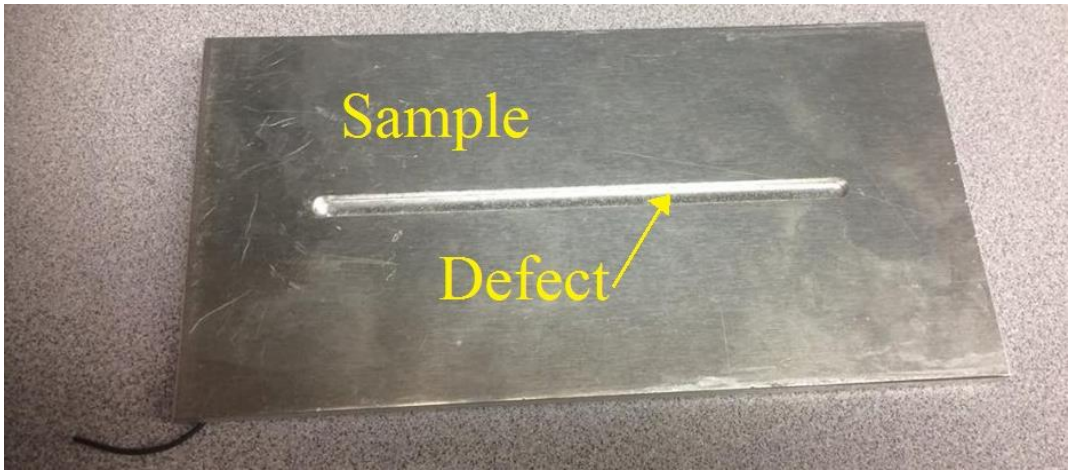

Figure 6-20 Bottom view shows the subsurface defect in the aluminum sample

The measuring line has been taken on 9.2 mm above the aluminum surface and its length was 120mm.

A computational setup has been used for both COMSOL modeling and SFEM, the following 2D setup in Figure 6-21 will be used to convert the computational work to 2D.

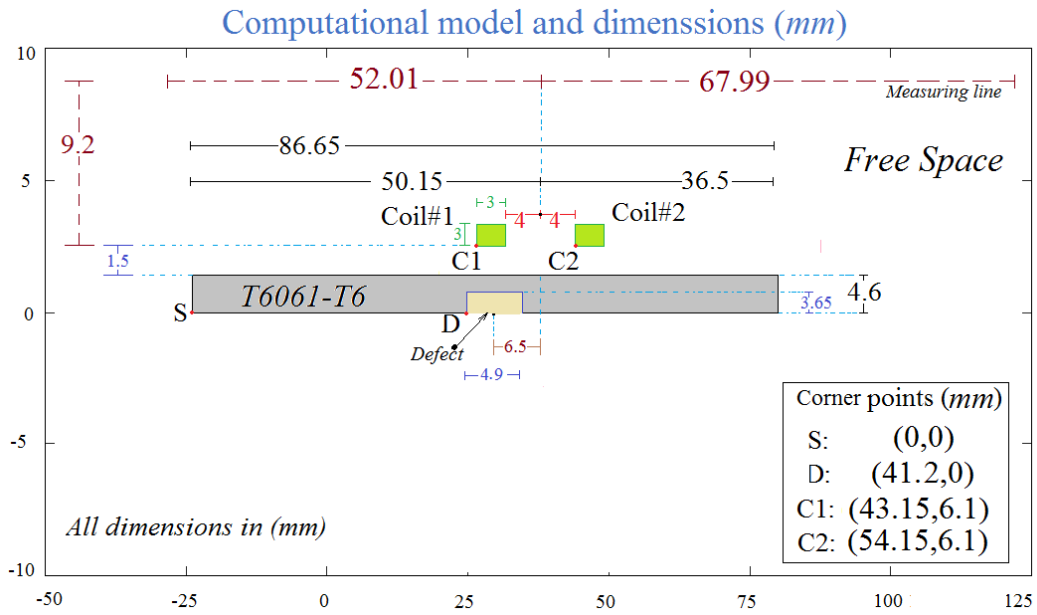

Figure 6-21 Computational model for aluminum sample used for simulation in SFEM

We used a measuring line between points (-1.66mm,13.8mm) to (118.34mm,13.8m). We used this measuring line to find values for normal magnetic flux density (B_y) as absolute, real and imaginary values, so we can use these values in our solution. The experimental values for the output of the lock-in amplifier V_y at 10 Hz, 100 Hz and 1kHz are shown in Figure 6-22.

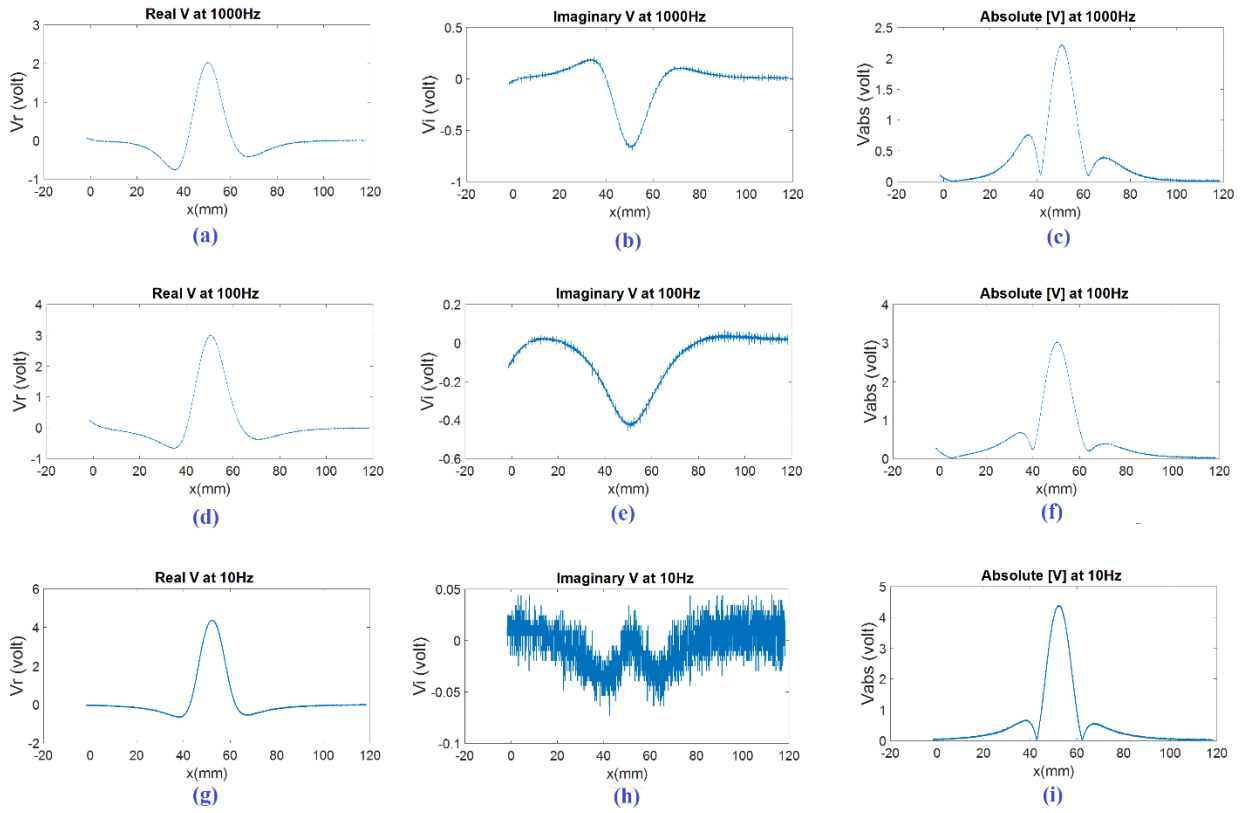

Figure 6-22 Experimental results for V_y (volt) at measuring line. (a) Real values at 1 kHz. (b) Imaginary values at 1 kHz. (c) Absolute values at 1 kHz. (d) Real values at 100 Hz. (e) Imaginary values at 100 Hz. (f) Absolute values at 100 Hz (g) Real values at 10 Hz. (h) Imaginary values at 10 Hz. (i) Absolute values at 10 Hz.

These values are representing real, imaginary and absolute values of magnetic flux density values. The left coil is positioned directly over the defect, while the right coil is positioned over the sample. This can be shown clearly from the values of magnetic flux density values at the measuring points.

Unsymmetrical shapes for the values of the magnetic flux densities is shown according to the defect existence. These values give an indication of having a defect in this region. This can be clear in shapes for real and absolute V_y at 1kHz. Where the unsymmetrical trend decreases by decreasing the frequency to 100Hz, and finally to 10Hz. This is due to skin depth that increases by decreasing the frequency; (3.1839 mm at 1kHz, 10.0684 mm at 100 Hz and 31.8391 at 10 Hz).

The output measured voltages are not clear due noise. There are a lot of resources of noise in ECT experimental systems, some of them due to [139] : lift off distances for coils, temperature variation, changes in electromagnetic properties of the material and the variation in testing speed.

As a solution for this problem, we input the experimental output signal to a moving average low pass filter to reduce the effect of noise as shown in Figure 6-23.

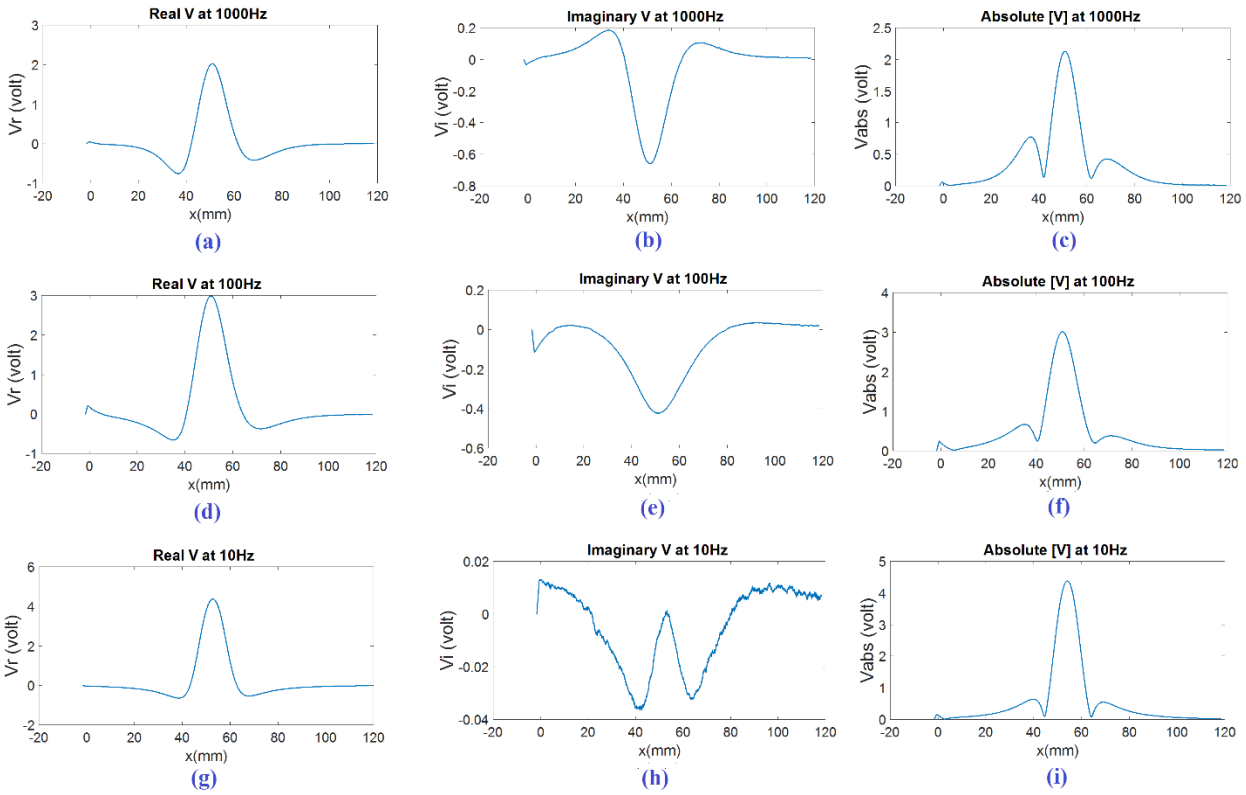

Figure 6-23 Filtered experimental results for V_y at measuring line. (a) Real values at 1 kHz. (b) Imaginary values at 1 kHz. (c) Absolute values at 1 kHz. (d) Real values at 100 Hz. (e) Imaginary values at 100 Hz. (f) Absolute values at 100 Hz (g) Real values at 10 Hz. (h) Imaginary values at 10 Hz. (i) Absolute values at 10 Hz.

It is noticed that imaginary part contribution in total magnetic flux density is very small compared to real part; about 1% of V_y. So, this will not be used in our updated values to reconstruct the defect.

It is still clear that there is asymmetry in real and absolute shapes for V_y which gives us an initial sign to start characterizing the defect since we are able now to detect it.

The following results are for the values of normalized magnetic flux density values B_y (T) at the measuring points.

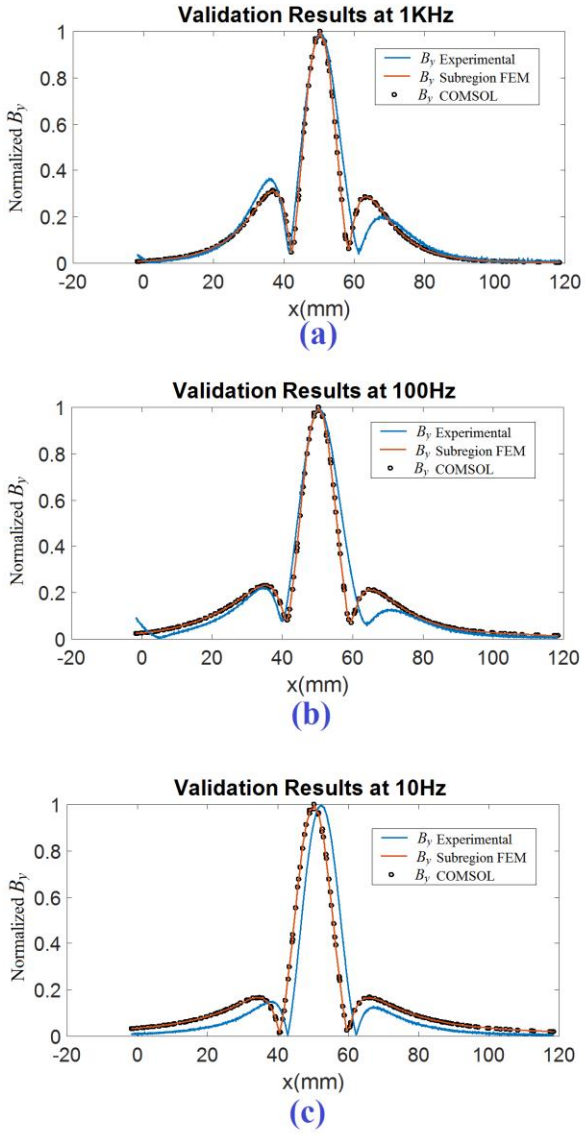

Figure 6-24 Normalized magnetic flux density B_y values at measuring line at : (a) 1 kHz. (b) 100 Hz. (c) 10 Hz.

These results were taken at f=1kHz, 100Hz and 10Hz . Where we use COMSOL to compare the experimental with the presented SFEM results to validate the experimental results. Unsymmetrical

shape for the values of the normalized magnetic flux densities has been noticed according to defect existence. These values give an indication of having a defect in this region where an excellent agreement between COMSOL, SFEM and experimental values as shown in Figure 6-24.

In order to see whether the experimental values are in phase with SFEM, we will plot the imaginary part vs. real part of B_y at all given tested frequencies as shown in Figure 6-25.

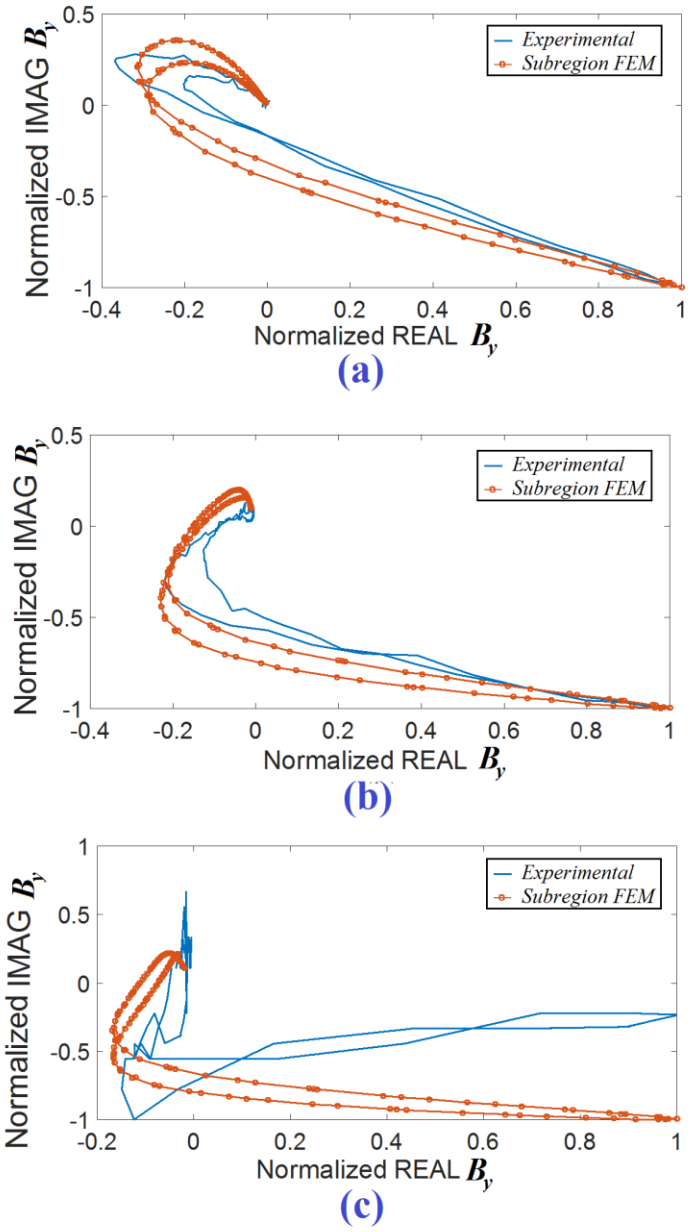

Figure 6-25 Real vs. imaginary values for the normalized magnetic flux density at measuring points at (a) 1 kHz (b) 100 Hz (c) 10 Hz

We notice that a good phase matching occurs at 1 kHz and 100 Hz, where there is small phase shift at 10 Hz. This phase shift can be easily solved by rotating the experimental results by the phase difference toward the Subregion results.

To characterize the defect, we will select the experimental results at 1 kHz for the following reasons: 1- increasing the frequency is proportional to input signal strength. That means more accurate results. 2- Skin depth is smaller (3.1839 mm). This means that all eddy current will flow in the sample and defect will have more chances to be detected. 3- For the previous two reasons and by refereeing to Figure 6-24 it is clear that asymmetrical behavior is clear at 1 kHz, that means more chances to detect the defect and the defect contribution on the magnetic flux density values at measuring points will be the maximum.

According to inverse solution for SFEM in ECT problems, defect should be detected first and an initial location should be assigned for the defect.

By testing the sample that contains the defect we find the values of the magnetic flux density values at the measurement plan, which has a lift off distance of 9.2 mm from sample surface. Plotting V_y at this plan can give us an indication for the defect location as shown in Figure 6.26.

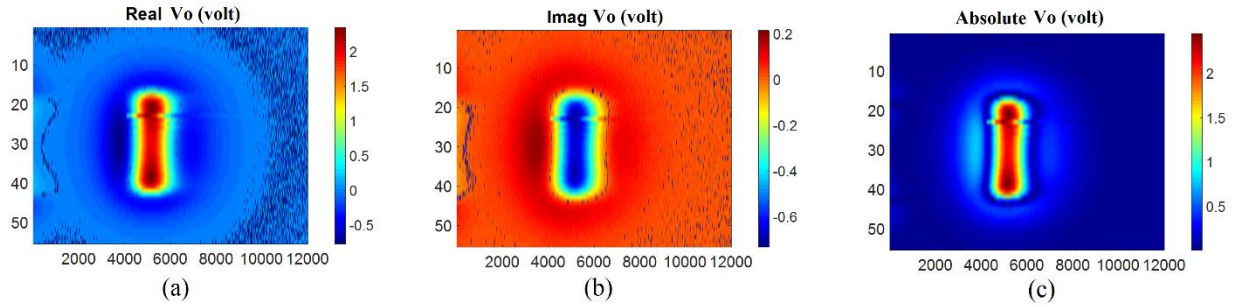

Figure 6-26 Experimental voltage values at the surface for the sample including the coils. (a) Real values. (b) Imaginary values. (c) Absolute values.

Figure 6-26 shows real, imaginary and absolute values of output voltage on the measurement plan. The location of the coils is clean where the defect can be assigned at the left of the left coil as shown in Figure 6-26c.

On each node on the defect, the vertical displacements are selected as design parameters. In our numerical model we have 8 geometric parameters as used in [115, 116] contained in vector $\{h\}$:{ $h_1, h_2, h_3, h_4, h_5, h_6, h_7, h_8$}. To start our solution, we will assign two regions, one for the defect as R_2 , where other one will be the reminder region R_1. Next, our design parameters will be identified inside R_2. Those design parameters should be on the surface of our predetermined defect as in Figure 5-18. Each design variable is represented by 10 bits to be used later in Genetic Algorithm. For testing, as was done for the original defect, the following fixed design parameters (mm) nodes coordinates as shown in Figure 6-25 will represent the original defect:

$$\{(4.12,0),(4.283,0),(4.446,0),(4.61,0),(4.61,0.365),(4.446,0.365),(4.283,0.365),(4.12,0.365)\}$$

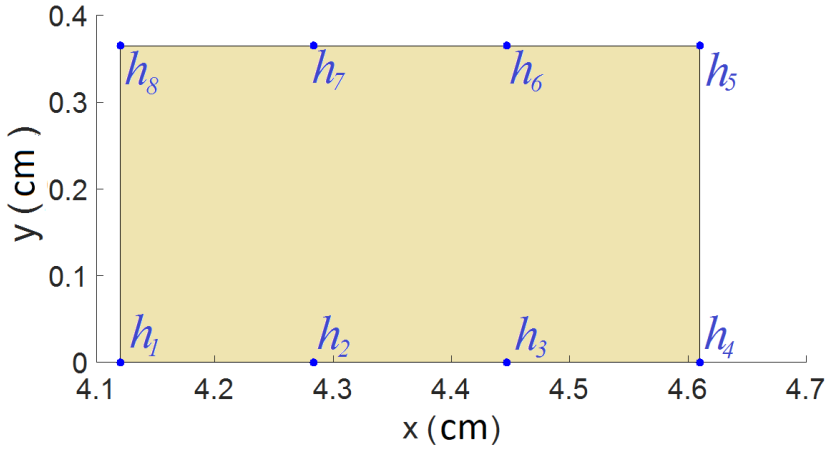

Figure 6-27 Original defect that is used for testing with the design parameters.

Starting from these points, $\{h\}$ will be calculated each iteration to find the original defect shape as we chose the *y*-directions of these design parameters as: $\{h\}$= {0, 0, 0, 0, 0.365, 0.365, 0.365, 0.365, } cm and computed the field $B^i_{Measured}$ at the measuring points.

These design parameters will be treated as our design nodes in our method of solution. An initial defect shape will be generated with saving node numbering as done for the first times of these

designing nodes. After that SFEM will be used to change the positions for these nodes until getting our solution which will be the most accurate defect shape and the reconstructed $\{h\}$ will be generated each iteration to match the measurements $B^i_{Measured}$.

In order to find the best $B^i_{Measured}$ values, we will need to multiply the experimental voltage values V_y by factor $K_{norm,}$ where $K_{norm,}$can be found found as:

$$K_{norm} = \frac{Max\{B_{y\_subFEM}\} - min\{B_{y\_subFEM}\}}{Max\{V_{y\_Exp}\} - min\{V_{y\_Exp}\}} \quad (6.7)$$

In our simulation and comparing values, we used the real part of magnetic flux density at measuring points. Where, we used multiple sets of measuring points along the sample and we chose a set of measuring points located between the coils as: *x* (mm)located at: {40, 42.22, 44.44, 46.66, 48.88, 51.11, 53.33, 55.55, 57.77, 60} and *y*=13.8 mm.

After determining the defect region and name it as R_2, then the remainder area will be considered as a fixed region with fixed nodes and elements and this will be R_1 as shown in Figure 5-25.

The next step will be to pick and determine the groups of nodes for each selected region. Each region should have two sets of nodes; interior and exterior nodes as mentioned before. At least one set of exterior nodes should be common between both regions for applying subregion method.

For the reminder region; the bigger one R_1, will consists of two sets of the exterior nodes (Group 1 and Group 2) where the exterior nodes in Group 1 of nodes will be at the interface between both of R_1 and R_2. Those are the common nodes between both regions. Those nodes will be used in equation (3.19) in simulation SFEM as the interfacing exterior nodes between both regions. Nodes that belong to Group 2 are also considered to be exterior nodes for R_1. Those are the boundary nodes and their values are upon the given data. In our example, zero potential values are imposed for these nodes.

The reminder nodes within region R_1 ,which are not belong to both Groups 1 and 2 will be saved as the interior nodes for R_1 and will be used in equation (3.6) in Subregion simulation. Our SFEM solver is designed to determine both interior and exterior nodes for R_2 where nodes belong to Group 1 are exterior nodes for R_2. This is the common set of nodes in R_1. While reminder nodes inside R_2 are considered the interior nodes for R_2.

After selecting nodes for both regions, a sub-regional Finite Element solution will be implemented for both regions. The important issue will be in creating two profiles for both regions. Then saving results in these two profiles to be used later in the inverse part to detect the shape of the defect. The profile that contains the resulted data of R_1 will be fixed and created only one time. While continuously updating data in the profile that is related to R_2. This is because SFEM will continue among the given iterations until achieving the optimal solution which is the best score function value. That means the best reconstructed shape of the hidden defect which happened at minimum value of F in equation (3.5). To update the data for R_2, new meshing scheme will be generated every iteration. The only things that have changed is be nodes position and their resulted vector potential values, Changing the position of the interior nodes in R_2 means that a resulted change on the predetermined design parameters and the magnetic flux density is then calculated $B^i_{Calculated}$ along the measuring line. The object function F is evaluated by comparing $B^i_{Calculated}$ with $B^i_{Measured}$ by using equation (5.2).

$$F\left(\{x_1, y_1\}, \{x_2, y_2\}, \cdots, \{x_n, y_n\}\right) = \sum_{i=1}^{measuring\ points} \left(B^i_{Calculated} - B^i_{Measured}\right)^2 \qquad (5.2)$$

It is necessary to impose constraints to get a single defect [115, 116]. So, to maintain a realistic shape with a single defect, node 8 on top of node 1 and node 7 on top of node 2 and node 6 on top of node 3 as shown later in Figure 5-18, where 8 nodes are used as designing nodes and by

imposing the constraints as $h_8 > h_1$, $h_7 > h_2$, $h_6 > h_3$ and $h_5 > h_4$: Therefore single and realistic defect will be created

In our simulation, Genetic Algorithm [115, 116] is used as optimization technique to calculate fitness score function each iteration. This optimization technique will be used to calculate best fitness score value. To apply this optimization technique in our proposed method, the object function F is calculated at each iteration. After that, new meshes inside the defect region R_2 will be generated using elastic meshing and then get new defect shape each iteration until having the best defect shape. Next, evaluate the performance of the complete system by calculating F. Figure 5-26b shew the block diagram of Genetic Algorithm optimization technique used in this SFEM solution. This GA block diagram can be plugged in the main SFEM flow chart in Figure 5-19 for optimization and calculating F each iteration.

Several simulations of defect characterization problem have been running and the results were tabulated. The best fitness score using Genetic Algorithm was achieved when the population size is 100 for the 50 iterations as shown in Table 6-1.

The verification of Genetic Algorithm is achieved by increasing both iteration numbers and populations size which means better values and being closer to the optimal solution of the fitness score in equation (5.2).

Table 6-1 Fitness scores and processing time using GA for different iteration numbers.

Population size	**10 iterations**	**20 iterations**	**30 iterations**	**40 iterations**	**50 iterations**
20	0.0784	0.0645	0.0331	0.0173	0.0139
40	0.0524	0.0408	0.0317	0.0169	0.0122
60	0.0338	0.0314	0.0272	0.016	0.0108
80	0.0374	0.0259	0.0152	0.0134	0.0073
100	0.0124	0.0114	0.0071	0.0069	0.0047

It is clear that increasing number of iterations will make solution closer to optimal value. In addition, this will increase processing time. Our objective in this thesis is to get an accurate shape for the hidden defect so we can study its effect on the entire system. This is clear from fitness score values per each case using Genetic Algorithm. In our solution, Genetic Algorithm needs computational time in processing since it takes three steps in determining the next population which are: selection, crossover and mutation. It is binary coded algorithm; it takes time to convert to real numbering system in our computational solution.

To measure the accuracy of the reconstructed defect, the length from the centroid of the true profile to each point was calculated using equation (5.8).

$$e = \frac{\sum_{i=1}^{n} \left(\frac{r_{true}^{i} - r_{reconstructed}^{i}}{r_{true}^{i}} \right)}{n} \tag{5.8}$$

where r_{true}^{i} is length from the centroid to the true profile, and $r_{reconstructed}^{i}$ is the length from the centroid to the reconstructed profile, where n is the number of coordinates in the profile.

Three different examples are taken to find r_{true}^{i} as shown in following results in Tables 6-2, 6-3 and 6-4.

Table 6-2 Calculating defect reconstruction accuracy for example one (cm).

True Defect Centroid		**True Defect Profile**			**Reconstructed Defect Profile**			$\left(\frac{r_{true}^{i} - r_{reconstructed}^{i}}{r_{true}^{i}} \right)$
x	y	x	y	r_{true}^{i}	x	y	$r_{reconstructed}^{i}$	
4.365	0.1825	4.12	0	0.3055	4.12	0.1025	0.2577	0.1563
4.365	0.1825	4.283	0	0.1999	4.283	0.0254	0.1770	0.1144
4.365	0.1825	4.446	0	0.1999	4.446	-0.2427	0.4329	1.1655
4.365	0.1825	4.61	0	0.3055	4.61	0.2158	0.2472	0.1906
4.365	0.1825	4.61	0.365	0.3055	4.61	0.3419	0.2922	0.0432
4.365	0.1825	4.446	0.365	0.1999	4.446	0.4401	0.2702	0.3515
4.365	0.1825	4.283	0.365	0.1999	4.283	0.3113	0.1525	0.2372
4.365	0.1825	4.12	0.365	0.3055	4.12	0.429	0.3475	0.1376

The reconstructed defect in Table 6-2 gives error= 29.96% with an average reconstruction efficiency = 70.04%

Table 6-3 Calculating defect reconstruction accuracy for example two (cm).

True Defect Centroid		**True Defect Profile**			**Reconstructed Defect Profile**			$\left(\frac{r^i_{true} - r^i_{reconstructed}}{r^i_{true}}\right)$
x	y	x	y	r^i_{true}	x	y	$r^i_{reconstructed}$	
4.365	0.1825	4.12	0	0.3055	4.12	0.2706	0.2603	0.1477
4.365	0.1825	4.283	0	0.1999	4.283	-0.1350	0.3278	0.6396
4.365	0.1825	4.446	0	0.1999	4.446	-0.0492	0.2456	0.2287
4.365	0.1825	4.61	0	0.3055	4.61	0.0124	0.2982	0.0237
4.365	0.1825	4.61	0.365	0.3055	4.61	0.3221	0.2819	0.0769
4.365	0.1825	4.446	0.365	0.1999	4.446	0.4802	0.3086	0.5439
4.365	0.1825	4.283	0.365	0.1999	4.283	0.3218	0.1614	0.1923
4.365	0.1825	4.12	0.365	0.3055	4.12	0.4410	0.3561	0.1658

The reconstructed defect in Table 6-3 gives error= 25.23% with an average reconstruction efficiency = 74.77%

Table 6-4 Calculating defect reconstruction accuracy for example three (cm).

True Defect Centroid		**True Defect Profile**			**Reconstructed Defect Profile**			$\left(\frac{r^i_{true} - r^i_{reconstructed}}{r^i_{true}}\right)$
x	y	x	y	r^i_{true}	x	y	$r^i_{reconstructed}$	
4.365	0.1825	4.12	0	0.3055	4.12	0.2038	0.2459	0.19501
4.365	0.1825	4.283	0	0.1999	4.283	0.1810	0.0816	0.5914
4.365	0.1825	4.446	0	0.1999	4.446	-0.1433	0.3358	0.6799
4.365	0.1825	4.61	0	0.3055	4.61	-0.0254	0.3213	0.0517
4.365	0.1825	4.61	0.365	0.3055	4.61	0.4519	0.3641	0.1919
4.365	0.1825	4.446	0.365	0.1999	4.446	0.2880	0.1334	0.3327
4.365	0.1825	4.283	0.365	0.1999	4.283	0.4171	0.2484	0.2424
4.365	0.1825	4.12	0.365	0.3055	4.12	0.3473	0.2952	0.0334

The reconstructed defect in Table 6-4 gives error= 28.98% with an average reconstruction efficiency = 71.02%.

Figure 6-28 shows the reconstructed and original defect diagrams for the previous three cases in Tables 6-2, 6-3 and 6-4.

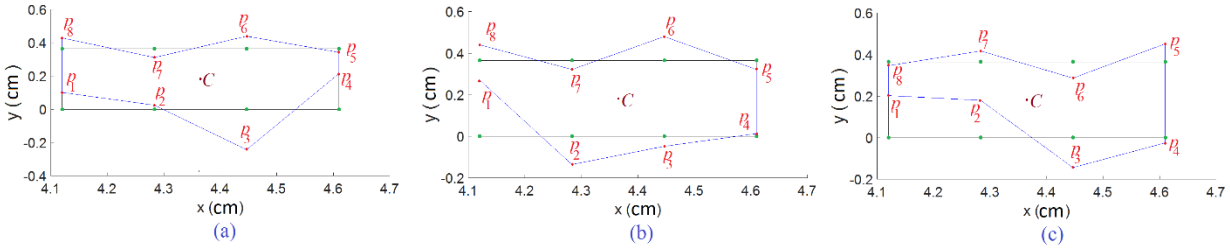

Figure 6-28 Reconstructed vs. original defect shapes. (a) Case one. (b) Case two. (c) Case three.

Where the reconstructed defect designing nodes p_i are the results of the optimization solution and are found in Tables 6-2, 6-3 and 6-4.

The best solution with average reconstruction efficiency equal to 74.77% is shown in Figure 6-28b.

We can now run our forward problem with these reconstructed defect design parameters to plot the magnetic vector potential lines as shown in Figure 6-29.

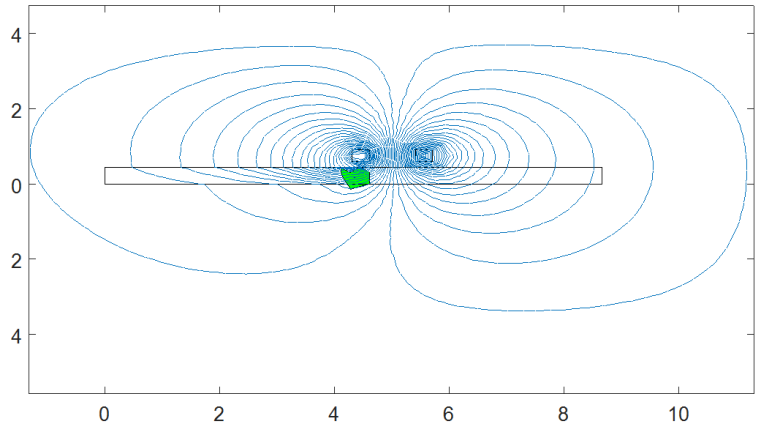

Figure 6-29 Magnetic vector potential lines distribution for the reconstructed defect.

This potential plot in Figure 6-29 can show us the effect of the subsurface defect on these vector potential lines. A lot of factors control the reconstruction of the defects as will be shown in the next chapter.

The reconstructed defect shows that it may extended over the sample which is computationally true but not representing a real defect. The shape of the defect is related to the constrains that we used in addition of the subregion area that we chose for the defect. We chose reliable defect region that is relatively large and not enclosed within the sample (1.5 mm above the upper surface of the sample and 4.6 mm bellow the sample lower surface along the sample). Figure 6-30 shows a reliable defect with limited number of elements to show how defect can be reconstructed within the sample and the resultant magnetic vector potential lines.

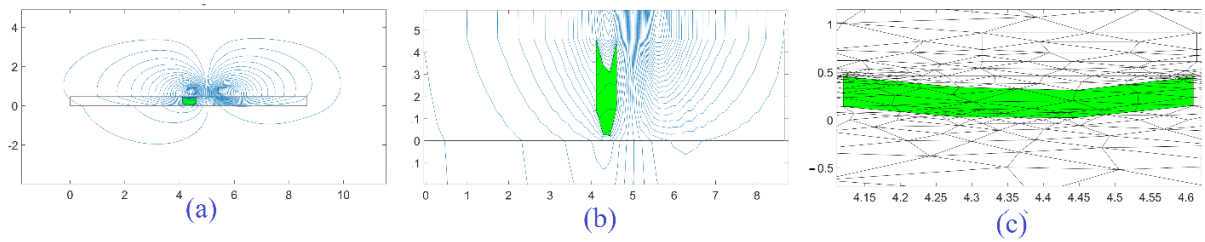

Figure 6-30 An example for a reconstructed defect within the sample. (a) Vector potential lines due to defect. (b) Zoomed plot for the defect. (c) Zoomed plot for the defect shows the elements.

After several iterations, we chose constrains to make the reconstructed defect within the sample as shown in Figure 6-30a that shows the resultant vector potential lines. Figure 6-30b shows a zoomed plot for the defect and how vector potential lines distributed in the sample. Figure 6-30c shows an extra zoomed plot for the defect with the constructing elements.

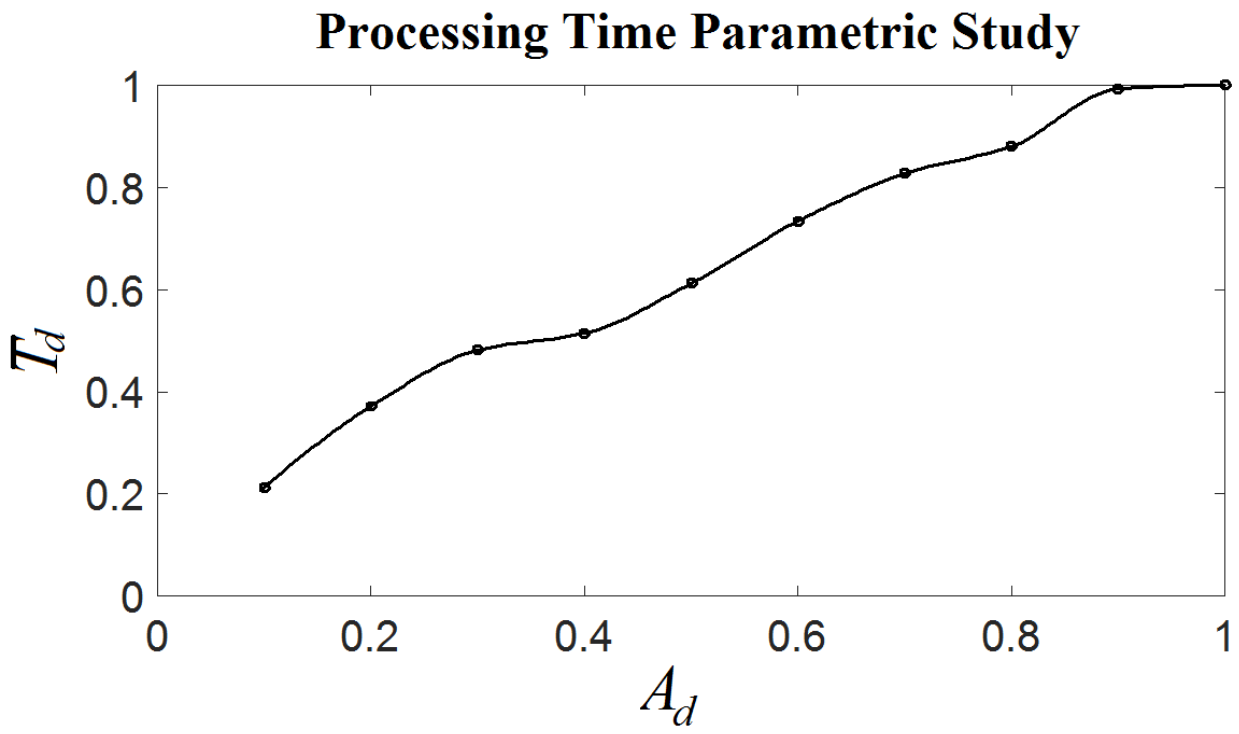

Figure 6-31 Normalized subregion areas vs. Normalized processing time

Figure 6-31 shows how using SFEMSFEM will be used to minimize processing time. Define T_d and A_d as:

$$T_d = \frac{t_2}{t_{Tot}} \tag{5.3a}$$

$$A_d = \frac{A_2}{A_{Tot}} \tag{5.3b}$$

Where: t_2 is time for processing region two only which is the defect region, t_{Tot} is the total time for processing the complete domain with both regions one and two, A_2 is the area for region two (defect region) and A_{Tot} is the total area for both regions one and two.

Increasing A_d that's defiantly will increase T_d. The maximum value for processing time will be when A_d=1 where SFEMSFEM will be turned to classical FEM by making the selected region of defect represents the entire domain. This result is logical if the total area increased by increasing

both areas of R_1 and R_2 since increasing the areas of the solution domain will increase the number of meshes and makes it takes longer time in processing.

7 Conclusions and Future Work

SFEM method is an effective method in solving different EM problems. In this thesis, this method was used to study some ECT problems for NDE applications. Excellent results have been achieved especially in saving time for solving large problems. This can help us to study more applications especially in inverse and optimization problems. We used SFEM solve both direct and inverse 2D-ECT problems. After that, we did an experimental validation to validate the presented computational results. The following will show the related conclusions and discussions to each part of the results presented in this thesis.

The proposed method was used successfully to find and plot magnetic potential lines for different cases and shapes of the defect. The objective of that part was to know how these defects can affect potential lines and how can that help us in detecting these defects in advanced applications of ECT. A ratio parameter was defined to study the relation between magnetic flux density values at some predetermined points with and without the existence of the defect. Then, these ratio values were used to study the relation between different defects shapes, angle of rotations, widths and depth from the sample's surfaces. Excellent results have been achieved compared to other techniques and to COMSOL in detecting defects. It was shown that increasing the depth of defect within metal will decrease its chance to be detected. While these defects will be easier to be detected if they lie within the skin depth distance. Also, the size of the defect and its rotation angle play an important factor in detecting defects. Increasing the size of the defects by increasing the width and the length of the defect will affect these ratios and will increase their values. It was shown that the maximum values of these ratios will be for those defects that are directly under the center of the coils and touching conductors surface. Regarding the processing time, it was shown that using SFEM improved processing time up to 90% comparing solving same problem using classical FEM.

The idea of having two regions in solving ECT problems came to improve both processing time and memory saving problems especially in advanced applications. Characterization defects is considered to be an inverse problem of using finite element with a selected optimization technique each running iteration until achieving the solution. Applying subregion method in the Finite Element solution for such problems give the benefits of minimizing computations in limited region. An elastic meshing scheme was used to solve the problem of numbering nodes inside the pre-divided regions each iteration and this method was improved to be used to generate meshes within the selected subregions. The elastic SFEM can save connectivity matrix each iteration for the entire elements. Minimizing the fitness, which was the difference between the calculated and measured magnetic flux density values score each iteration using both Genetic Algorithm and Simulated Annealing was used to get the most accurate defect shape. An excellent results were achieved using SFEM especially when Genetic Algorithm was used where 98% of the original defect could be reconstructed in very short time compared to classical FEM which proves that the presented method in this thesis can be used to locate hidden defects inside metals and to characterize these defects in addition to minimize processing time up to 90% of the total time and saving memory which allow this method to be used later in more complicated applications.

A magnetic field sensor using a tunneling magnetoresistive (TMR) element was used to measure the component of the magnetic field normal to the sample top surface. The TMR sensor was mounted on a PCB with a circuit to amplify the sensor output signal. The TMR sensor is placed in the sensor fixture and scanned over the coil that was placed on the top of the sample.

We tested the following samples:

1) Aluminum alloy T6061-T6 with edge defect.
2) Aluminum alloy T6061-T6 with subsurface defect.

3) Mild steel plate (0.15 - 0.30% carbon and Fe) with surface defect.

Where we get excellent results by testing these samples and it was easier to detect the aluminum defects rather than the steel defects due to high values for both conductivity (6.3×10^6 S/m) and relative permeability (2000) for steel sample.

Therefore, we use the aluminum sample to validate the computational SFEM results. After that, we used the experimental data to characterize hidden defect in this sample and after using our inverse SFEM solver using GA, we get an accuracy of 74% related to the original defect which is consider to be an excellent results since we are comparing experimental with computational data.

The experimental data that we get from the output of the lock-in amplifier came with noise and this noise may affect the reconstruction results. In addition, of scaling and phase shifting that may happen to the output data related to the following reasons, which also may consider as noise sources in experimental results:

1) Low pass filter used in the lock-in amplifier.
2) Surface roughness and sample microstructure.
3) Electrical noise.
4) Lift off distances for coils.
5) Temperature variation and thermal noise.
6) Changes in electromagnetic properties of the material, in case if we use nonlinear material. Nonlinear material.
7) Variation in testing speed.
8) Vibration of the scanner
9) TMR noise, related to solid state construction of TMR

All these factors may affect the output results and it will affect directly the reconstruction accuracy for the defect.

I believe that improving this technique will have tangible results especially in solving inverse FEM problems for the reasons and discussions that were presented in this thesis and other related research.

In computational analysis, researchers are facing many obstacles especially if they asked to validate their work experimentally. Working in solving these problems through my work on ECT problems and find logical explanations for results that I get, opens my mind to a lot of related thought and ideas that can be implemented in future to improve the algorithm and use it in a lot of related applications. The following are some recommendations for future work related to this topic.

1) Improving the presented SFEM solve 3D problems. We can start solving actual ECT problems by improving our solver to 3D FEM solver. In addition, we can improve the 3D SFEM solver for solving any computational physical problem.
2) Working on the absorber boundary conditions for open space problems. One of the major factors that increases processing ruing time is placing the sample and coils in a box of free space. In our computations, we choose the dimensions of this box to be very large which will increase processing time especially in classical FEM solutions. Therefore, applying absorber boundary conditions and Ballooning method will minimize processing time.
3) In our computational work, we used a coil with a fixed position. The effect for using a fixed position coil can be noticed when we did the experimental validation. We saw that we got a reconstruction accuracy of 75%. Using a moving coil in the future along the surface of the defect for each point for the measuring points will definitely increase the defect reconstruction accuracy.

4) We presented a study of a single defect; we can update our method to study multiple defects within the sample. Where we can select a specific region for each defect and continue our analysis.
5) We used the presented algorithm in this thesis to study ECT problems in a low range of frequencies. We can reproduce our FEM solver to be used at high frequency range. For example, we can use SFEM in finding the full wave analysis for 3striplines and coupled microstrip lines and in microwave engineering in general. Doing that means we need to solve Maxwell's equations in high frequency condition and continue updating the algorithm by deriving the subregions, then derive the needed elastic mesh generator that should be used and finally use the suitable optimization technique in case of solving inverse problems, like measuring the width and thickness for the conductor strips in microstrip lines for a given characteristic impedances matching purposes.
6) We can update our presented algorithm to solve multi-physical FEM problems, like electro-thermal problems.
7) When we test the mild steel sample, we could not get an accurate results due to the high values of the relative permeability (2000) for that sample. We can work in developing a techniques for demagnetize these kind of samples so we can use Eddy Current in testing such samples an get more accurate results.
8) In our experimental validation, we use one TMR sensor, we can use more than one sensor in the future to get more accurate results.
9) In our experimental validation, we tried as much as we can to make an equivalent 2D model for the computational problem. Therefore, we used a traditional coil that we did it from electric wire. We can think of using the GMR with a linear excitation coil and we can try

to update our algorithm parameters to handle this planner coil by consider it as a current sheet in our FEM modeling.

10) Subregion method was applied to serve FEM in this study where it can be derived to merge with other computational techniques for different applications like Finite Difference Frequency Domain method (FDFD) and Finite Difference Time Domain method (FDTD).

11) In our solution for inverse defect reconstruction problem we chose our design parameters to vary in y- direction. We can generalize the algorithm so we can move these design parameters in both *x* and *y* directions.

12) We can make a comparison study between defects parameters and the probability of detect these defects. We noticed that some defects are easy to be detected while other were more difficult. In addition, I noticed that the magnetic field density plot for the entire problem can give us some information regarding the initial position of these defects. I believe that doing some line segment detecting analysis will be significant in detecting 2D hidden defect and characterize their shapes from theoretical point of view.

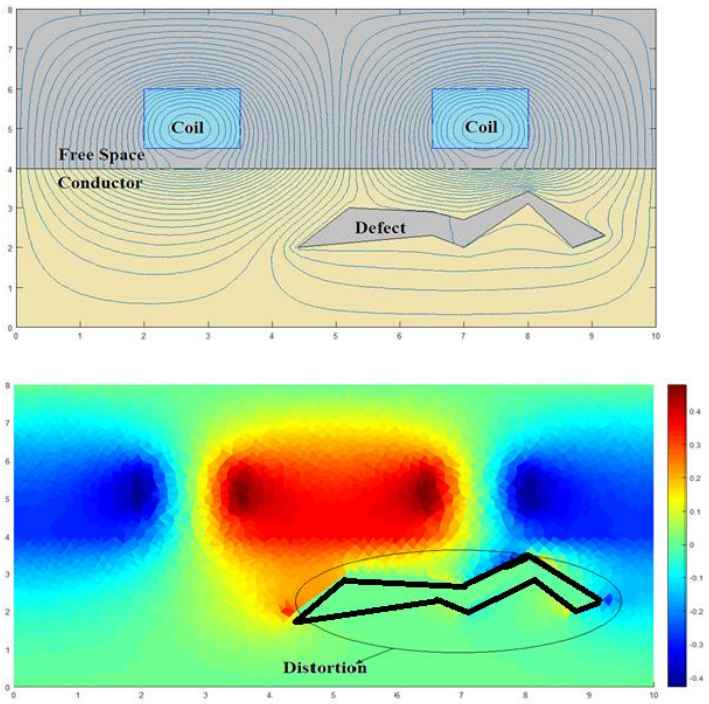

Figure 7-1 Using segment line detection to characterize hidden cracks

This can be useful in 3D analysis. We can do a FEM analysis for the entire domain. Then we can find and plot the magnetic flux density in each tetrahedral. The 2D side views, like, top bellow, right and left can give us an initial data regarding the hidden defects inside these metals. For this given problem, we propose to localize the defect from an image processing perspective. Therefore, the first step would be to transfer the output visualization of the system including the defect pattern into an RGB image. This is accomplished through sampling points in the vertical and horizontal directions of the plot, and then assign those samples to pixels accordingly. After obtaining the image, many computer vision and image processing techniques can be used to highlight the defect in a precise manner. The defect can be characterized as a single fully connected region, which exhibits high frequency edges on most of the boundaries, while some other edges are low frequencies. One approach is to simply try to detect the edges of the defect in the image using Sobel or Canny edge detectors. However, the results would appear too noisy since some edges are

not clear for the defect. Relaying on color information is also a bad choice, since the defect might contain colors similar to normal regions. One promising technique is to use a method named superpixel segmentation. In general, a superpixel is a polygonal part of an image, larger than a normal pixel, which has common color and texture information. Learning some features of the superpixels containing the defect, would help us to define a full segmentation of the entire defect part. This segmentation method is very well studied by researchers in the image-processing field, and it has been used in many applications. For example, object detection [140], depth estimation [141], medical image segmentation [142], and plant/tree disease segmentation [143].

BIBLIOGRAPHY

BIBLIOGRAPHY

[1] P. Baskaran, A. L. Ribeiro, and H. G. Ramos, "The dilation invariance principle in eddy-current non-destructive evaluation technique analytical justification," in *2017 IEEE International Instrumentation and Measurement Technology Conference (I2MTC)*, 2017, pp. 1-6.

[2] A. Sophian, G. Y. Tian, D. Taylor, and J. Rudlin, "A feature extraction technique based on principal component analysis for pulsed eddy current NDT," *NDT & e International*, vol. 36, pp. 37-41, 2003.

[3] C. Dodd and W. Deeds, "Analytical Solutions to Eddy-Current Probe-Coil Problems," *Journal of applied physics*, vol. 39, pp. 2829-2838, 1968.

[4] W. Lord, Y. S. Sun, S. Udpa, and S. Nath, "A finite element study of the remote field eddy current phenomenon," *IEEE Transactions on Magnetics*, vol. 24, pp. 435-438, 1988.

[5] R. Hamia, C. Cordier, S. Saez, and C. Dolabdjian, "Eddy-current nondestructive testing using an improved GMR magnetometer and a single wire as inducer: A FEM performance analysis," *IEEE Transactions on Magnetics*, vol. 46, pp. 3731-3737, 2010.

[6] J. Blitz, *Electrical and magnetic methods of non-destructive testing* vol. 3: Springer Science & Business Media, 2012.

[7] G. Murthy and P. Chandrachoodan, "Magnetic particle testing," *Chemical Concepts*, vol. 5, pp. 23-27, 1978.

[8] B. Collins and C. Eick, "Quick Break," *The NDT Technician*, vol. 13, pp. 1-3, 2014.

[9] M. Inamo, K. Sakai, T. Kiwa, and K. Tsukada, "Application to non-destructive evaluation of gas barrier films using a high-speed terahertz time-domain spectroscopy," in *2016 Progress in Electromagnetic Research Symposium (PIERS)*, 2016, pp. 3921-3921.

[10] J. Summerscales, *Non-destructive testing of fibre-reinforced plastics composites* vol. 2: Springer Science & Business Media, 1990.

[11] P. E. Mix, "Liquid Penetrant Tests," *Introduction to Nondestructive Testing: A Training Guide, Second Edition*, pp. 221-245.

[12] C. Dang, J. Gao, Z. Wang, F. Chen, and Y. Xiao, "Multi-step radiographic image enhancement conforming to weld defect segmentation," *IET Image Processing*, vol. 9, pp. 943-950, 2015.

[13] T. D. Luckey, *Hormesis with ionizing radiation*: CRC press Boca Raton, FL, 1980.

[14] B. Matuszewski, L.-K. Shark, M. Varley, and J. Smith, "Region-based wavelet fusion of ultrasonic, radiographic and shearographyc non-destructive testing images," in *Proceedings of the 15th World Conference on Non-Destructive Testing*, 2000, pp. 15-21.

[15] Y. Hung, "Shearography: a new optical method for strain measurement and nondestructive testing," *Optical Engineering,* vol. 21, p. 213391, 1982.

[16] U. Hampel, A. Bieberle, D. Hoppe, J. Kronenberg, E. Schleicher, T. Sühnel, *et al.*, "High resolution gamma ray tomography scanner for flow measurement and non-destructive testing applications," *Review of scientific instruments,* vol. 78, p. 103704, 2007.

[17] P. Fan and X. Liu, "An improved denoising method for ultrasonic echo of non-destructive evaluation," in *2016 10th IEEE International Conference on Anti-counterfeiting, Security, and Identification (ASID)*, 2016, pp. 30-33.

[18] J. Blitz and G. Simpson, *Ultrasonic methods of non-destructive testing* vol. 2: Springer Science & Business Media, 1995.

[19] M. Beard and M. Lowe, "Non-destructive testing of rock bolts using guided ultrasonic waves," *International journal of rock mechanics and mining sciences,* vol. 40, pp. 527-536, 2003.

[20] C. Garnier, M.-L. Pastor, F. Eyma, and B. Lorrain, "The detection of aeronautical defects in situ on composite structures using Non Destructive Testing," *Composite structures,* vol. 93, pp. 1328-1336, 2011.

[21] C. Albano, N. Camacho, J. Reyes, J. Feliu, and M. Hernández, "Influence of scrap rubber addition to Portland I concrete composites: destructive and non-destructive testing," *Composite Structures,* vol. 71, pp. 439-446, 2005.

[22] S. Chatillon, G. Cattiaux, M. Serre, and O. Roy, "Ultrasonic non-destructive testing of pieces of complex geometry with a flexible phased array transducer," *Ultrasonics*, vol. 38, pp. 131-134, 2000.

[23] X. Li, B. Gao, W. L. Woo, G. Y. Tian, X. Qiu, and L. Gu, "Quantitative Surface Crack Evaluation Based on Eddy Current Pulsed Thermography," *IEEE Sensors Journal*, vol. 17, pp. 412-421, 2017.

[24] S. Kharkovsky and R. Zoughi, "Microwave and millimeter wave nondestructive testing and evaluation-Overview and recent advances," *IEEE Instrumentation & Measurement Magazine,* vol. 10, pp. 26-38, 2007.

[25] B. Hobbs and M. T. Kebir, "Non-destructive testing techniques for the forensic engineering investigation of reinforced concrete buildings," *Forensic science international,* vol. 167, pp. 167-172, 2007.

[26] S. Hannachi and M. N. Guetteche, "Application of the combined method for evaluating the compressive strength of concrete on site," *Open Journal of Civil Engineering*, vol. 2, p. 16, 2012.

[27] H.-S. Shang, T.-H. Yi, and L.-S. Yang, "Experimental study on the compressive strength of big mobility concrete with nondestructive testing method," *Advances in Materials Science and Engineering*, vol. 2012, 2012.

[28] K. Virkler and I. K. Lednev, "Blood species identification for forensic purposes using Raman spectroscopy combined with advanced statistical analysis," *Analytical chemistry*, vol. 81, pp. 7773-7777, 2009.

[29] M. M. Schwartz, "Composite materials. Volume 1: Properties, non-destructive testing, and repair," 1997.

[30] J. Hoła and K. Schabowicz, "State-of-the-art non-destructive methods for diagnostic testing of building structures–anticipated development trends," *Archives of civil and mechanical engineering*, vol. 10, pp. 5-18, 2010.

[31] P. Cawley and R. D. Adams, "A vibration technique for non-destructive testing of fibre composite structures," *Journal of Composite Materials*, vol. 13, pp. 161-175, 1979.

[32] C.-H. Chen, *Ultrasonic and advanced methods for nondestructive testing and material characterization*: World Scientific, 2007.

[33] R. Jacques, T. Clarke, S. Morikawa, and T. Strohaecker, "Monitoring the structural integrity of a flexible riser during dynamic loading with a combination of non-destructive testing methods," *NDT & E International*, vol. 43, pp. 501-506, 2010.

[34] C. P. Ratcliffe, "Damage detection using a modified Laplacian operator on mode shape data," *Journal of Sound and Vibration*, vol. 204, pp. 505-517, 1997.

[35] N. K. Anuar, W. T. Wui, D. K. Ghodgaonkar, and M. N. Taib, "Characterization of hydroxypropylmethylcellulose films using microwave non-destructive testing technique," *Journal of pharmaceutical and biomedical analysis*, vol. 43, pp. 549-557, 2007.

[36] N. Qaddoumi, A. H. El-Hag, M. Al Hosani, I. Al Mansouri, and H. Al Ghufli, "Detecting defects in outdoor non-ceramic insulators using near-field microwave non-destructive testing," *IEEE Transactions on Dielectrics and Electrical insulation*, vol. 17, pp. 402-407, 2010.

[37] D. C. Carpenter, "Use of the finite element method in simulation and visualization of electromagnetic nondestructive testing applications," *Materials evaluation*, vol. 58, pp. 877-881, 2000.

[38] M. Kupke, K. Schulte, and R. Schüler, "Non-destructive testing of FRP by dc and ac electrical methods," *Composites Science and Technology*, vol. 61, pp. 837-847, 2001.

[39] C. Maierhofer, A. Brink, M. Röllig, and H. Wiggenhauser, "Quantitative impulse-thermography as non-destructive testing method in civil engineering–Experimental results and numerical simulations," *Construction and Building Materials,* vol. 19, pp. 731-737, 2005.

[40] J. C. Santamarina and D. Fratta, *Introduction to discrete signals and inverse problems in civil engineering*, 1998.

[41] D. Titman, "Applications of thermography in non-destructive testing of structures," *NDT & e International,* vol. 34, pp. 149-154, 2001.

[42] R. Jones, "The non-destructive testing of concrete," *Magazine of Concrete Research,* vol. 1, pp. 67-78, 1949.

[43] T. Root, R. Tillinghast, M. Maher, W. LaFlash, and R. Krupa, "Endoscopic delivery system for the non-destructive testing and evaluation of remote flaws," ed: Google Patents, 2004.

[44] M. Huang, L. Jiang, P. K. Liaw, C. R. Brooks, R. Seeley, and D. L. Klarstrom, "Using acoustic emission in fatigue and fracture materials research," *JOM,* vol. 50, pp. 1-14, 1998.

[45] H. Weinstock, "A review of SQUID magnetometry applied to nondestructive evaluation," *IEEE Transactions on Magnetics,* vol. 27, pp. 3231-3236, 1991.

[46] J. M. Papazian, J. Nardiello, R. P. Silberstein, G. Welsh, D. Grundy, C. Craven, *et al.*, "Sensors for monitoring early stage fatigue cracking," *International journal of fatigue,* vol. 29, pp. 1668-1680, 2007.

[47] R. P. Gangloff, "Crack tip modeling of hydrogen environement embrittlement: application to fracture mechanics life prediction," *Materials Science and Engineering: A,* vol. 103, pp. 157-166, 1988.

[48] Y. Gao, G. Y. Tian, P. Wang, and H. Wang, "Emissivity correction of eddy current pulsed thermography for rail inspection," in *2016 IEEE Far East NDT New Technology & Application Forum (FENDT)*, 2016, pp. 108-112.

[49] R. Pohl, A. Erhard, H.-J. Montag, H.-M. Thomas, and H. Wüstenberg, "NDT techniques for railroad wheel and gauge corner inspection," *NDT & e International,* vol. 37, pp. 89-94, 2004.

[50] X. P. Maldague, "Introduction to NDT by active infrared thermography," *Materials Evaluation,* vol. 60, pp. 1060-1073, 2002.

[51] S. Dixon, R. Edwards, and X. Jian, "Inspection of rail track head surfaces using electromagnetic acoustic transducers (EMATs)," *Insight-Non-Destructive Testing and Condition Monitoring,* vol. 46, pp. 326-330, 2004.

[52] D. Terry, "The development of eddy-current testing techniques for tube inspection," *Radio and Electronic Engineer,* vol. 26, pp. 373-382, 1963.

[53] Y. Sun, S. Udpa, W. Lord, and D. Cooley, "A remote field eddy current NDT probe for the inspection of metallic plates," *Materials evaluation,* vol. 54, 1996.

[54] D. Jinfeng, K. Yihua, and W. Xinjun, "Tubing thread inspection by magnetic flux leakage," *NDT & E International,* vol. 39, pp. 53-56, 2006.

[55] G. Pichenot and T. Sollier, "Eddy Current Modelling For Nondestructive Testing," *Journal of Nondestructive Testing,* vol. 8, pp. 1-5, 2003.

[56] Y.-M. Shyu and F. C.-N. Hong, "Low-temperature growth and field emission of aligned carbon nanotubes by chemical vapor deposition," *Materials Chemistry and Physics,* vol. 72, pp. 223-227, 2001.

[57] A. Skarlatos, G. Pichenot, D. Lesselier, M. Lambert, and B. Duchene, "Electromagnetic modeling of a damaged ferromagnetic metal tube by a volume integral equation formulation," *IEEE Transactions on Magnetics,* vol. 44, pp. 623-632, 2008.

[58] B. Tuzson, J. Mohn, M. Zeeman, R. Werner, W. Eugster, M. Zahniser, *et al.*, "High precision and continuous field measurements of δ 13 C and δ 18 O in carbon dioxide with a cryogen-free QCLAS," *Applied Physics B,* vol. 92, p. 451, 2008.

[59] A. El-Gendy, E. Ibrahim, V. Khavrus, Y. Krupskaya, S. Hampel, A. Leonhardt, *et al.*, "The synthesis of carbon coated Fe, Co and Ni nanoparticles and an examination of their magnetic properties," *Carbon,* vol. 47, pp. 2821-2828, 2009.

[60] Q. Ouyang, K. Qin, X. Zhang, Z. Niu, and S. Hou, "Thickness and surface flaws detection using EMAT&ECT for medium plate rolling in intermediate cooling process," in *2016 IEEE Far East NDT New Technology & Application Forum (FENDT)*, 2016, pp. 151-156.

[61] Y. Yu, D. Zhang, C. Lai, and G. Tian, "Quantitative Approach for Thickness and Conductivity Measurement of Monolayer Coating by Dual-Frequency Eddy Current Technique," *IEEE Transactions on Instrumentation and Measurement,* vol. 66, pp. 1874-1882, 2017.

[62] Z. Su, L. Udpa, G. Giovinco, S. Ventre, and A. Tamburrino, "Monotonicity principle in pulsed eddy current testing and its application to defect sizing," in *2017 International Applied Computational Electromagnetics Society Symposium - Italy (ACES)*, 2017, pp. 1-2.

[63] W. Jialong, Z. Deqiang, W. Jun, G. Xuedong, Y. Lihua, A. Wei, *et al.*, "Surface crack detection for carbon fiber reinforced plastic (CFRP) materials using pulsed eddy current testing," in *2014 IEEE Far East Forum on Nondestructive Evaluation/Testing*, 2014, pp. 181-185.

[64] L. Bo, L. Feilu, J. Zhongqing, and L. Jiali, "Eddy Current Array Instrument and Probe for Crack Detection of Aircraft Tubes," in *2010 International Conference on Intelligent Computation Technology and Automation*, 2010, pp. 177-180.

[65] D. Cai, C. Zou, Z. Sun, Q. Chen, and J. Wang, "Geometric optimization of a flexible arrayed eddy current sensor for non-destructive testing," in *2016 IEEE SENSORS*, 2016, pp. 1-3.

[66] K. Weise, R. Schmidt, M. Carlstedt, M. Ziolkowski, H. Brauer, and H. Toepfer, "Optimal Magnet Design for Lorentz Force Eddy-Current Testing," *IEEE Transactions on Magnetics,* vol. 51, pp. 1-15, 2015.

[67] M. Zec, R. P. Uhlig, M. Ziolkowski, and H. Brauer, "Lorentz force eddy current testing: Modelling of permanent magnets in dynamic simulation using logical expressions," in *IET 8th International Conference on Computation in Electromagnetics (CEM 2011)*, 2011, pp. 1-2.

[68] G. Van Drunen and V. Cecco, "Recognizing limitations in eddy-current testing," *NDT international,* vol. 17, pp. 9-17, 1984.

[69] M. De Goeje and K. Wapenaar, "Non-destructive inspection of carbon fibre-reinforced plastics using eddy current methods," *Composites,* vol. 23, pp. 147-157, 1992.

[70] X. Gros, K. Ogi, and K. Takahashi, "Eddy current, ultrasonic C-scan and scanning acoustic microscopy testing of delaminated quasi-isotropic CFRP materials: a case study," *Journal of reinforced plastics and composites,* vol. 17, pp. 389-405, 1998.

[71] S. Lee, D. Y. Kwak, and I. Sim, "Immersed finite element method for eigenvalue problem," *Journal of Computational and Applied Mathematics,* vol. 313, pp. 410-426, 3/15/ 2017.

[72] J. Li, Y. Huang, and W. Yang, "An adaptive edge finite element method for electromagnetic cloaking simulation," *Journal of Computational Physics,* vol. 249, pp. 216-232, 2013/09/15/ 2013.

[73] D. Garcia-Donoro, A. Amor-Martin, and L. E. Garcia-Castillo, "Higher-Order Finite Element Electromagnetics Code for HPC environments," *Procedia Computer Science*, vol. 108, pp. 818-827, // 2017.

[74] U. Römer, S. Schöps, and H. De Gersem, "A defect corrected finite element approach for the accurate evaluation of magnetic fields on unstructured grids," *Journal of Computational Physics*, vol. 335, pp. 688-699, 4/15/ 2017.

[75] S. R. H. Hoole and P. R. P. Hoole, "Finite Element Programs for Teaching Electromagnetics," *IEEE Transactions on Education*, vol. E-29, pp. 21-26, 1986.

[76] D. Andrzej, "Finite element modeling of magnetic field in electrical machines: Scalar or vector potential formulation part I: Comparative description of methods," in *2016 13th Selected Issues of Electrical Engineering and Electronics (WZEE)*, 2016, pp. 1-6.

[77] A. Bermudez, C. Lopez, R. Rodriguez, and P. Salgado, "A finite element method for the eddy current problem in terms of the current density. Application to nondestructive

testing," in *2007 International Conference on Electromagnetics in Advanced Applications*, 2007, pp. 277-280.

[78] H. Tsuboi, N. Seshima, I. Sebestyen, J. Pavo, S. Gyimothy, and A. Gasparics, "Transient eddy current analysis of pulsed eddy current testing by finite element method," *IEEE Transactions on Magnetics,* vol. 40, pp. 1330-1333, 2004.

[79] B. Jiang, "Study of Open Boundary Electromagnetic Field Coupling Computation Method," in *2012 Asia-Pacific Power and Energy Engineering Conference*, 2012, pp. 1-4.

[80] D. Chen, K. Shao, X. Hu, Y. Guo, and J. Lavers, "A Subregion Expansion Method for Computational Electromagnetics," in *INTERMAG 2006 - IEEE International Magnetics Conference*, 2006, pp. 337-337.

[81] K. Zhao, V. Rawat, and J. F. Lee, "A Domain Decomposition Method for Electromagnetic Radiation and Scattering Analysis of Multi-Target Problems," *IEEE Transactions on Antennas and Propagation,* vol. 56, pp. 2211-2221, 2008.

[82] C. Hwu, S.-T. Huang, and C.-C. Li, "Boundary-based finite element method for two-dimensional anisotropic elastic solids with multiple holes and cracks," *Engineering Analysis with Boundary Elements,* vol. 79, pp. 13-22, 6// 2017.

[83] M. Ogino, A. Takei, S.-i. Sugimoto, and S. Yoshimura, "A numerical study of iterative substructuring method for finite element analysis of high frequency electromagnetic fields," *Computers & Mathematics with Applications,* vol. 72, pp. 2020-2027, 2016/10/01/ 2016.

[84] Z. Q. You, Z. W. Jiang, Y. S. Sun, and L. Udpa, "Application of the substructure-frontal method for repeated solution of large sparse matrix equations to field problems," *IEEE Transactions on Magnetics,* vol. 24, pp. 326-329, 1988.

[85] K. Weeber and S. R. H. Hoole, "The subregion method in magnetic field analysis and design optimization," *IEEE Transactions on Magnetics,* vol. 28, pp. 1561-1564, 1992.

[86] *https://en.wikipedia.org/wiki/Main_Page*.

[87] L. Zhuo, F. Yi, and S. Meng, "An inverse method for the estimation of a long-duration surface heat flux on a finite solid," *International Journal of Heat and Mass Transfer,* vol. 106, pp. 1087-1096, 3// 2017.

[88] P. Tahmasebi, F. Javadpour, and M. Sahimi, "Stochastic shale permeability matching: Three-dimensional characterization and modeling," *International Journal of Coal Geology,* vol. 165, pp. 231-242, 2016/08/01/ 2016.

[89] R. V. Ambartsumian, "A life in astrophycis. Selected papers of Viktor A. Ambartsumian," *Astrophysics,* vol. 41, pp. 328-330, 1998/10/01 1998.

[90] H. H. Bauschke, R. S. Burachik, P. L. Combettes, V. Elser, D. R. Luke, and H. Wolkowicz, *Fixed-point algorithms for inverse problems in science and engineering* vol. 49: Springer Science & Business Media, 2011.

[91] F. S. Lobato, V. Steffen Jr, and A. Silva Neto, "Solution of inverse radiative transfer problems in two-layer participating media with differential evolution," *Inverse Problems in Science and Engineering,* vol. 18, pp. 183-195, 2010.

[92] Z. Ostrowski, R. Białecki, and A. Kassab, "Solving inverse heat conduction problems using trained POD-RBF network inverse method," *Inverse Problems in Science and Engineering,* vol. 16, pp. 39-54, 2008.

[93] D. Colton and A. Kirsch, "A simple method for solving inverse scattering problems in the resonance region," *Inverse problems,* vol. 12, p. 383, 1996.

[94] M. Gockenbach, B. Jadamba, and A. Khan, "Equation error approach for elliptic inverse problems with an application to the identification of Lamé parameters," *Inverse Problems in Science and Engineering,* vol. 16, pp. 349-367, 2008.

[95] S. R. H. Hoole, *Computer-aided analysis and design of electromagnetic devices*: Elsevier, 1989.

[96] S. Sivasuthan, V. U. Karthik, T. Mathialakan, M. R. Rawashdeh, P. Jayakumar, R. S. Thyagarajan, *et al.*, "GRAPHICS PROCESSING UNIT COMPUTATIONS FOR FINITE ELEMENT OPTIMIZATION: A REVIEW AND SOME ISSUES TO BE ADDRESSED," *REVUE ROUMAINE DES SCIENCES TECHNIQUES-SERIE ELECTROTECHNIQUE ET ENERGETIQUE,* vol. 60, pp. 241-251, 2015.

[97] Mohammad R. Rawashdeh, Zhiyi Su, Anton Efremov, Swathi Ramesh, Anders Rosell, Lalita Udpa, S. Ratnajeevan H. Hoole, Yiming Deng," Solving Inverse Eddy Current Testing Problems using Subregion Finite Element Method", ISP 2018, MI, USA..

[98] B. f. Yang, Z. Hui, Z. Chao, and C. Hai-xia, "Detecting non-magnetic conducting flat plates with pulsed Remote Eddy Current Field technique," in *2015 IEEE Far East NDT New Technology & Application Forum (FENDT)*, 2015, pp. 267-271.

[99] J. Xin, N. Lei, L. Udpa, and S. S. Udpa, "Nondestructive Inspection Using Rotating Magnetic Field Eddy-Current Probe," *IEEE Transactions on Magnetics,* vol. 47, pp. 1070-1073, 2011.

[100] R. Vázquez, A. Buffa, and L. d. Rienzo, "Isogeometric FEM Implementation of High-Order Surface Impedance Boundary Conditions," *IEEE Transactions on Magnetics,* vol. 50, pp. 1-8, 2014.

[101] O. Biro, K. Preis, K. R. Richter, R. Heller, P. Komarek, and W. Maurer, "FEM calculation of eddy current losses and forces in thin conducting sheets of test facilities for fusion reactor components," *IEEE Transactions on Magnetics,* vol. 28, pp. 1509-1512, 1992.

[102] M. Tanaka and H. Tsuboi, "Finite element model of natural crack in eddy current testing problem," *IEEE Transactions on Magnetics*, vol. 37, pp. 3125-3128, 2001.

[103] B. Helifa, M. Féliachi, I. K. Lefkaier, F. Boubenider, A. Zaoui, and N. Lagraa, "Characterization of surface cracks using eddy current NDT simulation by 3D-FEM and inversion by neural network," *Applied Computational Electromagnetics Society Journal*, vol. 31, pp. 187-194, 2016.

[104] M. Fardmanesh, F. Sarreshtedari, A. Pourhashemi, E. Ansari, M. A. Vesaghi, J. Schubert, *et al.*, "Optimization of NDE Characterization Parameters for a RF-SQUID Based System Using FEM Analysis," *IEEE Transactions on Applied Superconductivity*, vol. 19, pp. 791-795, 2009.

[105] Y. He and R. Yang, "Eddy Current Volume Heating Thermography and Phase Analysis for Imaging Characterization of Interface Delamination in CFRP," *IEEE Transactions on Industrial Informatics*, vol. 11, pp. 1287-1297, 2015.

[106] Z. Shuhao, L. Xuwei, H. Pingjie, P. Xiedan, H. Dibo, and Z. Guangxin, "Method of imaging and evaluation for defect based on pulsed eddy current," in *2016 IEEE International Instrumentation and Measurement Technology Conference Proceedings*, 2016, pp. 1-6.

[107] Z. Zeng, T. Wang, L. Sun, R. He, and J. Chen, "A Domain Decomposition Finite-Element Method for Eddy-Current Testing Simulation," *IEEE Transactions on Magnetics*, vol. 51, pp. 1-9, 2015.

[108] V. Karthik, "Reconstructing and Classifying Damage in a 2D Steel Plate Using Non-Destructive Evaluation (NDE) Methods."

[109] Mohammad. R. Rawashdeh, Anders Rosell, Lalita Udpa, S. Ratnajeevan H. Hoole and Yiming Deng," Subregion Finite Element Hybrid Optimization Using Genetics Algorithm and Simulated Annealing for Nondestructive Evaluation Inverse Problems", ASNT Annual Conference 2017, TN, USA.

[110] Mohammad. R. Rawashdeh, A. Rosell, L. Udpa, S. R. H. Hoole and Y. Deng, "Optimized Solutions for Defect Characterization in 2-D Inverse Eddy Current Testing Problems Using Subregion Finite Element Method," in IEEE Transactions on Magnetics, vol. 54, no. 8, pp. 1-15, Aug. 2018, Art no. 6201515.

[111] Mohammad. R. Rawashdeh, A. Rosell, L. Udpa, S. R. H. Hoole, and Y. Deng, "A computational investigation and smooth-shaped defect synthesis for eddy current testing problems using the subregion finite element method," Res. Nondestruct. Eval., 2018. [Online]. Available: https://doi.org/10.1080/09349847.2018.1427819.

[112] S. Sivasuthan, V. U. Karthik, A. Rahunanthan, P. Jayakumar, R. S. Thyagarajan, L. Udpa, *et al.*, "A Script-Based, Parameterized Finite Element Mesh for Design and NDE on a GPU," *IETE Technical Review*, vol. 32, pp. 94-103, 2015/03/04 2015.

[113] S. R. H. Hoole, V. U. Karthik, S. Sivasuthan, A. Rahunanthan, R. S. Thyagarajan, and P. Jayakumar, "Finite elements, design optimization, and nondestructive evaluation: A review in magnetics, and future directions in GPU-based, element-by-element coupled optimization and NDE," *International Journal of Applied Electromagnetics and Mechanics,* vol. 47, pp. 607-627, 2015.

[114] S. Krishnakumar and S. R. H. Hoole, "A common algorithm for various parametric geometric changes in finite element design sensitivity computation," *Journal of Materials Processing Technology,* vol. 161, pp. 368-373, 2005/04/10/ 2005.

[115] V. U. Karthik, "Shape optimization using finite element analysis in eddy current testing and electro-thermal coupled problems," 3739700 Ph.D., Michigan State University, Ann Arbor, 2015.

[116] S. Sivasuthan, "Software tool methodologies on a GPU for finite element optimization in magnetics," 3739735 Ph.D., Michigan State University, Ann Arbor, 2015.

[117] S. Sivasuthan, "The General Purpose Parameter Based Two Dimensional Mesh Generator," in *2014 American Society For Engineering Education North Central Section Conference*, 2014.

[118] S. R. H. Hoole and P. R. P. Hoole, *A Modern Short Course in Engineering Electromagnetics*: Oxford University Press, 1996.

[119] J. Koko, "A Matlab mesh generator for the two-dimensional finite element method," *Applied Mathematics and Computation,* vol. 250, pp. 650-664, 2015/01/01/ 2015.

[120] T. Rahman and J. Valdman, "Fast MATLAB assembly of FEM matrices in 2D and 3D: Nodal elements," *Applied Mathematics and Computation,* vol. 219, pp. 7151-7158, 2013/03/01/ 2013.

[121] M. R. Filho, J. T. Pinho, J. P. Silva, K. Z. Nobrega, and H. E. Hernandez-Figueroa, "A FEM mesh generator for large size aspect ratio problems with applications in optoelectronics," in *Proceedings of the 2003 SBMO/IEEE MTT-S International Microwave and Optoelectronics Conference - IMOC 2003. (Cat. No.03TH8678)*, 2003, pp. 589-593 vol.2.

[122] M. Sulman, J. F. Williams, and R. D. Russell, "Optimal mass transport for higher dimensional adaptive grid generation," *Journal of Computational Physics,* vol. 230, pp. 3302-3330, 2011/05/01/ 2011.

[123] F. L. Yang, C. H. Chen, and D. L. Young, "A novel mesh regeneration algorithm for 2D FEM simulations of flows with moving boundary," *Journal of Computational Physics,* vol. 230, pp. 3276-3301, 2011/05/01/ 2011.

[124] H. Abbasi, S. Haghzad, S. Amirkhani, and M. Eshghi, "Early detection of breast cancer using genetic algorithm and Neuro-Fuzzy network," in *2014 22nd Iranian Conference on Electrical Engineering (ICEE)*, 2014, pp. 1939-1944.

[125] J. A. B. Otero, S. Pacheco, E. C. Silva, C. R. H. Barbosa, and E. C. Monteiro, "Application of genetic algorithms to the solution of the biomagnetic inverse problem, using data acquired by a 16-Channel SQUID system," in *2016 IEEE Latin American Conference on Computational Intelligence (LA-CCI)*, 2016, pp. 1-6.

[126] S. Szénási and I. Felde, "Configuring genetic algorithm to solve the inverse heat conduction problem," in *2017 IEEE 15th International Symposium on Applied Machine Intelligence and Informatics (SAMI)*, 2017, pp. 000387-000392.

[127] Q. Anyong and L. Ching Kwang, "Shape reconstruction of a perfectly conducting cylinder using real-coded genetic algorithm," in *IEEE Antennas and Propagation Society International Symposium. 1999 Digest. Held in conjunction with: USNC/URSI National Radio Science Meeting (Cat. No.99CH37010)*, 1999, pp. 2148-2151 vol.3.

[128] L. Beghou, F. Costa, and L. Pichon, "Detection of Electromagnetic Radiations Sources at the Switching Time Scale Using an Inverse Problem-Based Resolution Method—Application to Power Electronic Circuits," *IEEE Transactions on Electromagnetic Compatibility*, vol. 57, pp. 52-60, 2015.

[129] R. Tang, S. Yang, Y. Li, G. Wen, and T. Mei, "Combined strategy of improved simulated annealing and genetic algorithm for inverse problem," *IEEE Transactions on Magnetics*, vol. 32, pp. 1326-1329, 1996.

[130] T. I. Alecu, S. Voloshynovskiy, and T. Pun, "Localization properties of an EEG sensor system: Lower bounds and optimality," in *2004 12th European Signal Processing Conference*, 2004, pp. 537-540.

[131] X. Rui, L. Gongyuan, and H. Dong, "Simulated Annealing Algorithm for Solving a Bi-level Optimization Model on High-speed Railway Station Location," in *2010 Third International Conference on Information and Computing*, 2010, pp. 159-162.

[132] M. C. Robini, N. Freud, and J. M. Letang, "Efficient simulated annealing for full inverse treatment planning," in *2013 IEEE Nuclear Science Symposium and Medical Imaging Conference (2013 NSS/MIC)*, 2013, pp. 1-5.

[133] B. Mhamdi, K. Grayaa, and T. Aguili, "Microwave imaging for conducting scatterers by hybrid particle swarm optimization with simulated annealing," in *Eighth International Multi-Conference on Systems, Signals & Devices*, 2011, pp. 1-6.

[134] R. Albanese, G. Rubinacci, and F. Villone, "An integral computational model for crack simulation and detection via eddy currents," *Journal of Computational Physics*, vol. 152, pp. 736-755, 1999.

[135] T. Khan and P. Ramuhalli, "A recursive Bayesian estimation method for solving electromagnetic nondestructive evaluation inverse problems," *IEEE Transactions on Magnetics*, vol. 44, pp. 1845-1855, 2008.

[136] T. Khan and P. Ramuhalli, "Sequential Monte Carlo methods for electromagnetic NDE inverse problems—Evaluation and comparison of measurement models," *IEEE Transactions on Magnetics*, vol. 45, pp. 1566-1569, 2009.

[137] T. Kundu, *Ultrasonic and Electromagnetic NDE for Structure and Material Characterization: Engineering and Biomedical Applications*: CRC Press, 2012.

[138] H. A. Sabbagh, R. K. Murphy, E. H. Sabbagh, J. C. Aldrin, J. Knopp, and M. Blodgett, "Computational electromagnetics and model-based inversion: a modern paradigm for eddy-current nondestructive evaluation," in *ACES*, 2009.

[139] J. García-Martín, J. Gómez-Gil, and E. Vázquez-Sánchez, "Non-destructive techniques based on eddy current testing," *Sensors*, vol. 11, pp. 2525-2565, 2011.

[140] G. Shu, A. Dehghan, and M. Shah, "Improving an Object Detector and Extracting Regions Using Superpixels," in *2013 IEEE Conference on Computer Vision and Pattern Recognition*, 2013, pp. 3721-3727.

[141] F. Liu, S. Chunhua, and L. Guosheng, "Deep convolutional neural fields for depth estimation from a single image," in *2015 IEEE Conference on Computer Vision and Pattern Recognition (CVPR)*, 2015, pp. 5162-5170.

[142] A. Lucchi, K. Smith, R. Achanta, G. Knott, and P. Fua, "Supervoxel-Based Segmentation of Mitochondria in EM Image Stacks With Learned Shape Features," *IEEE Transactions on Medical Imaging*, vol. 31, pp. 474-486, 2012.

[143] Y. Atoum, M. J. Afridi, X. Liu, J. M. McGrath, and L. E. Hanson, "On developing and enhancing plant-level disease rating systems in real fields," *Pattern Recognition*, vol. 53, pp. 287-299, 5// 2016.